TUM School of Engineering and Design

Grid and Particle Based Numerical Methods for Fluid and Solid Dynamics

Yujie Zhu

Vollständiger Abdruck der von der TUM School of Engineering and Design der Technischen Universität München zur Erlangung eines

Doktors der Ingenieur Wissenschaften

genehmigten Dissertation.

Vorsitzender: Prof. Dr.-Ing. Thomas Sattelmayer
Prüfer der Dissertation: 1. Priv.-Doz. Dr.-Ing. habil. Xiangyu Hu
2. Prof. Dr.-Ing. Oskar J. Haidn

Declaration of Authorship

I hereby declare that except where specific reference is made to the work of others, the contents of this dissertation are original and have not been submitted in whole or in part for consideration for any other degree or qualification in this, or any other university. This dissertation is my own work and contains nothing which is the outcome of work done in collaboration with others, except as specified in the text and Acknowledgements.

<div style="text-align: right">

Yujie Zhu
April 4, 2022

</div>

Abstract

In this cumulative thesis, several new numerical methods in both Eulerian and La-grangian perspective, including a high-order shock-capturing L2-norm regularized incremental-stencil Weighted Essentially Non-Oscillatory (WENO) scheme, a free-stream preserving method for linear-upwind and WENO schemes on curvilinear grids and an efficient Computer-Aided Design (CAD) compatible body-fitted parti-cle generator for particle-based methods, are developed and validated.

The first part of this thesis contributes to developing an L2-norm regularized incremental-stencil WENO scheme for compressible flows. Although WENO schemes adopting stencils with incremental sizes exhibit many advantages compared to the ones with uniform sizes in terms of robustness and performance, they still suf-fer from order degeneration near critical points and are too dissipative to resolve fine structures in turbulence or aeroacoustic flows. To address these drawbacks, the following three modifications are performed. (i) The 5th-order reconstruction is achieved by two 2-point and two 3-point stencils. An L2-norm error term, which is approximated from the discrepancy of numerical accuracy between 2-point stencils and classical 3-point stencils, is introduced into the weighting strategy to modulate the weights of these incremental stencils. (ii) A high-order non-dimensional discon-tinuity detector is chosen as the regularization parameter to control the contribution of the added error terms adaptively. (iii) With the above discontinuity detector, a hy-brid method is applied to further improve the performance of the scheme at smooth region and optimize the computational efficiency. A number of benchmark cases with strong discontinuities and fine flow structures demonstrate that the present method achieves very good fine-structure resolving capability and keeps the supe-rior numerical stability.

The second part of this thesis is devoted to propose a free-stream preserving method for general linear-upwind and WENO schemes on curvilinear grids. Gen-erally, it is problematic to apply high-order finite-difference scheme to curvilinear grids due to the dissatisfaction of the Geometric Conservation Law (GCL) and even the free-stream cannot be preserved. The geometrically induced errors from Jaco-bian and metrics evaluation can pollute the flow field and degrade the accuracy and consistency of the simulation. To eliminate these kind of errors and improve the con-sistency of the scheme, a free-stream preserving method is proposed. This method follows the Lax-Friedrichs splitting and rewrites the numerical flux into a central term and a numerical dissipation term. The numerical dissipation term is further reorganized into the form of local difference using neighboring grid-point pairs. For the central term, free-stream preserving can be achieved by adopting the Symmetri-cal Conservative Metric Method (SCMM). For the numerical dissipation term, each local difference is modified to share a common Jacobian and metric value which is evaluated by high-order schemes. Moreover, a simple free-stream preserving hy-bridization switching between linear-upwind and WENO schemes is proposed to further improve computational efficiency and reduce numerical dissipation. Several numerical cases on curvilinear grids regarding free-stream, isentropic vortex convec-tion, double Mach reflection, flow past a cylinder and supersonic wind tunnel with

a step reveal that the present method not only achieves good free-stream and vortex preserving properties but also recovers the shock-capturing ability of the original WENO scheme.

The third part of this thesis aims to provide an efficient CAD-compatible Body-fitted Particle Generator (CAD-BPG) for particle-based methods. Generating a high-quality body-fitted particle distribution for arbitrarily complex 3D geometry is highly challenging and hinders the potential of particle-based methods to engineering and bio-engineering applications. The proposed CAD-BPG provides a solution to this problem. CAD-BPG represents an arbitrarily complex geometry by parsing a CAD model, and describes the corresponding geometry surface by constructing an implicit zero level-set function on a Cartesian background mesh. To achieve a body-fitted and isotropic particle distribution, a physics-driven relaxation process with surface bounding governed by the transport-velocity formulation of Smoothed Particle Hydrodynamics (SPH) methodology is conducted to characterize the particle evolution. A set of examples with complex geometry, ranging from propeller, stent structures and anatomical heart models, demonstrate that the particle distribution generated by CAD-BPG describes the geometry precisely and particles are uniformly distributed. The improvements of computational accuracy by adopting the present CAD-BPG are then validated by a physical implementation in the modeling of wave-structure interaction. In addition, the present approach is CAD-compatible and can read arbitrarily complex geometry from external CAD files implying a promising potential of particle-based methods in real-world applications.

Acknowledgements

First and foremost, I would like to express my deep and sincere gratitude to my supervisor, PD Dr. Xiangyu Hu, for his guidance and warm encouragement during my Ph.D study. His extensive experience in numerical methods and in-depth understanding of fluid and solid dynamics benefit me a lot in this work. Xiangyu is always available whenever I have questions and I am very grateful to the meaningful discussions, which inspire me with new ideas, advise the work thoroughly and encourage me when I was frustrated. I also would like to thank Prof. Oskar J. Haidn for joining the examining committee and thank Prof. Thomas Sattelmayer for agreeing to be the chair of my thesis defense.

Great acknowledgment also goes to Prof. Wei Zhang and Zhensheng Sun, my master supervisors, for their consideration. During my Ph.D study, Prof. Zhang and Sun followed up my research and life and gave me a lot of encouragement. I also acknowledge the scholarship from Xidian University for providing the financial support of my research.

It is always a pleasure to work with my colleagues in the Chair of Aerodynamics and Fluid Mechanics (AER). Thanks for the fruitful discussions about solid dynamics and SPH methodology with Dr. Chi Zhang. I appreciate the collaboration and the help. I want to say thanks to Shucheng Pan, Jianhang Wang, Xiuxiu Lyv, Zhe Ji, Massoud Rezavand, Yuxuan Zhang, Wenbin Zhang, Dong Wu, Haitao Li, Shuoguo Zhang, Bo Zhang, Yijie Sun and many other colleagues for their accompany and courage. Particularly, I would like to thank Hua Liu and Angela Grygier, our secretaries, for their help and services. I also acknowledge other members in our chair, Ludger Pähler, Zhaoguang Wang, Yue Li and many others, for interesting discussions and accompany during my Ph.D study.

My gratitude also goes to many other friends in Munich. I would like to thank Xiaolong Wang, Hao Ma, Yongchuan Yu, Xiaojing Tang and Zhentong Wang for their daily help, supporting and accompany in Germany.

In the end, I am thoroughly grateful to my family. Thanks to my parents who have always helped me out of difficulties and supported me in every aspect of my life and research. Thanks to my wife who gives me love and understanding and encourages me all the time. Without their unconditional love and long-term encouragement, this thesis would never have been completed.

Contents

List of Symbols

CFSD	Computational Fluid and Solid Dynamics
FDM	Finite Difference Method
FVM	Finite Volume Method
FEM	Finite Element Method
CFD	Computational Fluid Dynamics
CSM	Computational Solid Mechanics
ENO	Essentially Non-Oscillatory
WENO	Weighted Essentially Non-Oscillatory
SPH	Smoothed Particle Hydrodynamics
CAD	Computer-Aided Design
CAD − BPG	CAD-compatible Body-fitted Particle Generator
EoS	Equation of State
RF	Roe Flux
LF	Lax-Friedrichs Flux
LLF	Local Lax-Friedrichs Flux
ODEs	Ordinary Differential Equations
SSP	Strong Stability-Preserving
CFL	Courant-Friedrich-Lewy
GCL	Geometric Conservation Law
SCL	Surface Conservation Law
VCL	Volume Conservation Law
SCMM	Symmetrical Conservative Metric Method
LES	Large Eddy Simulation
ILES	Implicit Large Eddy Simulation
DNS	Direct Numerical Simulation
TENO	Target Essentially Non-Oscillatory
FSI	Fluid Structure Interactions
MPS	Moving Particle Semi-implicit
DEM	Discrete Element Method
WVT	Weighted Voronoi Tessellation
CVP	Centroidal Voronoi Particle
OWSC	Oscillating Wave Surge Converter
2*D*	Two Dimensional
3*D*	Three Dimensional

Chapter 1

Introduction

1.1 Computational fluid and solid dynamics

Computational Fluid and Solid Dynamics (CFSD) provides an important numerical tool to investigate complex practical problems in engineering and science by numerical simulation with the assistance of computers. Compared to carrying experiments or using theoretical analysis, numerical simulation exhibits several important advantages in terms of economy, efficiency and flexibility, and becomes more and more attractive with the development of computer power. Moreover, it provides more insightful and fruitful information for a problem and plays an increasingly important role in validating theories, offering insights to experimental results and helping to discover new phenomena [1, 2, 3]. Figure 1.1 gives the necessary procedures to obtain solutions by numerical simulation. For a physical phenomenon related to fluid or solid dynamics, mathematical models, which are generally expressed in the form of governing equations, are first established by suitable assumptions. To solve the established governing equations numerically, the problem domain is divided into a number of components by a set of grids or particles. With the corresponding grid- or particle-based numerical schemes, a discrete mathematical description of the physical problem can be obtained. As the numerical scheme is essential to better understand the physics of a problem [4, 5], this thesis will focus on the performance of grid- and particle-based numerical methods and aim to improve their consistency and stability.
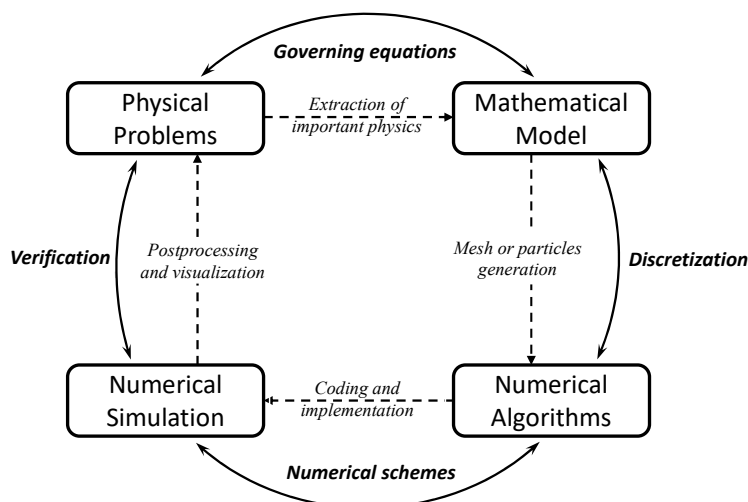

FIGURE 1.1: Sketch of the procedure for numerical simulation.

1.2   Brief review of numerical methods

1.2.1   Grid-based methods

According to the discretization approach, numerical methods can be generally classified into two groups, i.e. grid-based methods and particle-based methods. Typical grid-based methods include Finite Difference Method (FDM), Finite Volume Method (FVM) and Finite Element Method (FEM) and have been extensively applied in Computational Fluid Dynamics (CFD) and Computational Solid Mechanics (CSM).

For the simulation of complex flow with a vast range of spatial and temporal scales involved, high-order and high-resolution numerical methods are more favorable [6, 7]. As shown in Figure 1.2, high-order methods are more efficient compared to low-order ones to achieve the same accuracy for finer flow structures resolving. Considering the compressible flow in which both turbulence and shocks present, the simulation becomes much more challenging due to the requirement that the numerical schemes need to be of low dissipation in smooth region without damping the fine flow structures and be able to introduce adequate numerical dissipation for shock capturing. The low-order methods, e.g. the Godunov scheme [8], can capture the discontinuities monotonically, but may fail to resolve vortical structures and acoustic waves due to the excessive numerical dissipation. To achieve less numerical dissipation, various of high-order schemes based on structured grids [9, 10, 11, 12] and unstructured grids [13, 14, 15] have been developed. Among them, the Weighted Essentially Non-Oscillatory (WENO) scheme, an extension of the Essentially Non-Oscillatory (ENO) procedure aiming to achieve arbitrarily high-order accuracy in smooth region and resolve shocks shapely, gains much attention and has been widely used in applications [16]. Besides, it is well known that the FDM, which is based on structured grids, is easier to be extended to high-order versions and requires much less computational effort [17], and thus is more promising to solve the problems with simple geometry domain. However, directly applying these high-order schemes to curvilinear grids for problems with complex geometry is problematic [18, 19] and classic WENO scheme faces several shortcomings, like excessive numerical dissipation for sustaining fine structures and lack of numerical stability for strong discontinuities [20, 21]. Thus, further researches for high-order methods in terms of consistency and stability are necessary and essentially important for high performance computing.

1.2.2   Particle-based methods

As an alternative, particle-based numerical methods have been extensively studied and received increasing interest during the past decades. The key idea of particle-based method is to use a set of arbitrarily distributed particles other than a predefined mesh or grid to descretize the system and provide accurate and stable numerical solutions for established governing equations. The distinct meshfree feature makes particle-based methods more attractive in dealing with problems corresponding to free surfaces, large deformations, moving interfaces, etc, which are difficult for the aforementioned grid-based methods. Several interesting applications are given in Figure 1.3.

In recent years, various of particle-based methods [26, 27, 28, 29] have been developed for fluid and solid dynamics. One notable method is Smoothed Particle Hydrodynamics (SPH), which was first proposed for astrophysical applications [26, 27].
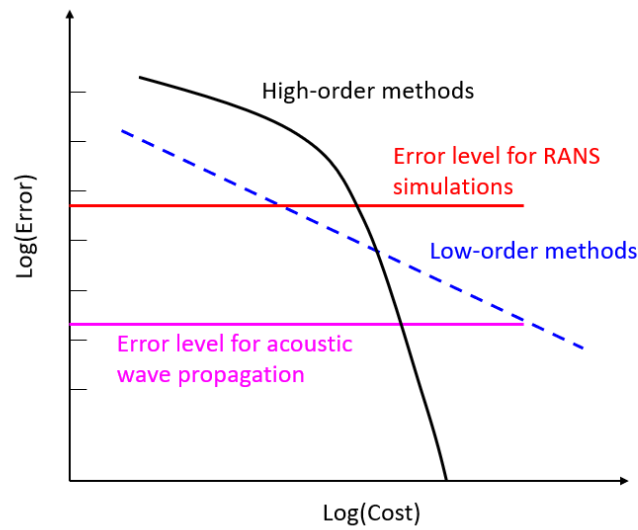
FIGURE 1.2: Comparison of cost and error between low- and high-order methods (reproduced from Ref. [7]).
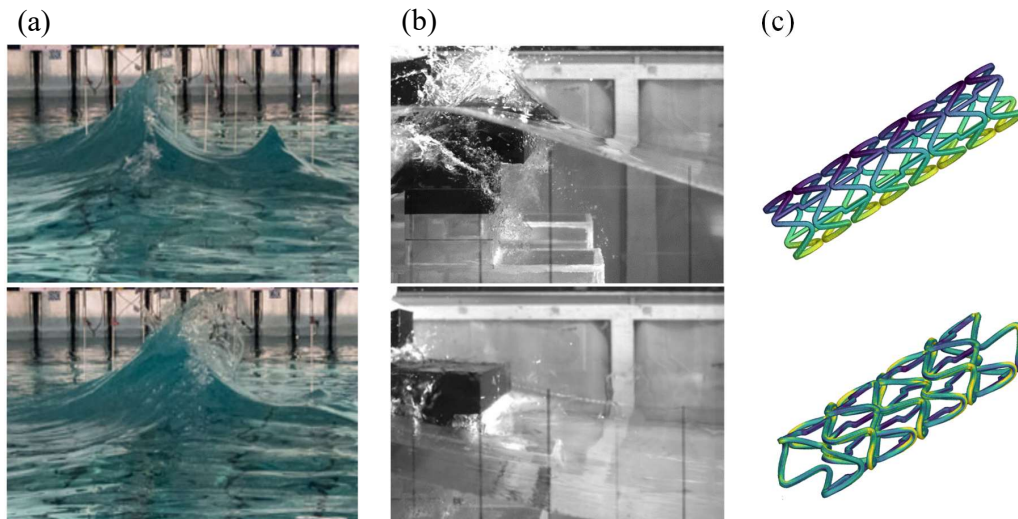
FIGURE 1.3: Typical applications for particle-based methods : (a) Draupner wave breaking (reproduced from Ref. [22]), (b) freak wave impacts on a tension-leg platform (reproduced from Ref. [23]) and (c) the simulation of a realistic cardiovascular stent structure (reproduced from Refs. [24, 25]).

In SPH method, a set of particles carrying material properties and moving with their local velocity are adopted to represent the state of a system. Field functions are expressed in integral form by kernel approximation using a smoothing kernel function with a specified compact support as shown in Figure 1.4. Particle approximation is then performed to further approximate the integral functions using particles. More detailed theory and fundamentals of SPH can be found in comprehensive reviews [30, 31, 32, 33]. As particle approximation is carried out at every time step, the computation only depends on current local particle distributions. This local adaptive feature as well as the well-established theory make SPH attractive especially for the problems involving large deformations. SPH method has been successfully applied to various areas, e.g. fluid dynamics [34, 35, 36, 37], solid dynamics [38, 39, 40, 41],

Fluid Structure Interactions (FSI) [42, 43] and multi-physics applications for cardiac function [44].

As mentioned in Ref. [3], particle representation is one of the major steps in SPH simulation, which is closely related to the initial creation of particles. However, generating a high-quality particle distribution is never an easy task especially for industrial and biomechanical applications, where the geometry is relatively complex in usual. As a high-quality particle distribution is essential for the simulation accuracy, it is significant to develop an efficient particle generator to create body-fitted and homogeneous distributions for particle-based methods, which is one of the major concerns of the present thesis.

kernel function

$$W = (|\boldsymbol{x} - \xi|, h)$$

r_e

target particle x

$\Omega_i =$ influence domain of particle i

neighboring particle ξ
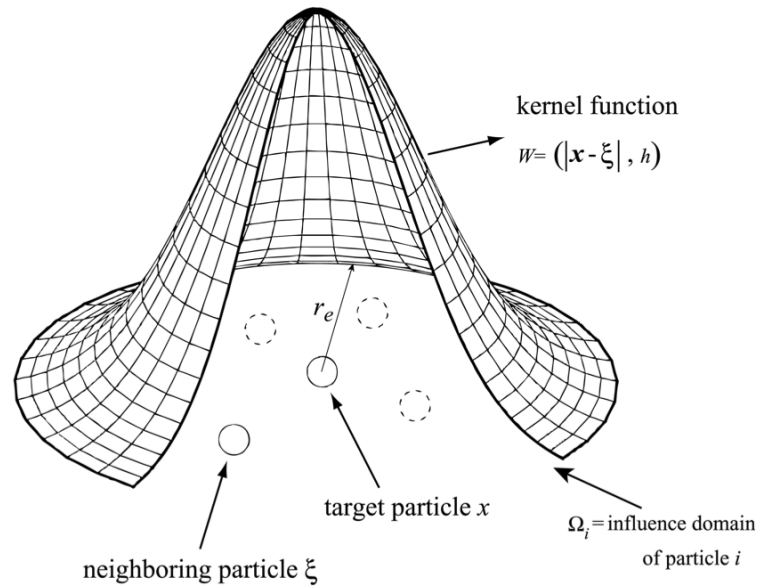
FIGURE 1.4: Smoothing kernel function with compact support.

1.3 Aims and objectives

In the present thesis, several novel numerical methods are proposed to address the aforementioned issues relevant to grid- and particle-based methods in modeling fluid and solid dynamics.

Considering the simulation of compressible flows where present a broadband of length scales and discontinuities, an L2-norm regularized incremental-stencil WENO scheme is proposed. The key idea is to modify the WENO weighting strategy by taking account the L2-norm error term. The relative contribution of the error term and the regularization term is controlled by a non-dimensional discontinuity detector. After adopting a simple hybridization with the optimal linear scheme, the proposed method achieves very good wave resolving capability and keeps the superior numerical stability. This work is detailed in Paper I [45]

- Y. J. Zhu, X. Y. Hu, An L2-norm regularized incremental-stencil WENO scheme for compressible flows. *Computers & Fluids*. 213 (2020): 104721

which has been attached in Appendix A.1.

Although high-order finite-difference schemes, e.g. the method proposed in Paper I [45], have advantages in terms of wave-resolution capability and numerical efficiency, they encounter the free-stream preserving problem, i.e. the dissatisfaction

of 0th-order consistency, on curvilinear grids. Therefore, the next objective of this thesis is to propose a free-stream preserving method for general linear-upwind and WENO schemes by eliminating the geometrically induced error. After rewriting the numerical flux into a central term and a numerical dissipation term in a local difference form, a novel modification is introduced to the latter term. Extensive tests demonstrate that the proposed method achieves good free-stream and vortex preserving property and keeps the shock-capturing ability of the original method. This work is detailed in Paper II [46]

- Y. J. Zhu, X. Y. Hu, Free-stream preserving linear-upwind and WENO schemes on curvilinear grids. *J. Comput. Phys*. 399 (2019): 108907

which is attached in Appendix A.2.

Compared to grid-based method, particle-based methods exhibit several important advantages especially for modeling flexible structures with large deformations, and have been successfully applied to industrial problems. However, generating a high-quality particle distribution for complex geometry is challenging and hinders the potential of particle-based methods. Thus, the last but not least objective of the thesis is to provide an efficient CAD-compatible Body-fitted Particle Generator (CAD-BPG) for particle-based methods. An arbitrarily complex geometry is accessed by parsing the CAD model and the corresponding surface is described by an implicit zero level-set function. A physics-driven relaxation process with surface bounding is then conducted to characterize the particle evolution. The proposed CAD-BPG is efficient and can generate body-fitted and isotropic distribution for arbitrarily complex geometry, implying a promising potential of particle-based methods in real-world applications. This work is detailed in Paper III [24]

- Y. J. Zhu, C. Zhang, Y. C. Yu, X. Y. Hu, A CAD-compatible body-fitted particle generator for arbitrarily complex geometry and its application to wave-structure interaction. *J. Hydrodyn*. 33.2 (2021): 195-206

which is attached in Appendix A.3.

1.4 Outline

The thesis is organized as follows. In Chapter 2, the classical numerical methods for hyperbolic conservation laws and the particle generator, e.g. the WENO scheme on both Cartesian and curvilinear grids and the SPH method, are reviewed. In Chapter 3, state-of-the-arts of the proposed numerical methods are detailed. Particularly, a high-resolution and very robust WENO scheme based on L2-norm regularization is developed, a free-stream preserving method for general linear-upwind and WENO schemes is proposed and an efficient CAD-BPG is presented to generate high-quality particle distributions for particle-based methods. In Chapter 4, discussions of the proposed methods are given and outlooks are presented.

Chapter 2

Numerical methodology

In this chapter, the relevant grid-based numerical methods in both Cartesian and curvilinear coordinates for hyperbolic conservation laws are briefly reviewed. Then, particle generation related methods, e.g. smoothed particle hydrodynamics, are given.

2.1 Hyperbolic conservation laws

This section briefly reviews the theory and methodology of classic finite-difference WENO scheme and describes the discretization of governing equations, i.e., Navier-Stokes equation, with WENO scheme in Cartesian coordinates (t, x, y, z).

2.1.1 Governing equations

In Eulerian description, the Navier-Stokes equations for compressible flows can be written in the following conservative form as

$$\frac{\partial \mathbf{U}}{\partial t} + \frac{\partial (\mathbf{F} - \mathbf{F_v})}{\partial x} + \frac{\partial (\mathbf{G} - \mathbf{G_v})}{\partial y} + \frac{\partial (\mathbf{H} - \mathbf{H_v})}{\partial z} = 0, \tag{2.1}$$

where $\mathbf{U} = [\rho \quad \rho u \quad \rho v \quad \rho w \quad E]^T$ denotes the conservative variables, $\mathbf{F}$, $\mathbf{G}$, $\mathbf{H}$ are inviscid fluxes and

$$\begin{cases} \mathbf{F} = [\rho u \quad \rho u^2 + p \quad \rho v u \quad \rho w u \quad (E+p)u]^T \\ \mathbf{G} = [\rho v \quad \rho u v \quad \rho v^2 + p \quad \rho w v \quad (E+p)v]^T \\ \mathbf{H} = [\rho w \quad \rho u w \quad \rho v w \quad \rho w^2 + p \quad (E+p)w]^T \end{cases} . \tag{2.2}$$

Here, ρ and u, v, w denote the density and Cartesian velocity components in $x-, y-, z-$ direction, $E = \rho e + \frac{1}{2}\rho(u^2 + v^2 + w^2)$ is the total energy. $\mathbf{F}_v$, $\mathbf{G}_v$, $\mathbf{H}_v$ represent the diffusive fluxes and

$$\begin{cases} \mathbf{F}_v = [0 \quad \tau_{xx} \quad \tau_{yx} \quad \tau_{zx} \quad \beta_x]^T \\ \mathbf{G}_v = [0 \quad \tau_{xy} \quad \tau_{yy} \quad \tau_{zy} \quad \beta_y]^T \\ \mathbf{H}_v = [0 \quad \tau_{xz} \quad \tau_{yz} \quad \tau_{zz} \quad \beta_z]^T \end{cases} , \tag{2.3}$$

where

$$\begin{cases} \beta_x = u\tau_{xx} + v\tau_{yx} + w\tau_{zx} - q_x \\ \beta_y = u\tau_{xy} + v\tau_{yy} + w\tau_{zy} - q_y \\ \beta_z = u\tau_{xz} + v\tau_{yz} + w\tau_{zz} - q_z \end{cases} \tag{2.4}$$

with $\mathbf{q} = q_x \mathbf{i} + q_y \mathbf{j} + q_z \mathbf{k} = -\kappa \nabla T$ following Fourier's law. For Newtonian fluid, the viscous stress tensors are defined according to Stokes' hypothesis as

$$\begin{cases} \tau_{xx} = 2\mu \dfrac{\partial u}{\partial x} + \lambda(\dfrac{\partial u}{\partial x} + \dfrac{\partial v}{\partial y} + \dfrac{\partial w}{\partial z}) & \tau_{xy} = \tau_{yx} = \mu(\dfrac{\partial u}{\partial y} + \dfrac{\partial v}{\partial x}) \\[2mm] \tau_{yy} = 2\mu \dfrac{\partial v}{\partial y} + \lambda(\dfrac{\partial u}{\partial x} + \dfrac{\partial v}{\partial y} + \dfrac{\partial w}{\partial z}) & \tau_{yz} = \tau_{zy} = \mu(\dfrac{\partial v}{\partial z} + \dfrac{\partial w}{\partial y}) \;, \\[2mm] \tau_{zz} = 2\mu \dfrac{\partial w}{\partial z} + \lambda(\dfrac{\partial u}{\partial x} + \dfrac{\partial v}{\partial y} + \dfrac{\partial w}{\partial z}) & \tau_{zx} = \tau_{xz} = \mu(\dfrac{\partial u}{\partial z} + \dfrac{\partial w}{\partial x}) \end{cases} \tag{2.5}$$

where $\lambda = -2\mu/3$ and μ denotes the viscosity defined by Sutherland's law. If the viscous diffusion and heat conduction are not considered, the Navier-Stokes equations can be simplified to Euler equations, i.e.,

$$\frac{\partial \mathbf{U}}{\partial t} + \frac{\partial \mathbf{F}}{\partial x} + \frac{\partial \mathbf{G}}{\partial y} + \frac{\partial \mathbf{H}}{\partial z} = \mathbf{0}. \tag{2.6}$$

To close the system of Eq. (2.6), the ideal-gas Equation of State (EoS) $p = (\gamma - 1)\rho e$ with γ the specific heats ratio is adopted.

For simplicity, the Euler equations Eq. (2.6) are mainly considered in the present work. Within a uniform grid, the semi-discrete form of Eq. (2.6) at a grid point indexed as (i, j, k) gives

$$\left(\frac{\mathrm{d}\mathbf{U}}{\mathrm{d}t} \right)_{i,j,k} = -(\delta_x \mathbf{F}_{i,j,k} + \delta_y \mathbf{G}_{i,j,k} + \delta_z \mathbf{H}_{i,j,k}), \tag{2.7}$$

where δ_x, δ_y and δ_z are flux derivative operators in $x-$, $y-$ and $z-$ direction, respectively. A conservative formulation of the operators, say $\delta_x \mathbf{F}_{i,j,k}$, is

$$\delta_x \mathbf{F}_{i,j,k} = \frac{1}{\Delta x} \left(\hat{\mathbf{F}}_{i+1/2,j,k} - \hat{\mathbf{F}}_{i-1/2,j,k} \right), \tag{2.8}$$

where $\hat{\mathbf{F}}_{i\pm1/2,j,k}$ are the numerical fluxes at half point and Δx is the equidistant space step. In fact, the reconstruction of numerical fluxes at the cell interface is the key point for modern methods in terms of high-order accuracy and stability. The detailed procedure, say $\hat{\mathbf{F}}_{i+1/2}$, includes the following steps. In the following, the subscripts j and k are omitted for simplicity.

First, the conservative variables and fluxes are projected into characteristic space following

$$\mathbf{u}_m = \mathbb{L}_{i+1/2} \cdot \mathbf{U}_m, \quad \mathbf{f}_m = \mathbb{L}_{i+1/2} \cdot \mathbf{F}_m, \quad m = \{\cdots, i-1, i, i+1, \cdots\}, \tag{2.9}$$

where $\mathbb{L}_{i+1/2}$ denotes the left eigenvector matrix of the linearized Roe-average Jacobian matrix $\mathbb{A}_{i+1/2}$ [47].

Second, flux splitting is carried out to split the projected fluxes as

$$f_m^{s,\pm} = \frac{1}{2} \left(f_m^s \pm \alpha^s u_m^s \right), \tag{2.10}$$

where f_m^s and u_m^s denote the s-th element of vector $\mathbf{f}_m$ and $\mathbf{u}_m$, $f_m^{s,+}$ and $f_m^{s,-}$ are the positive and negative characteristic fluxes. Here, $\alpha^s = \left| \lambda_{i+1/2}^s \right|$, where λ^s denotes the s-th eigenvalue of $\mathbb{A}_{i+1/2}$, for Roe Flux (RF) splitting scheme. Otherwise, $\alpha^s = \left| \lambda_l^s \right|_{max}$ with l representing the entire computational domain for Lax-Friedrichs

(LF) splitting scheme and for Local Lax-Friedrichs (LLF) splitting scheme when l represents the local stencil.

Then, the characteristic fluxes are reconstructed at the cell interface $i + 1/2$ by modern methods and

$$\hat{f}^s_{i+1/2} = \hat{f}^{s,+}_{i+1/2} + \hat{f}^{s,-}_{i+1/2}. \tag{2.11}$$

Finally, the flux in physics space can be transformed from characteristic flux by

$$\hat{\mathbf{F}}_{i+1/2} = \mathbb{R}_{i+1/2} \cdot \hat{\mathbf{f}}_{i+1/2}, \tag{2.12}$$

where $\mathbb{R}_{i+1/2}$ is the right eigenvector matrix of $\mathbb{A}_{i+1/2}$.

2.1.2 WENO schemes

For simplicity, the following one-dimensional scalar hyperbolic conservation law is considered

$$\frac{\partial u}{\partial t} + \frac{\partial f(u)}{\partial x} = 0 \tag{2.13}$$

as a prototype. Here, the characteristic velocity is assumed to be positive with $\frac{\partial f(u)}{\partial u} > 0$.

On a uniform grid, denote $x_i = i\Delta x$ and quantities at the point x_i are identified by the subscript i. Using the method of lines, the semi-discrete form of Eq. (2.13) can be approximated by a conservative finite difference scheme as

$$\frac{\mathrm{d}u_i}{\mathrm{d}t} = -\frac{1}{\Delta x} \left(h_{i+1/2} - h_{i-1/2} \right), \tag{2.14}$$

where $h_{i\pm1/2} = h(x_{i\pm1/2})$ and is implicitly defined by

$$f(x) = \frac{1}{\Delta x} \int_{x-\Delta x/2}^{x+\Delta x/2} h(\xi)d\xi. \tag{2.15}$$

By introducing numerical fluxes $\hat{f}_{i\pm1/2}$, which are reconstructed by high-order polynomial interpolations, Eq. (2.14) can be further approximated as

$$\frac{\mathrm{d}u_i}{\mathrm{d}t} \approx -\frac{1}{\Delta x} \left(\hat{f}_{i+1/2} - \hat{f}_{i-1/2} \right). \tag{2.16}$$

For classic 5th-order WENO scheme [12], a 5-point stencil S_5, see Figure 2.1, is served as the full stencil to approximate the numerical flux $\hat{f}_{i+1/2}$. For the purpose of shock capturing, the full stencil is subdivided into three 3-point stencils, i.e., S_1, S_2 and S_3 as shown in Figure 2.1. The numerical flux $\hat{f}_{i+1/2}$ is assembled by a convex combination of these three candidate stencil fluxes as

$$\hat{f}_{i+1/2} = \sum_{k=1}^{3} \omega_k \hat{f}_{k,i+1/2}, \tag{2.17}$$

where $\hat{f}_{k,i+1/2}$ and ω_k are the reconstructed fluxes by candidate stencils and their

corresponding non-linear weights, respectively. The expressions of these three candidate fluxes are

$$
\begin{cases}
\hat{f}_{1,i+1/2} = -\dfrac{1}{6}f_{i-1} + \dfrac{5}{6}f_i + \dfrac{1}{3}f_{i+1} \\[2mm]
\hat{f}_{2,i+1/2} = \dfrac{1}{3}f_i + \dfrac{5}{6}f_{i+1} - \dfrac{1}{6}f_{i+2} \\[2mm]
\hat{f}_{3,i+1/2} = \dfrac{1}{3}f_{i-2} - \dfrac{7}{6}f_{i-1} + \dfrac{11}{6}f_i
\end{cases}
\tag{2.18}
$$
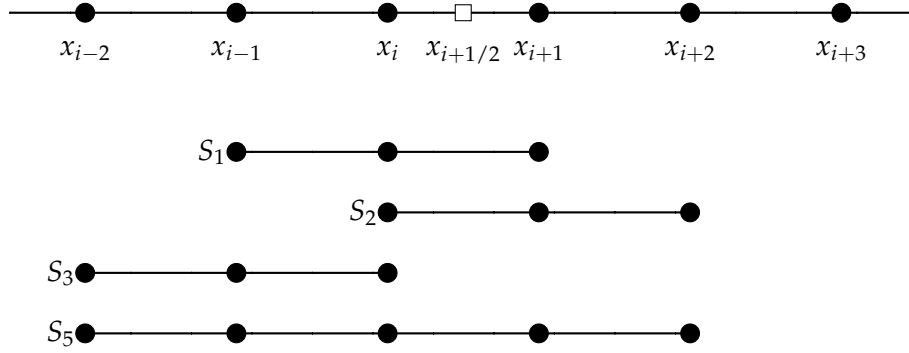
FIGURE 2.1: Sketch of the full stencil and candidate stencils for WENO reconstruction.

To avoid Gibbs oscillations [48] in vicinity of discontinuities, the weights are defined adaptively according to the smoothness of the stencil as

$$
\omega_k = \frac{\alpha_k}{\sum_{s=1}^{3} \alpha_s}, \quad \alpha_k = \frac{d_k}{(\beta_k + \varepsilon)^2}, \quad k = \{1,2,3\},
\tag{2.19}
$$

where d_k are optimal weights and $d_1 = 0.6$, $d_2 = 0.3$, $d_3 = 0.1$ for 5th-order accuracy. ε is a small positive parameter to prevent the division by zero, which also acts as a cut-off for smoothness measurement [49]. β_k denotes the smoothness indicator for each candidate stencil and is defined by

$$
\beta_k = \sum_{l=1}^{r_k-1} \Delta x^{2l-1} \int_{x_{i-1/2}}^{x_{i+1/2}} \left(\frac{d^l}{dx^l} \hat{f}_k(x) \right)^2 dx
\tag{2.20}
$$

following Jiang and Shu [12]. For 5th-order WENO scheme, the explicit expressions of β_k are

$$
\begin{cases}
\beta_1 = \dfrac{13}{12}(f_{i-1} - 2f_i + f_{i+1})^2 + \dfrac{1}{4}(f_{i-1} - f_{i+1})^2 \\[2mm]
\beta_2 = \dfrac{13}{12}(f_i - 2f_{i+1} + f_{i+2})^2 + \dfrac{1}{4}(3f_i - 4f_{i+1} + f_{i+2})^2 \\[2mm]
\beta_3 = \dfrac{13}{12}(f_{i-2} - 2f_{i-1} + f_i)^2 + \dfrac{1}{4}(f_{i-2} - 4f_{i-1} + 3f_i)^2
\end{cases}
\tag{2.21}
$$

Expansion of Eq. (2.21) in Taylor series at x_i gives

$$
\begin{cases}
\beta_1 = f'^2_i \Delta x^2 + \left(\dfrac{13}{12} f''^2_i + \dfrac{1}{3} f'_i f'''_i \right) \Delta x^4 + O\left(\Delta x^6\right) \\[2mm]
\beta_2 = f'^2_i \Delta x^2 + \left(\dfrac{13}{12} f''^2_i - \dfrac{2}{3} f'_i f'''_i \right) \Delta x^4 + \left(-\dfrac{1}{2} f'_i f''''_i + \dfrac{13}{6} f''_i f'''_i \right) \Delta x^5 + O\left(\Delta x^6\right) \\[2mm]
\beta_3 = f'^2_i \Delta x^2 + \left(\dfrac{13}{12} f''^2_i - \dfrac{2}{3} f'_i f'''_i \right) \Delta x^4 - \left(-\dfrac{1}{2} f'_i f''''_i + \dfrac{13}{6} f''_i f'''_i \right) \Delta x^5 + O\left(\Delta x^6\right)
\end{cases}
$$

$$(2.22)$$

Henrick et al. [50] pointed out that the condition of $w_k - d_k = O\left(\Delta x^3\right)$ should be satisfied for 5-point WENO scheme restoring the formal 5th-order accuracy. Following this idea, Borges et al. [51] proposed a new weighting strategy as

$$
\alpha_k = d_k \left(1 + \frac{\tau_5}{\beta_k + \varepsilon} \right) \tag{2.23}
$$

to improve the classic WENO scheme. τ_5 is evaluated by the absolute difference between β_2 and β_3, i.e., $\tau_5 = |\beta_2 - \beta_3|$. From Eq. (2.22), it is straightforward that the truncation error of $\tau_5 = O\left(\Delta x^5\right)$ and

$$
\frac{\tau_5}{\beta_k + \varepsilon} = O\left(\Delta x^3\right), \quad k = \{1,2,3\}, \tag{2.24}
$$

when there are no critical points. The condition of $w_k - d_k = O\left(\Delta x^3\right)$ is thus satisfied [51, 49].

Although WENO schemes using stencils with uniform size have achieved good wave-resolution capability by various modifications [52, 53], they suffer from numerical stability problems when high density ratio or strong shock waves present. Wang et al. [54] developed a 5th-order incremental-stencil WENO scheme (WENO-IS), which adopts both 2- and 3-point stencils for reconstruction. The sketch of the adopted stencils is shown in Figure 2.2. The basic idea is to split the 3-point stencil

FIGURE 2.2: Sketch of the candidate stencils with incremental width for WENO-IS reconstruction.

S_{01} into two 2-point stencils and the reconstructed fluxes are

$$
\begin{cases}
\hat{f}_{0,i+1/2} = \dfrac{1}{2}f_i + \dfrac{1}{2}f_{i+1} \\
\hat{f}_{1,i+1/2} = -\dfrac{1}{2}f_{i-1} + \dfrac{3}{2}f_i
\end{cases}.
\tag{2.25}
$$

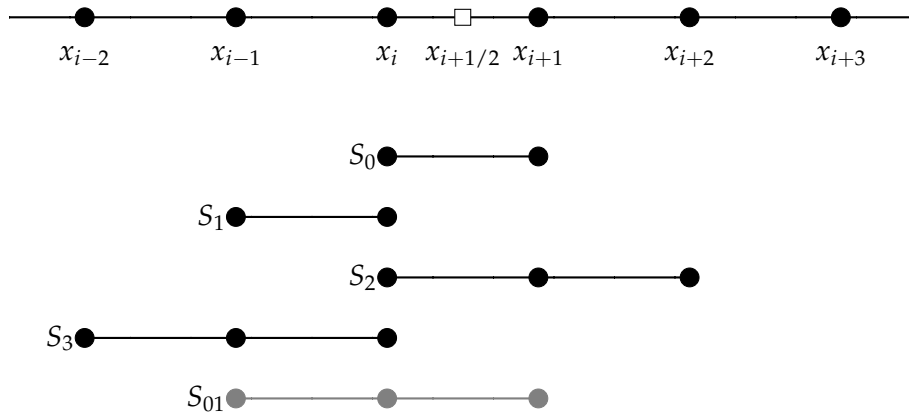Following Borges et al. [51], the nonlinear weights are evaluated by

$$
\omega_k = \frac{\alpha_k}{\sum_s \alpha_s}, \quad \alpha_k = d_k \left(1 + \frac{\tau_5}{\beta_k + \varepsilon}\right), \quad k = \{0,1,2,3\},
\tag{2.26}
$$

where $d_0 = 0.4$, $d_1 = 0.2$, $d_2 = 0.3$ and $d_3 = 0.1$ are the optimal weights. Following Eq. (2.20), the smoothness indicators β_0 and β_1 have the form of

$$
\begin{cases}
\beta_0 = (f_{i+1} - f_i)^2 \\
\beta_1 = (f_i - f_{i-1})^2
\end{cases}.
\tag{2.27}
$$

τ_5 is the global reference smoothness indicator and is defined by

$$
\tau_5 = \sum_{l=3}^{4} \Delta x^{2l-1} \int_{x_{i-1/2}}^{x_{i+1/2}} \left(\frac{d^l}{dx^l}\widehat{f}_k(x)\right)^2 dx,
\tag{2.28}
$$

where only the high-order components are contained. The explicit expression of τ_5 yields

$$
\tau_5 = \frac{13}{12}(f_{i+2} - 4f_{i+1} + 6f_i - 4f_{i-1} + f_{i-2})^2 + \frac{1}{4}(f_{i+2} - 2f_{i+1} + 2f_{i-1} - f_{i-2})^2.
\tag{2.29}
$$

By Taylor series expansion analysis,

$$
\tau_5 = O\left(\Delta x^6\right), \quad \frac{\tau_5}{\beta_k + \varepsilon} = O\left(\Delta x^4\right), \quad k = \{0,1,2,3\},
\tag{2.30}
$$

and thus the condition of $w_k - d_k = O\left(\Delta x^4\right)$ in smooth region is satisfied.

From Eq. (2.29), the smoothness indicators of 2-point stencils are evaluated from 1st-order derivatives, while these of 3-point stencils are from both 1st-order and 2nd-order derivatives of parabolic functions. This discrepancy may lead to order degeneration especially in the region near critical points. To avoid this problem, Wang et al. [54] made a slight modification to the weighting strategy as

$$
\alpha_0 = d_0 \left(1 + \frac{\tau_5}{\beta_0 + \varepsilon} \cdot \frac{\tau_5}{\beta_{01} + \varepsilon}\right), \quad \alpha_1 = d_1 \left(1 + \frac{\tau_5}{\beta_1 + \varepsilon} \cdot \frac{\tau_5}{\beta_{01} + \varepsilon}\right),
\tag{2.31}
$$

where

$$
\beta_{01} = \frac{13}{12}(f_{i-1} - 2f_i + f_{i+1})^2 + \frac{1}{4}(f_{i-1} - f_{i+1})^2
\tag{2.32}
$$

is the smoothness indicator of S_{01}.

2.1.3 Time integration

After approximating spatial derivatives, a set of Ordinary Differential Equations (ODEs) can be reformed from the Euler equations Eq. (2.6) as

$$\frac{d\mathbf{U}}{dt} = L(\mathbf{U}), \tag{2.33}$$

where $L(\mathbf{U})$ denotes the discretization of spatial operator. Generally, there are two kinds of ODE solver to advance the conservative variables in time, i.e., implicit and explicit methods. Although implicit method is more stable and allows larger time-step size, explicit one is more suitable for resolving transient flows and easier to construct high-order schemes. In Ref. [55], a class of Strong Stability-Preserving (SSP) high-order time discretization methods are developed. Among them, the explicit 3rd-order Runge-Kutta method is considered in this work, which includes the following three steps

$$\begin{cases} \mathbf{U}^{(1)} = \mathbf{U}^n + \Delta t L(\mathbf{U}^n) \\ \mathbf{U}^{(2)} = \frac{3}{4}\mathbf{U}^n + \frac{1}{4}\mathbf{U}^{(1)} + \frac{1}{4}\Delta t L(\mathbf{U}^{(1)}) \\ \mathbf{U}^{n+1} = \frac{1}{3}\mathbf{U}^n + \frac{2}{3}\mathbf{U}^{(2)} + \frac{2}{3}\Delta t L(\mathbf{U}^{(2)}) \end{cases} . \tag{2.34}$$

For numerical stability, the time-step size is constrained by a Courant-Friedrich-Lewy (CFL) condition.

2.2 Numerical methods on curvilinear grids

In this section, numerical formulations on curvilinear grids and the free-stream preserving problem are briefly introduced.

2.2.1 Governing equations on curvilinear grids

When curvilinear grids are adopted for numerical discretization, the Euler equations Eq. (2.6) should be transformed from Cartesian coordinates (t, x, y, z) to curvilinear coordinates (τ, ξ, η, ζ) according to the following relations

$$\tau = t, \quad \xi = \xi(x, y, z), \quad \eta = \eta(x, y, z), \quad \zeta(x, y, z). \tag{2.35}$$

The transformed equations in the conservation form yield

$$\tilde{\mathbf{U}}_\tau + \tilde{\mathbf{F}}_\xi + \tilde{\mathbf{G}}_\eta + \tilde{\mathbf{H}}_\zeta = 0, \tag{2.36}$$

where

$$\begin{cases} \tilde{\mathbf{U}} = \dfrac{\mathbf{U}}{J} \\ \tilde{\mathbf{F}} = \dfrac{\xi_x}{J}\mathbf{F} + \dfrac{\xi_y}{J}\mathbf{G} + \dfrac{\xi_z}{J}\mathbf{H} \\ \tilde{\mathbf{G}} = \dfrac{\eta_x}{J}\mathbf{F} + \dfrac{\eta_y}{J}\mathbf{G} + \dfrac{\eta_z}{J}\mathbf{H} \\ \tilde{\mathbf{H}} = \dfrac{\zeta_x}{J}\mathbf{F} + \dfrac{\zeta_y}{J}\mathbf{G} + \dfrac{\zeta_z}{J}\mathbf{H} \end{cases}, \tag{2.37}$$

and the subscript τ, ξ, η, ζ denote the temporal and spatial derivatives in curvilinear coordinates, respectively. The expressions of the transformation Jacobian J and metrics are

$$
\begin{cases}
\dfrac{1}{J} = x_\xi y_\eta z_\zeta - x_\eta y_\xi z_\zeta + x_\zeta y_\xi z_\eta - x_\xi y_\zeta z_\eta + x_\eta y_\zeta z_\xi - x_\zeta y_\eta z_\xi \\[2mm]
\dfrac{\xi_x}{J} = y_\eta z_\zeta - y_\zeta z_\eta, \quad \dfrac{\xi_y}{J} = x_\zeta z_\eta - x_\eta z_\zeta, \quad \dfrac{\xi_z}{J} = x_\eta y_\zeta - x_\zeta y_\eta \\[2mm]
\dfrac{\eta_x}{J} = y_\zeta z_\xi - y_\xi z_\zeta, \quad \dfrac{\eta_y}{J} = x_\xi z_\zeta - x_\zeta z_\xi, \quad \dfrac{\eta_z}{J} = x_\zeta y_\xi - x_\xi y_\zeta \\[2mm]
\dfrac{\zeta_x}{J} = y_\xi z_\eta - y_\eta z_\xi, \quad \dfrac{\zeta_y}{J} = x_\eta z_\xi - x_\xi z_\eta, \quad \dfrac{\zeta_z}{J} = x_\xi y_\eta - x_\eta y_\xi
\end{cases}
. \tag{2.38}
$$

2.2.2 Free-stream preserving problem

When a free-stream condition is imposed, where conservative variables and convective fluxes are constant, Eq. (2.36) can be rewritten as

$$
\tilde{\mathbf{U}}_\tau = - \left(I_x \mathbf{F} + I_y \mathbf{G} + I_z \mathbf{H} \right), \tag{2.39}
$$

where

$$
\begin{cases}
I_x = \left(\dfrac{\xi_x}{J} \right)_\xi + \left(\dfrac{\eta_x}{J} \right)_\eta + \left(\dfrac{\zeta_x}{J} \right)_\zeta = 0 \\[2mm]
I_y = \left(\dfrac{\xi_y}{J} \right)_\xi + \left(\dfrac{\eta_y}{J} \right)_\eta + \left(\dfrac{\zeta_y}{J} \right)_\zeta = 0 \\[2mm]
I_z = \left(\dfrac{\xi_z}{J} \right)_\xi + \left(\dfrac{\eta_z}{J} \right)_\eta + \left(\dfrac{\zeta_z}{J} \right)_\zeta = 0
\end{cases}
. \tag{2.40}
$$

Note that Eq. (2.40) may not be strictly satisfied when I_x, I_y and I_z are represented by numerical discretization. This inconsistency can introduce artificial disturbances in the simulation and lead to the so-called free-stream preserving problems.

Zhang et al. [56] introduced the concept of Surface Conservation Law (SCL), one component of GCL corresponding to stationary curvilinear grid. If a numerical scheme satisfies SCL, $I_x = I_y = I_z = 0$ as in Eq.(2.40) can still be satisfied with the numerical approximation of Jacobian, metrics and their derivative operators, and thus the free-stream can be preserved [57, 58].

To eliminate the geometrically induced error and improve the consistency of a scheme on curvilinear grids, Deng et al. [59] and Abe et al. [60] suggested to rewrite

the metric terms and Jacobian in Eq. (2.38) into a symmetrical conservative form as

$$
\begin{cases}
\dfrac{\xi_x}{J} = \dfrac{1}{2}\left[(y_\eta z)_\zeta - (y_\zeta z)_\eta + (yz_\zeta)_\eta - (yz_\eta)_\zeta\right] \\[2mm]
\dfrac{\xi_y}{J} = \dfrac{1}{2}\left[(xz_\eta)_\zeta - (xz_\zeta)_\eta + (x_\zeta z)_\eta - (x_\eta z)_\zeta\right] \\[2mm]
\dfrac{\xi_z}{J} = \dfrac{1}{2}\left[(x_\eta y)_\zeta - (x_\zeta y)_\eta + (xy_\zeta)_\eta - (xy_\eta)_\zeta\right] \\[2mm]
\dfrac{\eta_x}{J} = \dfrac{1}{2}\left[(y_\zeta z)_\xi - (y_\xi z)_\zeta + (yz_\xi)_\zeta - (yz_\zeta)_\xi\right] \\[2mm]
\dfrac{\eta_y}{J} = \dfrac{1}{2}\left[(xz_\zeta)_\xi - (xz_\xi)_\zeta + (x_\xi z)_\zeta - (x_\zeta z)_\xi\right]\,, \\[2mm]
\dfrac{\eta_z}{J} = \dfrac{1}{2}\left[(x_\zeta y)_\xi - (x_\xi y)_\zeta + (xy_\xi)_\zeta - (xy_\zeta)_\xi\right] \\[2mm]
\dfrac{\zeta_x}{J} = \dfrac{1}{2}\left[(y_\xi z)_\eta - (y_\eta z)_\xi + (yz_\eta)_\xi - (yz_\xi)_\eta\right] \\[2mm]
\dfrac{\zeta_y}{J} = \dfrac{1}{2}\left[(xz_\xi)_\eta - (xz_\eta)_\xi + (x_\eta z)_\xi - (x_\xi z)_\eta\right] \\[2mm]
\dfrac{\zeta_z}{J} = \dfrac{1}{2}\left[(x_\xi y)_\eta - (x_\eta y)_\xi + (xy_\eta)_\xi - (xy_\xi)_\eta\right]
\end{cases}
\tag{2.41}
$$

and

$$
\frac{1}{J} = \frac{1}{3}\left[\left(x\frac{\xi_x}{J}+y\frac{\xi_y}{J}+z\frac{\xi_z}{J}\right)_\xi + \left(x\frac{\eta_x}{J}+y\frac{\eta_y}{J}+z\frac{\eta_z}{J}\right)_\eta + \left(x\frac{\zeta_x}{J}+y\frac{\zeta_y}{J}+z\frac{\zeta_z}{J}\right)_\zeta\right].
\tag{2.42}
$$

With the above symmetrical metric terms, I_x can be evaluated by

$$
\begin{aligned}
I_x = \frac{1}{2}\Big[&\delta_1{}^\xi\delta_2{}^\zeta\left(z\delta_3{}^\eta y\right) - \delta_1{}^\xi\delta_2{}^\eta\left(z\delta_3{}^\zeta y\right) + \delta_1{}^\xi\delta_2{}^\eta\left(y\delta_3{}^\zeta z\right) - \delta_1{}^\xi\delta_2{}^\zeta\left(y\delta_3{}^\eta z\right) \\
&+\delta_1{}^\eta\delta_2{}^\xi\left(z\delta_3{}^\zeta y\right) - \delta_1{}^\eta\delta_2{}^\zeta\left(z\delta_3{}^\xi y\right) + \delta_1{}^\eta\delta_2{}^\zeta\left(y\delta_3{}^\xi z\right) - \delta_1{}^\eta\delta_2{}^\xi\left(y\delta_3{}^\zeta z\right) \\
&+\delta_1{}^\zeta\delta_2{}^\eta\left(z\delta_3{}^\xi y\right) - \delta_1{}^\zeta\delta_2{}^\xi\left(z\delta_3{}^\eta y\right) + \delta_1{}^\zeta\delta_2{}^\xi\left(y\delta_3{}^\eta z\right) - \delta_1{}^\zeta\delta_2{}^\eta\left(y\delta_3{}^\xi z\right)\Big],
\end{aligned}
\tag{2.43}
$$

where δ_1, δ_2 denote outer derivative operators and δ_3 is the inner derivative operator for calculating the corresponding level of the metric terms. By applying the Symmetrical Conservative Metric Method (SCMM) [59], in which the derivative operators of the above metrics are kept the same with that of the fluxes, it is easy to see that I_x equals to zero with $\delta_2{}^\xi = \delta_1{}^\xi$, $\delta_2{}^\eta = \delta_1{}^\eta$ and $\delta_2{}^\zeta = \delta_1{}^\zeta$. This technique is effective for linear central schemes and free-stream can be preserved accordingly. However, this method is difficult to be applied to upwind schemes, like the following presented linear-upwind and WENO schemes.

2.2.3 Free-stream preserving linear-upwind scheme

Without loss of generality, I use the explicit 5th-order linear-upwind scheme with local Lax-Friedrichs splitting to explain the difficulty of free-stream preserving and then propose an effective modification.

In curvilinear coordinates, the semi-discrete approximation of governing equations Eq. (2.36) at a grid point indexed as (i, j, k) is as follows

$$\left(\frac{d\tilde{\mathbf{U}}}{d\tau}\right)_{i,j,k} = -\left(\delta_1^{\tilde{\xi}}\tilde{\mathbf{F}}_{i,j,k} + \delta_1^{\eta}\tilde{\mathbf{G}}_{i,j,k} + \delta_1^{\zeta}\tilde{\mathbf{H}}_{i,j,k}\right), \tag{2.44}$$

where $\delta_1^{\tilde{\xi}}$, δ_1^{η} and δ_1^{ζ} are flux derivative operators in $\xi-$, $\eta-$ and $\zeta-$ direction, respectively. The derivative operator, e.g. $\delta_1^{\tilde{\xi}}\tilde{\mathbf{F}}_{i,j,k}$, has the following conservative form

$$\delta_1^{\tilde{\xi}}\tilde{\mathbf{F}}_{i,j,k} = \frac{1}{\delta\xi}\left(\tilde{\mathbf{F}}_{i+\frac{1}{2},j,k} - \tilde{\mathbf{F}}_{i-\frac{1}{2},j,k}\right), \tag{2.45}$$

where $\tilde{\mathbf{F}}_{i\pm\frac{1}{2},j,k}$ are the numerical fluxes at half points and $\delta\xi$ is the equidistant space step. Similar to the formulation on a uniform grid as given in Section 2.1.1, the numerical fluxes are reconstructed within a local characteristic field.

For 5th-order linear upwind scheme, the detailed procedure to obtain $\tilde{\mathbf{F}}_{i+\frac{1}{2}}$ is as follows. For simplicity, only the reconstruction in $\xi-$ direction is considered.

(1) Evaluate the Jacobian matrix $\mathbb{A}_{i+1/2} = \partial\tilde{\mathbf{F}}/\partial\tilde{\mathbf{U}}$ at a Roe-average state. Then, compute the corresponding left and right eigenvector matrices $\mathbb{L}_{i+1/2}$, $\mathbb{R}_{i+1/2}$ as well as the eigenvalues.

(2) Transform the fluxes and conservative variables at all grid-points within the stencil into characteristic space and carry out a local Lax-Friedrichs splitting as

$$f_m^{s,\pm} = \frac{1}{2}\mathbf{L}_{i+\frac{1}{2}}^s \cdot \left(\tilde{\mathbf{F}}_m \pm \lambda^s\tilde{\mathbf{U}}_m\right) \quad m = \{i-2, i+3\}, \tag{2.46}$$

where $f_m^{s,\pm}$ denote the s-th positive and negative characteristic fluxes, $\mathbf{L}_{i+\frac{1}{2}}^s$ is the s-th left eigenvector vector and $\lambda^s = \max\left(|\lambda_m^s|\right)$ denotes the largest s-th eigenvalue across the stencil.

(3) Construct the characteristic fluxes at the half point by the 5th-order linear-upwind scheme as

$$\begin{cases} f_{i+\frac{1}{2}}^{s,+} = \frac{1}{60}\left(2f_{i-2}^{s,+} - 13f_{i-1}^{s,+} + 47f_i^{s,+} + 27f_{i+1}^{s,+} - 3f_{i+2}^{s,+}\right) \\ f_{i+\frac{1}{2}}^{s,-} = \frac{1}{60}\left(-3f_{i-1}^{s,-} + 27f_i^{s,-} + 47f_{i+1}^{s,-} - 13f_{i+2}^{s,-} + 2f_{i+3}^{s,-}\right) \end{cases}. \tag{2.47}$$

(4) Transform the characteristic fluxes back into physical space by

$$\tilde{\mathbf{F}}_{i+\frac{1}{2}} = \sum_s \mathbf{R}_{i+\frac{1}{2}}^s \left(f_{i+\frac{1}{2}}^{s,+} + f_{i+\frac{1}{2}}^{s,-}\right), \tag{2.48}$$

where $\mathbf{R}_{i+\frac{1}{2}}^s$ is the s-th right eigenvector vector. Substituting Eqs. (2.46) and (2.47) into Eq. (2.48), the numerical flux can be expressed as

$$\tilde{\mathbf{F}}_{i+\frac{1}{2}} = \frac{1}{60}\left(\tilde{\mathbf{F}}_{i-2} - 8\tilde{\mathbf{F}}_{i-1} + 37\tilde{\mathbf{F}}_i + 37\tilde{\mathbf{F}}_{i+1} - 8\tilde{\mathbf{F}}_{i+2} + \tilde{\mathbf{F}}_{i+3}\right)$$
$$+ \frac{1}{60}\sum_s \mathbf{R}_{i+\frac{1}{2}}^s \lambda^s \mathbf{L}_{i+\frac{1}{2}}^s \cdot \left(\tilde{\mathbf{U}}_{i-2} - 5\tilde{\mathbf{U}}_{i-1} + 10\tilde{\mathbf{U}}_i - 10\tilde{\mathbf{U}}_{i+1} + 5\tilde{\mathbf{U}}_{i+2} - \tilde{\mathbf{U}}_{i+3}\right). \tag{2.49}$$

From Eq. (2.49), it is easy to see that the numerical flux corresponding to $\delta_1^{\tilde{\xi}}$ of Eq.

(2.45) contains not only the central flux term but also the numerical dissipation term which consists of conservative variables $\tilde{\mathbf{U}}$. The free-stream preserving of the central term can be achieved by SCMM with 6th-order central scheme applying to $\delta_2^{\tilde{\zeta}}$ as in Eq. (2.43). However, the numerical dissipation term with conservative variables $\tilde{\mathbf{U}}$ leads to the inconsistency of the overall $\delta_1^{\tilde{\zeta}}$ with $\delta_2^{\tilde{\zeta}}$ and the numerical dissipation term doesn't vanish when a free-stream is imposed.

In this work, the numerical dissipation term of Eq. (2.49) is rewritten into a local difference form as

$$
\tilde{\mathbf{F}}_{i+\frac{1}{2}}^{D} = \frac{1}{60} \sum_{s} \mathbf{R}_{i+\frac{1}{2}}^{s} \lambda^{s} \mathbf{L}_{i+\frac{1}{2}}^{s} \cdot \left[\left(\tilde{\mathbf{U}}_{i-2} - \tilde{\mathbf{U}}_{i-1} \right) - 4 \left(\tilde{\mathbf{U}}_{i-1} - \tilde{\mathbf{U}}_{i} \right) \right. \\
\left. + 6 \left(\tilde{\mathbf{U}}_{i} - \tilde{\mathbf{U}}_{i+1} \right) - 4 \left(\tilde{\mathbf{U}}_{i+1} - \tilde{\mathbf{U}}_{i+2} \right) + \left(\tilde{\mathbf{U}}_{i+2} - \tilde{\mathbf{U}}_{i+3} \right) \right] .
\tag{2.50}
$$

Then, each local difference is modified into a free-stream preserving formulation as

$$
\tilde{\mathbf{F}}_{i+\frac{1}{2}}^{D} = \frac{1}{60} \sum_{s} \mathbf{R}_{i+\frac{1}{2}}^{s} \lambda^{s} \mathbf{L}_{i+\frac{1}{2}}^{s} \cdot \left[\left(\mathbf{U}_{i-2} - \mathbf{U}_{i-1} \right) \left(\frac{1}{J} \right)_{i-\frac{3}{2}} - 4 \left(\mathbf{U}_{i-1} - \mathbf{U}_{i} \right) \left(\frac{1}{J} \right)_{i-\frac{1}{2}} \right. \\
\left. + 6 \left(\mathbf{U}_{i} - \mathbf{U}_{i+1} \right) \left(\frac{1}{J} \right)_{i+\frac{1}{2}} - 4 \left(\mathbf{U}_{i+1} - \mathbf{U}_{i+2} \right) \left(\frac{1}{J} \right)_{i+\frac{3}{2}} + \left(\mathbf{U}_{i+2} - \mathbf{U}_{i+3} \right) \left(\frac{1}{J} \right)_{i+\frac{5}{2}} \right],
\tag{2.51}
$$

by introducing local averaged grid Jacobian $\left(\frac{1}{J} \right)_{i-\frac{3}{2}}, \left(\frac{1}{J} \right)_{i-\frac{1}{2}}, \left(\frac{1}{J} \right)_{i+\frac{1}{2}}, \left(\frac{1}{J} \right)_{i+\frac{3}{2}}$ and $\left(\frac{1}{J} \right)_{i+\frac{5}{2}}$, which are evaluated by the 6th-order central scheme. Taking $\left(\frac{1}{J} \right)_{i+\frac{1}{2}}$ as an example,

$$
\left(\frac{1}{J} \right)_{i+\frac{1}{2}} = \frac{1}{60} \left[\left(\frac{1}{J} \right)_{i-2} - 8 \left(\frac{1}{J} \right)_{i-1} + 37 \left(\frac{1}{J} \right)_{i} + 37 \left(\frac{1}{J} \right)_{i+1} - 8 \left(\frac{1}{J} \right)_{i+2} + \left(\frac{1}{J} \right)_{i+3} \right].
\tag{2.52}
$$

It is easy to see that, when free-stream is imposed, the modification of Eq. (2.51) leads to the dissipation term vanishing. In addition, this modified method recovers the original linear-upwind scheme on Cartesian grids.

2.2.4 Free-stream preserving WENO scheme

For the classic 5th-order WENO scheme [12] with local Lax-Friedrichs flux splitting as given in Eq. (2.46), the positive reconstructed characteristic flux can be expressed as

$$
f_{i+\frac{1}{2}}^{s,+} = \sum_{k=0}^{2} \omega_{k}^{+} q_{k}^{+},
\tag{2.53}
$$

where

$$
\begin{cases}
q_{0}^{+} = \frac{1}{3} f_{i-2}^{s,+} - \frac{7}{6} f_{i-1}^{s,+} + \frac{11}{6} f_{i}^{s,+} \\
q_{1}^{+} = -\frac{1}{6} f_{i-1}^{s,+} + \frac{5}{6} f_{i}^{s,+} + \frac{1}{3} f_{i+1}^{s,+} , \\
q_{2}^{+} = \frac{1}{3} f_{i}^{s,+} + \frac{5}{6} f_{i+1}^{s,+} - \frac{1}{6} f_{i+2}^{s,+}
\end{cases}
\tag{2.54}
$$

are the fluxes obtained by three candidate stencils and ω_k^+ are the corresponding nonlinear weights (see Section 2.1.2 for the detailed formulation). The negative reconstructed flux can be evaluated in a similar way by flipping the stencils respect to $\xi_{i+1/2}$. Then, the numerical fluxes in physical space can be obtained by the transformation as Eq. (2.48). After reorganization [61, 62], the numerical flux can be rewritten into a central term and a dissipation term as

$$
\begin{aligned}
\tilde{\mathbf{F}}_{i+\frac{1}{2}} &= \tilde{\mathbf{F}}_{i+\frac{1}{2}}^+ + \tilde{\mathbf{F}}_{i+\frac{1}{2}}^- \\
&= \sum_s \mathbf{R}_{i+\frac{1}{2}}^s f_{i+\frac{1}{2}}^{s,+} + \sum_s \mathbf{R}_{i+\frac{1}{2}}^s f_{i+\frac{1}{2}}^{s,-} \\
&= \frac{1}{60}\left(\tilde{\mathbf{F}}_{i-2} - 8\tilde{\mathbf{F}}_{i-1} + 37\tilde{\mathbf{F}}_i + 37\tilde{\mathbf{F}}_{i+1} - 8\tilde{\mathbf{F}}_{i+2} + \tilde{\mathbf{F}}_{i+3}\right) \\
&\quad - \frac{1}{60}\sum_s \mathbf{R}_{i+\frac{1}{2}}^s \left\{\left(20\omega_0^+ - 1\right)\hat{f}_{i,1}^{s,+} - \left(10\left(\omega_0^+ + \omega_1^+\right) - 5\right)\hat{f}_{i,2}^{s,+} + \hat{f}_{i,3}^{s,+}\right\} \\
&\quad + \frac{1}{60}\sum_s \mathbf{R}_{i+\frac{1}{2}}^s \left\{\left(20\omega_0^- - 1\right)\hat{f}_{i,1}^{s,-} - \left(10\left(\omega_0^- + \omega_1^-\right) - 5\right)\hat{f}_{i,2}^{s,-} + \hat{f}_{i,3}^{s,-}\right\},
\end{aligned}
\tag{2.55}
$$

where

$$
\begin{cases}
\hat{f}_{i,r+1}^{s,+} = f_{i+r+1}^{s,+} - 3f_r^{s,+} + 3f_{i+r-1}^{s,+} - f_{i+r-2}^{s,+}, & r = \{0,1,2\} \\
\hat{f}_{i,r+1}^{s,-} = f_{i-r+3}^{s,-} - 3f_{i-r+2}^{s,-} + 3f_{i-r+1}^{s,-} - f_{i-r}^{s,-}, & r = \{0,1,2\}
\end{cases}.
\tag{2.56}
$$

Similar to the linear-upwind scheme, the central flux term in Eq. (2.55) can also achieve free-stream preserving by using 6th-order central scheme for δ_2^ξ. However, the extra numerical dissipation term leads to inconsistency between δ_2^ξ and δ_1^ξ. Another issue is that the approximation of Jacobian and metrics also introduces disturbances into the smoothness indicators of WENO scheme, so that the optimal background linear scheme is not recovered for a uniform flow either.

To address this issue, Eq. (2.56), e.g. $\hat{f}_{i,1}^{s,+}$, is rewritten into a local difference form as

$$
\begin{aligned}
\hat{f}_{i,1}^{s,+} &= f_{i+1}^{s,+} - 3f_i^{s,+} + 3f_{i-1}^{s,+} - f_{i-2}^{s,+} \\
&= \frac{1}{2}\mathbf{L}_{i+\frac{1}{2}}^s \cdot \left[\left(\tilde{\mathbf{F}}_{i+1} - \tilde{\mathbf{F}}_i\right) - 2\left(\tilde{\mathbf{F}}_i - \tilde{\mathbf{F}}_{i-1}\right) + \left(\tilde{\mathbf{F}}_{i-1} - \tilde{\mathbf{F}}_{i-2}\right)\right] \\
&\quad + \frac{1}{2}\lambda^s \mathbf{L}_{i+\frac{1}{2}}^s \cdot \left[\left(\tilde{\mathbf{U}}_{i+1} - \tilde{\mathbf{U}}_i\right) - 2\left(\tilde{\mathbf{U}}_i - \tilde{\mathbf{U}}_{i-1}\right) + \left(\tilde{\mathbf{U}}_{i-1} - \tilde{\mathbf{U}}_{i-2}\right)\right].
\end{aligned}
\tag{2.57}
$$

Then, the local difference form can be modified for free-stream preserving, similar to Eq. (2.51), as

$$
\begin{aligned}
\hat{f}_{i,1}^{s,+} &= \frac{\mathbf{L}_{i+\frac{1}{2}}^s}{2} \cdot \left[\left(\mathbf{F}_{i+1} - \mathbf{F}_i\right)\left(\frac{\xi_x}{J}\right)_{i+\frac{1}{2}} - 2\left(\mathbf{F}_i - \mathbf{F}_{i-1}\right)\left(\frac{\xi_x}{J}\right)_{i-\frac{1}{2}} + \left(\mathbf{F}_{i-1} - \mathbf{F}_{i-2}\right)\left(\frac{\xi_x}{J}\right)_{i-\frac{3}{2}}\right] \\
&\quad + \frac{\mathbf{L}_{i+\frac{1}{2}}^s}{2} \cdot \left[\left(\mathbf{G}_{i+1} - \mathbf{G}_i\right)\left(\frac{\xi_y}{J}\right)_{i+\frac{1}{2}} - 2\left(\mathbf{G}_i - \mathbf{G}_{i-1}\right)\left(\frac{\xi_y}{J}\right)_{i-\frac{1}{2}} + \left(\mathbf{G}_{i-1} - \mathbf{G}_{i-2}\right)\left(\frac{\xi_y}{J}\right)_{i-\frac{3}{2}}\right] \\
&\quad + \frac{\mathbf{L}_{i+\frac{1}{2}}^s}{2} \cdot \left[\left(\mathbf{H}_{i+1} - \mathbf{H}_i\right)\left(\frac{\xi_z}{J}\right)_{i+\frac{1}{2}} - 2\left(\mathbf{H}_i - \mathbf{H}_{i-1}\right)\left(\frac{\xi_z}{J}\right)_{i-\frac{1}{2}} + \left(\mathbf{H}_{i-1} - \mathbf{H}_{i-2}\right)\left(\frac{\xi_z}{J}\right)_{i-\frac{3}{2}}\right] \\
&\quad + \frac{\lambda^s}{2}\mathbf{L}_{i+\frac{1}{2}}^s \cdot \left[\left(\mathbf{U}_{i+1} - \mathbf{U}_i\right)\left(\frac{1}{J}\right)_{i+\frac{1}{2}} - 2\left(\mathbf{U}_i - \mathbf{U}_{i-1}\right)\left(\frac{1}{J}\right)_{i-\frac{1}{2}} + \left(\mathbf{U}_{i-1} - \mathbf{U}_{i-2}\right)\left(\frac{1}{J}\right)_{i-\frac{3}{2}}\right],
\end{aligned}
\tag{2.58}
$$

where the half-point metrics and Jacobians, say $\left(\frac{\xi_x}{J}\right)_{i+\frac{1}{2}}$, $\left(\frac{\xi_y}{J}\right)_{i+\frac{1}{2}}$, $\left(\frac{\xi_z}{J}\right)_{i+\frac{1}{2}}$ and $\left(\frac{1}{J}\right)_{i+\frac{1}{2}}$ are all evaluated with a 6th-order central scheme as in Eq. (2.52).

Furthermore, in order to achieve free-stream preserving for the smooth indicators, they are rewritten into a local difference formulation too, say β_0^+, as

$$\beta_0^+ = \frac{1}{4}\left[\left(f_{i-2}^{s,+} - f_{i-1}^{s,+}\right) - 3\left(f_{i-1}^{s,+} - f_i^{s,+}\right)\right]^2 + \frac{13}{12}\left[\left(f_{i-2}^{s,+} - f_{i-1}^{s,+}\right) - \left(f_{i-1}^{s,+} - f_i^{s,+}\right)\right]^2. \tag{2.59}$$

Then, the same treatment as Eq. (2.58) can be applied. Again, since the neighboring grid-point pairs share a common Jacobian and metric value, the smoothness indicators vanish for a uniform flow. Note that this free-stream preserving method also recovers the original WENO scheme on Cartesian grids.

2.3 Smoothed Particle Hydrodynamics

In this section, I briefly introduce the theories and fundamentals of SPH method and review the relevant numerical methods for fluid dynamics.

2.3.1 Governing equations

In Lagrangian description, the governing equations for inviscid flow include the conservation of mass and momentum as

$$\begin{cases} \dfrac{\mathrm{d}\rho}{\mathrm{d}t} = -\rho\nabla\cdot\mathbf{v} \\[2mm] \dfrac{\mathrm{d}\mathbf{v}}{\mathrm{d}t} = -\dfrac{1}{\rho}\nabla p \end{cases}, \tag{2.60}$$

where ρ, $\mathbf{v}$, p are the fluid density, velocity, pressure, respectively, and

$$\frac{\mathrm{d}(\bullet)}{\mathrm{d}t} = \frac{\partial(\bullet)}{\partial t} + \mathbf{v}\cdot\nabla(\bullet) \tag{2.61}$$

denotes the material derivative. To close the system of aforementioned equations, an artificial EoS is introduced. Under the weakly-compressible assumption, the fluid pressure is evaluated from density by

$$p = c_0^2\left(\rho - \rho_0\right), \tag{2.62}$$

where ρ_0 is the reference density and c_0 is the speed of sound defined by $c_0 = 10U_{max}$ with U_{max} the maximum anticipated flow speed.

2.3.2 Theory and fundamentals

Different from grid-based methods, SPH is a fully Lagrangian particle method, in which field variables are approximated by a set of particles. The formulations of SPH mainly include the following two steps, i.e., integral representation and particle approximation.

Any quantities or functions can be described in the form of integral representation by the following equation

$$f(\mathbf{r}) = \int_{\Omega} f(\mathbf{r}')\delta(\mathbf{r} - \mathbf{r}')d\mathbf{r}', \tag{2.63}$$

where $f(\mathbf{r})$ is a function with respect to the position vector $\mathbf{r}$, $\delta(\mathbf{r} - \mathbf{r}')$ is the Dirac delta function and Ω denotes the volume of the integral domain. As the Dirac delta function is applied, the integral representation in Eq.(2.63) is exact. To make it possible to establish a discrete model for the integral, a smoothing kernel function is introduced by Lucy [27] and Gingold and Monaghan [26] to replace the Delta function and Eq. (2.63) can be rewritten in kernel approximation form as

$$f(\mathbf{r}) = \int_{\Omega} f(\mathbf{r}')W(\mathbf{r} - \mathbf{r}', h)d\mathbf{r}', \tag{2.64}$$

where W is the smoothing kernel function and h denotes the smoothing length defining the effective width of W.

    If a set of particles are used to represent the system, the kernel approximation of $f(\mathbf{r})$ can be further discretized as

$$f(\mathbf{r}) = \sum_{j=1}^{N} f(\mathbf{r}_j)W(\mathbf{r} - \mathbf{r}_j, h)dV_j, \tag{2.65}$$

where N is the number of neighboring particles. The index j represents the particle label and dV_j denotes the finite volume of a particle. Since the particle has the mass of m and the density of ρ, the particle approximation can be rewritten as

$$f(\mathbf{r}) = \sum_{j=1}^{N} \frac{m_j}{\rho_j} f(\mathbf{r}_j)W(\mathbf{r} - \mathbf{r}_j, h), \tag{2.66}$$

by using $\frac{m_j}{\rho_j}$ to represent the volume. As shown in Figure 2.3, the summation is over all particles inside the support domain S, which is a circle (for 2D problem) centered at particle i with radius of kh.
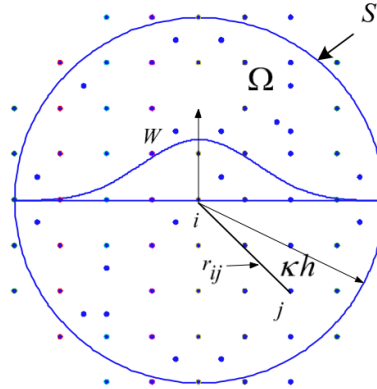

FIGURE 2.3: Sketch of particles approximation using particles inside the support domain.

    Following the same idea as in Eq. (2.64), the kernel approximation for the gradient of a function yields

$$\bigtriangledown f(\mathbf{r}) = \int_{\Omega} [\bigtriangledown f(\mathbf{r}')]W(\mathbf{r} - \mathbf{r}', h)d\mathbf{r}'. \tag{2.67}$$

According to partial integration and

$$[\bigtriangledown f(\mathbf{r}')]W(\mathbf{r} - \mathbf{r}', h) = \bigtriangledown [f(\mathbf{r}')W(\mathbf{r} - \mathbf{r}', h)] - f(\mathbf{r}')\bigtriangledown W(\mathbf{r} - \mathbf{r}', h), \tag{2.68}$$

the following equation can be obtained

$$
\begin{aligned}
\triangledown f(\mathbf{r}) &= \int_{\Omega} \triangledown [f(\mathbf{r}')W(\mathbf{r} - \mathbf{r}', h)]d\mathbf{r}' - \int_{\Omega} f(\mathbf{r}') \triangledown W(\mathbf{r} - \mathbf{r}', h)d\mathbf{r}' \\
&= \int_{S} f(\mathbf{r}')W(\mathbf{r} - \mathbf{r}', h)\mathbf{n}dS - \int_{\Omega} f(\mathbf{r}') \triangledown W(\mathbf{r} - \mathbf{r}', h)d\mathbf{r}',
\end{aligned}
\tag{2.69}
$$

where S denotes the surface of the integration domain Ω and $\mathbf{n}$ is the corresponding unit normal vector. If the support domain locates inside the problem, the surface integration term in right hand side of Eq. (2.69) equals to zero due to the compact support of kernel function. Thus, Eq. (2.69) can be simplified to

$$
\begin{aligned}
\triangledown f(\mathbf{r}) &= - \int_{\Omega} f(\mathbf{r}') \triangledown_{\mathbf{r}'} W(\mathbf{r} - \mathbf{r}', h)d\mathbf{r}' \\
&= \int_{\Omega} f(\mathbf{r}') \triangledown_{\mathbf{r}} W(\mathbf{r} - \mathbf{r}', h)d\mathbf{r}'.
\end{aligned}
\tag{2.70}
$$

Applying particle approximation as described in Eqs. (2.65-2.66), the discretized form of Eq. (2.70) yields

$$
\triangledown f(\mathbf{r}_i) = \sum_{j=1}^{N} \frac{m_j}{\rho_j} f(\mathbf{r}_j) \triangledown_i W(\mathbf{r}_i - \mathbf{r}_j, h),
\tag{2.71}
$$

where $\nabla_i W(\mathbf{r}_i - \mathbf{r}_j, h) = \mathbf{e}_{ij}\frac{\partial W_{ij}}{\partial r_{ij}}$ with $\mathbf{e}_{ij} = \frac{\mathbf{r}_i - \mathbf{r}_j}{|\mathbf{r}_i - \mathbf{r}_j|}$.

2.3.3 SPH discretization for governing equations

In SPH method, there are generally two approaches to calculate particle density. The first approach is to use the summation equation as given in Eq. (2.66) [32], and the density for a particle can be evaluated directly from

$$
\rho_i = \sum_{j=1}^{N} m_j W_{ij},
\tag{2.72}
$$

where $W_{ij} = W(\mathbf{r}_{ij}, h)$ is the smoothing kernel function. This approach is widely applied for multi-phase problems involving large density ratio [63]. Another approach is to solve the continuity equation, i.e. the mass conservation defined in Eq. (2.60). According to Divergence theorem, we have the following equation

$$
\nabla \cdot \mathbf{v} = \frac{1}{\Phi}[\nabla \cdot (\Phi \mathbf{v}) - \mathbf{v} \cdot \nabla \Phi].
\tag{2.73}
$$

By substituting Eq. (2.73) into the continuity equation and setting $\Phi = 1$, the SPH approximation of the continuity equation gives [64]

$$
\frac{d\rho_i}{dt} = \rho_i \sum_{j=1}^{N} \frac{m_j}{\rho_j}(\mathbf{v}_i - \mathbf{v}_j) \cdot \nabla_i W_{ij}.
\tag{2.74}
$$

Eq. (2.74) is also widely used and shows good performance for free-surface flows with violent events involved.

By applying the particle approximations for the gradient of a function (as given in Eq. (2.71)) to Eq. (2.60), the SPH formulation for the momentum conservation

equation can be obtained, which gives

$$\frac{d\mathbf{v}_i}{dt} = -\frac{1}{\rho_i} \sum_{j=1}^{N} m_j \frac{p_j}{\rho_j} \nabla_i W_{ij}.$$
(2.75)

Adding the following identity

$$\sum_{j=1}^{N} m_j \frac{p_i}{\rho_i \rho_j} \nabla_i W_{ij} = \frac{p_i}{\rho_i} \left(\sum_{j=1}^{N} \frac{m_j}{\rho_j} \nabla_i W_{ij} \right) = 0$$
(2.76)

to Eq. (2.75) leads to the final form as

$$\frac{d\mathbf{v}_i}{dt} = -\sum_{j=1}^{N} m_j \frac{p_i + p_j}{\rho_i \rho_j} \nabla_i W_{ij}.$$
(2.77)

Note that the right hand side of Eq. (2.77) denotes the repulsive force induced by the pressure. If a constant background pressure is adopted, the repulsive force leads to an equilibrium particle distribution by relaxation [65, 66, 67].

2.3.4 Time integration

For the time integration of governing equations, the position-based Verlet scheme can be applied following Ref. [43]. It includes the following steps. First, the fields of density and position are updated to the intermediate state as

$$\begin{cases} \rho_i^{n+\frac{1}{2}} = \rho_i^n + \frac{\Delta t}{2} \frac{d\rho_i}{dt} \\ \mathbf{r}_i^{n+\frac{1}{2}} = \mathbf{r}_i^n + \frac{\Delta t}{2} \mathbf{v}_i^n \end{cases}.$$
(2.78)

Then, the velocity at new time step is updated by

$$\mathbf{v}_i^{n+1} = \mathbf{v}_i^n + \Delta t \frac{d\mathbf{v}_i}{dt}.$$
(2.79)

Finally, the new time step positions and density can be updated from

$$\begin{cases} \mathbf{r}_i^{n+1} = \mathbf{r}_i^{n+\frac{1}{2}} + \frac{\Delta t}{2} \mathbf{v}_i^{n+1} \\ \rho_i^{n+1} = \rho_i^{n+\frac{1}{2}} + \frac{\Delta t}{2} \frac{d\rho_i}{dt} \end{cases}.$$
(2.80)

For numerical stability, the acoustic and body-force time-step criteria should be satisfied, i.e.

$$\Delta t \le 0.25 \left(\frac{h}{c + |\mathbf{v}|_{max}} \right),$$
(2.81)

and

$$\Delta t \le 0.25 \sqrt{\frac{h}{|d\mathbf{v}/dt|}}.$$
(2.82)

Chapter 3

Summaries of publications

In this chapter, the major achievements of this thesis and the relevant publications are briefly summarized.

3.1 An L2-norm regularized incremental-stencil WENO scheme for compressible flows

Y. J. Zhu and X. Y. Hu

3.1.1 State of the art

For the simulation of compressible flow involving a broadband of length scales and discontinuities, a stable numerical scheme with high-resolution property, which can introduce sufficient dissipation in vicinity of discontinuities to suppress numerical oscillations and keep high-order accuracy in smooth region at the same time, is essential. To achieve this goal, a range of numerical schemes have been proposed in the literature. Among them, WENO-JS scheme developed by Jiang and Shu [12] exhibits superior performance in terms of high-order accuracy and shock-capturing properties and has been extensively employed in Large Eddy Simulation (LES) and Direct Numerical Simulation (DNS). However, extensive numerical experiments and analyses reveal that the classic WENO-JS scheme may fail to recover the formal order of accuracy near critical points where the first or higher derivatives vanish [50].

To avoid order degeneration, several modifications have been proposed by improving the weighting strategy, e.g. the WENO-M scheme [50] with a corrective mapping applied to the classical WENO weights, the WENO-Z scheme [51, 49] with a new high-order smoothness indicator introduced, and the WENO-RL or WENO-RLTV scheme [68] switching on the optimal weights when the magnitudes of smoothness indicators are comparable. Although improved performances have been achieved by these variants, they are still too dissipative to sustain fine structures in turbulence or aeroacoustic flows. Another notable modification to WENO scheme is to introduce the contribution of the downwind stencil and use central scheme as the optimal linear scheme [20, 69, 52]. Hu et al. [52] proposed the WENO-CU6 scheme and introduced a new smoothness indicator for the adaptation between central and upwind stencils. Later, it was extended for Implicit Large Eddy Simulation (ILES) by incorporating a physically-motivated scale separation approach [53].

To enhance the numerical stability of very-high-order WENO schemes, Fu et al. [70] proposed a family of high-order TENO scheme by assembling a set of low-order candidate stencils with incrementally increasing stencil width. The consideration of low-order approximation polynomials in reconstruction makes TENO scheme considerably more robust. However, when high density ratio or strong shock waves

present, the positive preserving methods [71, 72] are still needed for TENO schemes to keep stable. Another numerical scheme with superior stability is the 5th-order WENO-IS scheme, which was proposed by Wang et al. [54]. In this scheme, both 2-point and 3-point stencils are adopted for reconstruction.

3.1.2   Summary of the publication

To address the drawbacks of classic WENO scheme, i.e. order degeneration near critical points, excessive numerical dissipation for resolving fine flow structures and the lack of numerical stability for strong discontinuities, Paper I proposed an L2-norm regularized incremental-stencil WENO scheme for compressible flows.

Different from the classic WENO scheme using stencils with uniform size, four stencils with incremental width are adopted as candidate stencils for high-order reconstruction following WENO-IS scheme. Since both 2-point and 3-point stencils are used, the scheme can degenerate gradually from high-order to low-order reconstruction according to the local smoothness. When strong discontinuities present in the flow, the reconstruction would prefer to choose the 2-point stencil, which makes the scheme, compared to the classic WENO-JS scheme, more robust.

L2-norm regularization is introduced into the WENO weighting strategy to modulate the weights of incremental stencils. The smoothness indicators of 2-point stencils are evaluated from the 1st-order derivative of a linear function, while these of the 3-point stencils are from both 1st-order and 2nd-order derivatives of a parabolic function. By taking account an L2-norm error term, the discrepancy of numerical accuracy between 2-point and 3-point stencils can be made up and excessive weights of 2-point stencils are reduced.

A suitable non-dimensional discontinuity detector is applied as the adaptive regularization parameter to control the contribution of the added error term and the regularization term. When the full 6-point stencil contains discontinuities, the regularization parameter becomes a large number, which makes the original smoothness indicator the leading term and the 2-point stencil will be assigned larger weights. Otherwise, the reconstruction prefers to choose 3-point stencils. Based on the discontinuity detector, a hybridization with a linear scheme is introduced to improve computational efficiency and further reduce numerical dissipation in very smooth region.

A number of cases including shock tube problems, shock/entropy wave interaction problems and a problem involving very strong discontinuities are considered to assess the performance of the proposed scheme. The numerical results of these cases reveal that the proposed method has good wave resolving capability and keeps the superior numerical stability.

3.1.3   Individual contributions of the candidate

This article [45] was published in the international peer-reviewed journal *computers and fluids*. My contribution to this work was the development of the method and the corresponding computer code for its implementation. I have performed simulations, analyzed the results, and wrote the manuscript for the publication.

3.2 Free-stream preserving linear-upwind and WENO schemes on curvilinear grids

Y. J. Zhu and X. Y. Hu

3.2.1 State of the art

High-order finite-difference schemes, like the proposed L2-norm regularized incremental stencil WENO scheme in Paper I [45], have shown good performance in numerical efficiency and good wave resolving property. However, it is problematic to directly apply them on stationary curvilinear grids due to the dissatisfaction of SCL [18, 19]. Since body-fitted curvilinear grids are widely used for problems with practical geometries, SCL is of great important. The grid Jacobian and metrics calculated in curvilinear coordinates can introduce large errors and lead numerical instability even when uniform flow is imposed, i.e., the free-stream preserving problem.

For low-order schemes, the simple averaging method [73], conservative form of metrics [18] or finite-volume-like technique [19] can help to achieve SCL. For high-order central compact scheme, Visbal and Gaitonde [74] verified that the geometrically induced error can be largely decreased by two steps, i.e., (i) utilizing the conservative form of metrics [18], (ii) discretizing the metric terms with the same compact scheme which is used for calculating the convective-flux derivatives. Then, Deng et al. [57] proposed a sufficient SCL condition for general high-order central schemes. However, further analyses [58, 59] showed that this condition is difficult to be satisfied by dissipative scheme, e.g. the widely used upwind schemes, due to the inconsistency outer-level differential operators used for flux splitting.

Since numerical dissipation is essential for a scheme to obtain stable solutions, upwind schemes have been extensively used in the simulation of compressible flows. To eliminate the geometrically induced error for upwind schemes, Nonomura et al. [62] split the upwind scheme into a non-dissipative central part and a dissipative part, and then implemented them, respectively, with high-order finite-difference and finite-volume-like schemes by freezing Jacobian and metric terms for the entire stencil. Other approaches modified the dissipative part by replacing the transformed conservative variables with the original ones [75, 76]. Zhu et al. [77] proposed a free-stream preserving technique for WENO scheme by introducing offsetting terms with the same WENO nonlinear weights for computing the corresponding inviscid fluxes. Although this technique is generally effective, it may lead to large errors due to the resulting of non-conservative formulation.

3.2.2 Summary of the publication

General high-order upwind schemes do not satisfy SCL and cannot preserve free-stream on curvilinear grids. To address this drawback, Paper II proposed a novel method to impose SCL for linear-upwind and WENO schemes and eliminate the geometrically induced error.

With a Lax-Friedrichs splitting, the numerical flux of a linear-upwind scheme or WENO scheme can be rewritten into a central term of the flux function and a numerical dissipation term. For the central flux term, free-stream preserving is achieved by the symmetric conservative metric method and the 6th-order linear central scheme (for the 5th-order scheme) is adopted for outer derivative operators of metrics.

For the dissipation term, the difference operator is split into several local differences involving only two successive grid points. Each neighboring grid-point pairs

are modified to share a common Jacobian and metric value which is evaluated by high-order schemes. Note that the dissipation term would vanish if a uniform flow is imposed. Furthermore, the smoothness indicators of WENO scheme are also modified for free-stream preserving with the same treatment.

In order to achieve less numerical dissipation and higher computational efficiency, a hybridization based on the above free-stream preserving linear-upwind and WENO scheme is introduced. Since both the candidate schemes are free-stream preserving and recover each other for a uniform flow, it is obvious that their hybridization has the same property.

This technique is simple and can be applied to general explicit linear-upwind scheme and other WENO schemes, e.g. WENO-CU6 scheme [52]. To validate the performance of the proposed method, a range of tests including free-stream, isentropic vortex convection, double Mach reflection and flow past cylinder are carried out on various non-uniform grids. Numerical results demonstrate that this method not only achieves good free-stream and vortex preserving properties, but also maintains the shock-capturing ability of original WENO schemes.

3.2.3 Individual contributions of the candidate

This article [46] was published in the international peer-reviewed journal *journal of computational physics*. My contribution to this work was the development of the method and the corresponding computer code for its implementation. I have performed simulations, analyzed the results, and wrote the manuscript for this publication.

3.3. A CAD-compatible body-fitted particle generator for arbitrarily complex geometry and its application to wave-structure interaction

27

3.3 A CAD-compatible body-fitted particle generator for arbitrarily complex geometry and its application to wave-structure interaction

Y. J. Zhu, C. Zhang, Y. C. Yu and X. Y. Hu

3.3.1 State of the art

Compared to grid-based numerical methods, e.g. the finite difference methods proposed in Paper I and Paper II, finite volume methods and finite element methods, the meshfree particle-based methods exhibit important advantages in modeling flexible structures with large deformations and complex flows when there present free surfaces, moving interfaces or fluid structure interactions [31]. These methods include Smoothed Particle Hydrodynamics (SPH) [26, 27], Moving-Particle Semi-implicit method (MPS) [28] and Discrete Element Method (DEM) [29] and attract increasing attention in a broad range of fields [31, 32].

In the past decades, particle-based methods have been applied in industrial applications where complex 3D geometries are involved, viz, bird strike [78], high pressure water jets impacting pelton turbine blades [79], oil flow inside a gearbox [80], wave-structure interactions [81, 82] and stent and myocardium deformation in biomechanics [83]. However, it is still a challenge to generate a high-quality body-fitted initial particle distribution for arbitrarily complex geometry and thus hinders the potential applications of particle-based methods.

Generally, there are two approaches to generate the initial particle distribution, i.e. (a) direct initiate particles on a lattice structure and (b) generate particles on a volume element mesh. The first approach is widely used in particle-based methods community [84] and the induced particle distribution is isotropic. However, a very fine spatial resolution is required to portray the correct surface in particular for complex geometry. The second approach generates particles at the center of tetra- or hexahedron volume elements and the particle volume equals to the corresponding element volume [85, 86]. Although the geometry surface can be accurately portrayed by this approach, the particle spacing and volume are non-uniform which would reduce the interpolation accuracy.

Recently, the Weighted Voronoi Tessellation (WVT) method was applied to generate initial particle distribution by Diehl et al. [87] for SPH astrophysical simulations. This method was later adopted by Siemann and Ritt [78] for SPH simulation of bird-strike. Vela et al. [88] also proposed an algorithm to construct complex initial density distributions for low noise property. More recently, Centroidal Voronoi Particle (CVP) method combining the Centroidal Voronoi Tessellation and Voronoi Particle concept was developed by Fu and Ji [89] to generate isotropic particle distribution. This method is effective and easy to be implemented for simple 2D geometry. However, it needs ghost particles to impose proper boundary conditions making it difficult to model complex 3D geometry as constructing their ghost particles is not an easy task.

3.3.2 Summary of the publication

To generate a body-fitted and homogeneous particle distribution for arbitrarily complex 3D geometry, Paper III proposed a CAD-compatible body-fitted particle generator.

First of all, the geometry information is accessed by importing and parsing the polygon mesh storing in external CAD files. The corresponding geometry surface is described by the zero level-set of the signed-distance function

$$\Gamma = \{(x, y, z) \, | \phi(x, y, z, t) = 0\} \tag{3.1}$$

based on a Cartesian background mesh.

Then, a preconditioned lattice particle distribution is generated inside the domain of a geometry. Particles are relaxed by a physics-driven relaxation process to obtain a homogeneous distribution with the transport-velocity formulation. To achieve the body-fitted feature, a simple surface bounding method is introduced. In this method, particles near the surface are enforced to locate on geometry surface and a body-fitted particle distribution is achieved accordingly as shown in Figure 3.1. With the assumption that each particle possesses an invariant volume, a
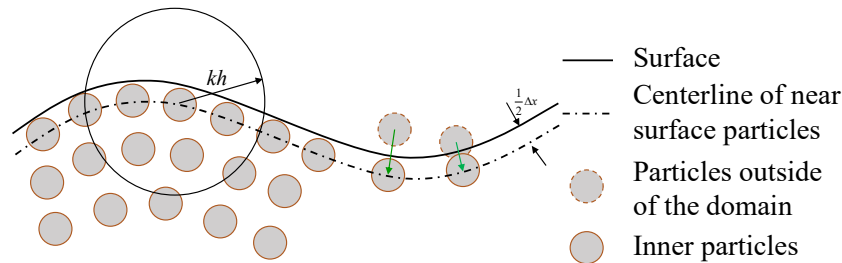
FIGURE 3.1: An illustration of surface particles bounding.

body-fitted well-regularized particle distribution can be achieved when system approaches to stable.

To test the performance of the proposed CAD-BPG, a number of structures with complex geometry, e.g. propeller, stents and anatomical heart models, are considered. Their final particle distributions represent the geometry well and particles are uniformly distributed implying the effectiveness of the proposed CAD-BPG for arbitrarily complex 3D geometry. The application for modeling wave-structure interaction, where regular wave interacts with an Oscillating Wave Surge Converter (OWSC), reveals that the present method not only provides an efficient and easy-to-implement pre-processing tool for particle-based simulation but also improves the numerical accuracy compared with the one with lattice particle distribution. In addition, the proposed approach is CAD-compatible and can read arbitrarily complex geometry from external CAD files.

3.3.3   Individual contributions of the candidate

This article [67] was published in the international peer-reviewed journal *journal of hydrodynamics*. My contribution to this work was the development of the method and the corresponding computer code for its implementation. I have performed simulations, analyzed the results, and wrote the manuscript for this publication.

Chapter 4

Discussion and Outlooks

4.1 Discussion

In this publication-based thesis, a series of novel numerical schemes have been proposed to improve the consistency and stability for grid- and particle-based methods. Targeted at WENO schemes on both Cartesian and curvilinear grids as well as particle generation related methods, this work has the following achievements. (i) A high-resolution L2-norm regularized incremental-stencil WENO scheme was proposed for compressible flows. (ii) A free-stream preserving method was proposed to improve the consistency of general linear-upwind and WENO schemes on curvilinear grids. (iii) An efficient CAD-BPG for 3D arbitrarily complex geometry was proposed for particle-based methods.

In the simulation of compressible flow, conventional WENO scheme [12] suffers from order degeneration and is too dissipative for sustaining fine structures in turbulence or aeroacoustic flows [50, 20]. In the literature, many modifications have been developed to address these drawbacks [51, 49], such as WENO-M and WENO-Z schemes [50, 51] by modifying the weighting strategy, WENO-CU6 scheme [52] by introducing the contribution of the downwind stencil and TENO scheme [70] by assembling a set of low-order candidate stencils with incrementally increasing stencil width. However, numerical tests reveal that the numerical stability of these variants is inferior to the classic WENO-JS scheme [12]. In contrast to aforementioned works, the present study adopts two 2-point and two 3-point stencils for 5th-order reconstruction. Since the smallest stencil is 2-point, the scheme is more robust compared to the classic WENO-JS scheme [12] and can simulate the flow field with strong discontinuities. Then, an L2-norm regularization strategy, which takes account the L2-error term to cope with the discrepancy of the smoothness indicators between 2-point and 3-point stencils, is introduced to modulate the weights of the incremental stencils. A non-dimensional discontinuity detector is then adopted as the regularization parameter to adaptively control the contribution of the error and regularization terms. In this way, 2-point stencils will be assigned larger weights when the full stencil contains discontinuities, otherwise, the reconstruction prefers to choose 3-point stencils. Furthermore, a hybridization with the optimal linear scheme is introduced to improve numerical efficiency and further reduce numerical dissipation for smooth regions. Extensive numerical tests involving a broadband of waves and discontinuities demonstrate that the proposed method is efficient and can resolve much finer flow structures. Moreover, the present method has superior numerical stability and can capture very strong discontinuities.

Another issue for conventional WENO scheme is that it cannot be directly applied to curvilinear grids due to the dissatisfaction of GCL [18, 19]. The computation in curvilinear coordinates is not 0th-order consistent and even free-stream cannot be

preserved. Solutions in literature mainly concentrated on central schemes. For instance, Visbal and Gaitonde [74] found a two-step procedure for central compact scheme to eliminate the geometrically induced error. Deng et al. [57] identified the outer- and inner-level differential operators for the metrics, and obtained a sufficient SCL condition for general high order central schemes [90]. However, as pointed out in Refs. [58, 59], this condition is difficult to be satisfied for upwind schemes, e.g. the high-order linear-upwind scheme and the conventional WENO scheme. The present work provides a novel solution of free-stream preserving for general high-order upwind schemes on curvilinear grids. The numerical flux of upwind schemes is rewritten into a linear central term of the flux functions and a numerical dissipation term, which is further reorganized into a local difference form of conservative variables for neighboring grid-point pairs. Since the SCMM method [59] is effective for linear central schemes, this method is introduced to the central term for free-stream preserving by adopting the same outer-level derivative operators with the flux to metrics. The local differences of the numerical dissipation term are modified to share the same Jacobian and metric terms, which are evaluated by high order schemes. This modification leads the numerical dissipation term vanishing when free-stream is imposed. A free-stream preserving hybridization, which switches between the modified linear-upwind and WENO schemes, is introduced to improve computational efficiency and reduce numerical dissipation. Extensive numerical examples demonstrate that the proposed method is effective on various non-uniform grids to achieve free-stream and vortex preserving property and keep the shock-capturing ability of the original WENO scheme. Moreover, the present method is applicable to general explicit linear-upwind schemes and other WENO schemes to eliminate the geometrically induced error in curvilinear coordinates.

As an alternative to the aforementioned grid-based method, particle-based method exhibits important advantages in modeling flexible structures with large deformations and complex flows when there present free surfaces or fluid structure interactions [31]. One challenging task for particle-based method is to generate a high-quality body-fitted particle distribution. In the literature, there are generally two approaches for particle generation, i.e., initiating particles on a lattice structure [84] and generating particles based on volume element mesh [85, 86]. For the first approach, a very fine spatial resolution is needed for correct portraying of the geometry surface. The second approach has the drawback that the generated particle spacing and volume may be non-uniform. Compared to these approaches, the present work can achieve the correct portraying of complex surface and uniform particle distributions simultaneously. Using a CAD parser, an arbitrarily complex geometry is accessed from external CAD files, and the corresponding geometry surface is then represented by an implicit zero level-set function [91]. Starting from a pre-conditioned lattice or random particle distribution, a relaxation procedure, where particles evolution is driven by a constant background pressure in the SPH framework, is carried out to regularize particle distribution. An efficient surface bounding method is proposed to achieve body-fitted feature by enforcing particle outside of the domain back to the geometric surface. With this method, a body-fitted well-regularized particle distribution is achieved when the relaxation process approaches to stable. The particle distributions of a number of complex structures demonstrate the efficiency and effectiveness of the proposed method. In addition, a high-quality particle distribution is essential to the consistency of particle-based methods and the improvements of computational accuracy by adopting the proposed method are validated by a physical implementation. Consequently, the proposed method sheds lights on simulating real-world applications for particle-based methods.

4.2 Outlooks

The main part of the present work focuses on improving the stability and consistency for grid- and particle-based numerical methods. A high-resolution scheme for compressible flows and a practicable framework applying the scheme to complex geometries are offered. A high-quality body-fitted particle generator for arbitrarily complex geometries is also provided, implying many potential applications. Several directions for future work are

- The present regularized WENO-IS scheme [45] can be extended to very-high-order (higher than 5th-order) versions for better performance by taking account several incremental stencils. The spectral properties of the scheme should be further studied and optimized by many general approaches, see the strategies in Refs. [69, 70] to minimize dispersion and control suitable dissipation errors. Besides, the present scheme can be applied to simulate compressible and incompressible turbulence for further researches.

- As the present method [46] is developed for stationary grids, the free-stream preserving method for moving grids should also be studied for volume conservation law (VCL) [56, 92]. Moreover, the free-stream preserving schemes can also be implemented to study the flow field with complex geometry, like the flow past airfoils or cylinders, turbulence over a wavy wall, etc.

- Regarding to the present particle generator [24], a supplementary boundary condition, which takes the cut-off cells into consideration, should be studied and implemented to further improve the distributions of boundary particles. The method to generate multi-resolution distributions [93], which is essential for computational efficiency, is attractive and should also be developed.

Bibliography

[1]   J. D. Anderson and J. Wendt. *Computational Fluid Dynamics*. Vol. 206. Springer, 1995.

[2]   H. K. Versteeg and W. Malalasekera. *An introduction to computational fluid dynamics: the finite volume method*. Pearson education, 2007.

[3]   G. R. Liu and M. B. Liu. *Smoothed particle hydrodynamics: a meshfree particle method*. World Scientific, 2003.

[4]   E. Johnsen et al. "Assessment of high-resolution methods for numerical simulations of compressible turbulence with shock waves". In: *Journal of Computational Physics* 229.4 (2010), pp. 1213–1237.

[5]   S. Pirozzoli. "Numerical methods for high-speed flows". In: *Annual Review of Fluid Mechanics* 43 (2011), pp. 163–194.

[6]   Z. J. Wang et al. "High-order CFD methods: current status and perspective". In: *International Journal for Numerical Methods in Fluids* 72.8 (2013), pp. 811–845.

[7]   Z. J. Wang. "High-order methods for the Euler and Navier–Stokes equations on unstructured grids". In: *Progress in Aerospace Sciences* 43.1-3 (2007), pp. 1–41.

[8]   S. K. Godunov. "A difference method for numerical calculation of discontinuous solutions of the equations of hydrodynamics". In: *Matematicheskii Sbornik* 89.3 (1959), pp. 271–306.

[9]   A. Harten et al. "Uniformly high order accurate essentially non-oscillatory schemes, III". In: *Upwind and High-resolution Schemes*. Springer, 1987, pp. 218–290.

[10]   S. K. Lele. "Compact finite difference schemes with spectral-like resolution". In: *Journal of Computational Physics* 103.1 (1992), pp. 16–42.

[11]   X. D. Liu, S. Osher, and T. Chan. "Weighted essentially non-oscillatory schemes". In: *Journal of Computational Physics* 115.1 (1994), pp. 200–212.

[12]   G. S. Jiang and C. W. Shu. "Efficient Implementation of Weighted ENO Schemes". In: *Journal of Computational Physics* 126.1 (1996), pp. 202–228.

[13]   C. Ollivier-Gooch and M. Van Altena. "A high-order-accurate unstructured mesh finite-volume scheme for the advection–diffusion equation". In: *Journal of Computational Physics* 181.2 (2002), pp. 729–752.

[14]   B. Cockburn and C. W. Shu. "Runge–Kutta discontinuous Galerkin methods for convection-dominated problems". In: *Journal of Scientific Computing* 16.3 (2001), pp. 173–261.

[15]   Z. J. Wang and H. Y. Gao. "A unifying lifting collocation penalty formulation including the discontinuous Galerkin, spectral volume/difference methods for conservation laws on mixed grids". In: *Journal of Computational Physics* 228.21 (2009), pp. 8161–8186.

[16] C. W. Shu. "Essentially non-oscillatory and weighted essentially non-oscillatory schemes". In: *Acta Numerica* 29 (2020), pp. 701–762.

[17] C. W. Shu. "High-order finite difference and finite volume WENO schemes and discontinuous Galerkin methods for CFD". In: *International Journal of Computational Fluid Dynamics* 17.2 (2003), pp. 107–118.

[18] P. D. Thomas and C. K. Lombard. "Geometric conservation law and its application to flow computations on moving grids". In: *AIAA journal* 17.10 (1979), pp. 1030–1037.

[19] M. Vinokur. "An analysis of finite-difference and finite-volume formulations of conservation laws". In: *Journal of Computational Physics* 81.1 (1989), pp. 1–52.

[20] M. P. Martín et al. "A bandwidth-optimized WENO scheme for the effective direct numerical simulation of compressible turbulence". In: *Journal of Computational Physics* 220.1 (2006), pp. 270–289.

[21] G. A. Gerolymos, D. Sénéchal, and I. Vallet. "Very-high-order WENO schemes". In: *Journal of Computational Physics* 228.23 (2009), pp. 8481–8524.

[22] M. McAllister et al. "Laboratory recreation of the Draupner wave and the role of breaking in crossing seas". In: *Journal of Fluid Mechanics* 860 (2019), pp. 767–786.

[23] M. Luo et al. "Experimental study of freak wave impacts on a tension-leg platform". In: *Marine Structures* 74 (2020), p. 102821.

[24] Y. J. Zhu et al. "A CAD-compatible body-fitted particle generator for arbitrarily complex geometry and its application to wave-structure interaction". In: *Journal of Hydrodynamics* 33.2 (2021), pp. 195–206.

[25] C. Zhang et al. "A simple artificial damping method for total Lagrangian smoothed particle hydrodynamics". In: *arXiv preprint arXiv:2102.04898* (2021).

[26] R. A. Gingold and J. J. Monaghan. "Smoothed particle hydrodynamics: theory and application to non-spherical stars". In: *Mon. Not. R. Astron. Soc.* 181.3 (1977), pp. 375–389.

[27] L. B. Lucy. "A numerical approach to the testing of the fission hypothesis". In: *The astronomical journal* 82 (1977), pp. 1013–1024.

[28] S. Koshizuka and Y. Oka. "Moving-particle semi-implicit method for fragmentation of incompressible fluid". In: *Nuclear Science and Engineering* 123.3 (1996), pp. 421–434.

[29] B. K. Mishra and R. K. Rajamani. "The discrete element method for the simulation of ball mills". In: *Applied Mathematical Modelling* 16.11 (1992), pp. 598–604.

[30] J. J. Monaghan. "Smoothed Particle Hydrodynamics". In: *Reports on progress in physics* 68.8 (2005), p. 1703.

[31] M. B. Liu and G. R. Liu. "Smoothed particle hydrodynamics (SPH): an overview and recent developments". In: *Archives of Computational Methods in Engineering* 17.1 (2010), pp. 25–76.

[32] J. J. Monaghan. "Smoothed particle hydrodynamics and its diverse applications". In: *Annual Review of Fluid Mechanics* 44 (2012), pp. 323–346.

[33] T. Ye et al. "Smoothed particle hydrodynamics (SPH) for complex fluid flows: Recent developments in methodology and applications". In: *Physics of Fluids* 31.1 (2019), p. 011301.

[34] J. J. Monaghan. "Simulating free surface flows with SPH". In: *Journal of Computational Physics* 110.2 (1994), pp. 399–406.

[35] J. P. Morris, P. J. Fox, and Y. Zhu. "Modeling low Reynolds number incompressible flows using SPH". In: *Journal of Computational Physics* 136.1 (1997), pp. 214–226.

[36] X. Y. Hu and N. A. Adams. "A multi-phase SPH method for macroscopic and mesoscopic flows". In: *Journal of Computational Physics* 213.2 (2006), pp. 844–861.

[37] C. Zhang et al. "A weakly compressible SPH method with WENO reconstruction". In: *Journal of Computational Physics* 392 (2019), pp. 1–18.

[38] W. Benz and E. Asphaug. "Simulations of brittle solids using smooth particle hydrodynamics". In: *Computer Physics Communications* 87.1 (1995), pp. 253–265.

[39] P. W. Randles and L. D. Libersky. "Smoothed particle hydrodynamics: some recent improvements and applications". In: *Computer Methods in Applied Mechanics and Engineering* 139.1 (1996), pp. 375–408.

[40] J. J. Monaghan. "SPH without a tensile instability". In: *Journal of Computational Physics* 159.2 (2000), pp. 290–311.

[41] K. Ba and A. Gakwaya. "Thermomechanical total Lagrangian SPH formulation for solid mechanics in large deformation problems". In: *Computer Methods in Applied Mechanics and Engineering* 342 (2018), pp. 458–473.

[42] C. Antoci, M. Gallati, and S. Sibilla. "Numerical simulation of fluid–structure interaction by SPH". In: *Computers & Structures* 85.11 (2007), pp. 879–890.

[43] C. Zhang, M. Rezavand, and X. Y. Hu. "A multi-resolution SPH method for fluid-structure interactions". In: *Journal of Computational Physics* 429 (2021), p. 110028.

[44] C. Zhang et al. "An integrative smoothed particle hydrodynamics method for modeling cardiac function". In: *Computer Methods in Applied Mechanics and Engineering* 381 (2021), p. 113847.

[45] Y. J. Zhu and X. Y. Hu. "An L2-norm regularized incremental-stencil WENO scheme for compressible flows". In: *Computers & Fluids* 213 (2020), p. 104721.

[46] Y. J. Zhu and X. Y. Hu. "Free-stream preserving linear-upwind and WENO schemes on curvilinear grids". In: *Journal of Computational Physics* 399 (2019), p. 108907.

[47] P. L. Roe. "Approximate Riemann solvers, parameter vectors, and difference schemes". In: *Journal of Computational Physics* 43.2 (1981), pp. 357–372.

[48] E. Hewitt and R. E. Hewitt. "The Gibbs-Wilbraham phenomenon: an episode in Fourier analysis". In: *Archive for History of Exact Sciences* 21.2 (1979), pp. 129–160.

[49] M. Castro, B. Costa, and W. S. Don. "High order weighted essentially non-oscillatory WENO-Z schemes for hyperbolic conservation laws". In: *Journal of Computational Physics* 230.5 (2011), pp. 1766–1792.

[50] A. K. Henrick, T. D. Aslam, and J. M. Powers. "Mapped weighted essentially non-oscillatory schemes: achieving optimal order near critical points". In: *Journal of Computational Physics* 207.2 (2005), pp. 542–567.

[51] R. Borges et al. "An improved weighted essentially non-oscillatory scheme for hyperbolic conservation laws". In: *Journal of Computational Physics* 227.6 (2008), pp. 3191–3211.

[52] X. Y. Hu, Q. Wang, and N. A. Adams. "An adaptive central-upwind weighted essentially non-oscillatory scheme". In: *Journal of Computational Physics* 229.23 (2010), pp. 8952–8965.

[53] X. Y. Hu and N. A. Adams. "Scale separation for implicit large eddy simulation". In: *Journal of Computational Physics* 230.19 (2011), pp. 7240–7249.

[54] B. Wang, G. M. Xiang, and X. Y. Hu. "An incremental-stencil WENO reconstruction for simulation of compressible two-phase flows". In: *International Journal of Multiphase Flow* 104 (2018), pp. 20–31.

[55] S. Gottlieb, C. W. Shu, and E. Tadmor. "Strong stability-preserving high-order time discretization methods". In: *SIAM review* 43.1 (2001), pp. 89–112.

[56] H. Zhang et al. "Discrete form of the GCL for moving meshes and its implementation in CFD schemes". In: *Computers & Fluids* 22.1 (1993), pp. 9–23.

[57] X. G. Deng et al. "Geometric conservation law and applications to high-order finite difference schemes with stationary grids". In: *Journal of Computational Physics* 230.4 (2011), pp. 1100–1115.

[58] T. Nonomura, N. Iizuka, and K. Fujii. "Freestream and vortex preservation properties of high-order WENO and WCNS on curvilinear grids". In: *Computers & Fluids* 39.2 (2010), pp. 197–214.

[59] X. G. Deng et al. "Further studies on geometric conservation law and applications to high-order finite difference schemes with stationary grids". In: *Journal of Computational Physics* 239 (2013), pp. 90–111.

[60] Y. Abe et al. "Geometric interpretations and spatial symmetry property of metrics in the conservative form for high-order finite-difference schemes on moving and deforming grids". In: *Journal of Computational Physics* 260 (2014), pp. 163–203.

[61] G. S. Jiang and C. C. Wu. "A high-order WENO finite difference scheme for the equations of ideal magnetohydrodynamics". In: *Journal of Computational Physics* 150.2 (1999), pp. 561–594.

[62] T. Nonomura et al. "A new technique for freestream preservation of finite-difference WENO on curvilinear grid". In: *Computers & Fluids* 107 (2015), pp. 242–255.

[63] A. Colagrossi and M. Landrini. "Numerical simulation of interfacial flows by smoothed particle hydrodynamics". In: *Journal of Computational Physics* 191.2 (2003), pp. 448–475.

[64] J. J. Monaghan. "Smoothed particle hydrodynamics". In: *Annual Review of Astronomy and Astrophysics* 30.1 (1992), pp. 543–574.

[65] S. Adami, X. Y. Hu, and N. A. Adams. "A transport-velocity formulation for smoothed particle hydrodynamics". In: *Journal of Computational Physics* 241 (2013), pp. 292–307.

[66] S. Litvinov, X. Y. Hu, and N. A. Adams. "Towards consistence and convergence of conservative SPH approximations". In: *Journal of Computational Physics* 301 (2015), pp. 394–401.

[67] C. Zhang, X. Y. Hu, and N. A. Adams. "A generalized transport-velocity formulation for smoothed particle hydrodynamics". In: *Journal of Computational Physics* 337 (2017), pp. 216–232.

[68] E. M. Taylor, M. W. Wu, and M. P. Martín. "Optimization of nonlinear error for weighted essentially non-oscillatory methods in direct numerical simulations of compressible turbulence". In: *Journal of Computational Physics* 223.1 (2007), pp. 384–397.

[69] Z. S. Sun et al. "A class of finite difference schemes with low dispersion and controllable dissipation for DNS of compressible turbulence". In: *Journal of Computational Physics* 230.12 (2011), pp. 4616–4635.

[70] L. Fu, X. Y. Hu, and N. A. Adams. "A family of high-order targeted ENO schemes for compressible-fluid simulations". In: *Journal of Computational Physics* 305 (2016), pp. 333–359.

[71] X. Y. Hu, N. A. Adams, and C. W. Shu. "Positivity-preserving method for high-order conservative schemes solving compressible Euler equations". In: *Journal of Computational Physics* 242 (2013), pp. 169–180.

[72] X. X. Zhang and C. W. Shu. "On positivity-preserving high order discontinuous Galerkin schemes for compressible Euler equations on rectangular meshes". In: *Journal of Computational Physics* 229.23 (2010), pp. 8918–8934.

[73] T. H. Pulliam and J. L. Steger. "Implicit finite-difference simulations of three-dimensional compressible flow". In: *AIAA Journal* 18.2 (1980), pp. 159–167.

[74] M. R. Visbal and D. V. Gaitonde. "On the use of higher-order finite-difference schemes on curvilinear and deforming meshes". In: *Journal of Computational Physics* 181.1 (2002), pp. 155–185.

[75] M. Vinokur and H. C. Yee. "Extension of efficient low dissipation high order schemes for 3-d curvilinear moving grids". In: *Frontiers of Computational Fluid Dynamics 2002*. World Scientific, 2002, pp. 129–164.

[76] Q. Li, D. Sun, and P. X. Liu. "Further study on errors in metric evaluation by linear upwind schemes with flux splitting in stationary grids". In: *Communications in Computational Physics* 22.1 (2017), pp. 64–94.

[77] Y. J. Zhu et al. "A numerical strategy for freestream preservation of the high order weighted essentially non-oscillatory schemes on stationary curvilinear grids". In: *Journal of Scientific Computing* 72.3 (2017), pp. 1021–1048.

[78] M. H. Siemann and S. A. Ritt. "Novel particle distributions for SPH bird-strike simulations". In: *Computer Methods in Applied Mechanics and Engineering* 343 (2019), pp. 746–766.

[79] S. Alimirzazadeh et al. "GPU-accelerated numerical analysis of jet interference in a six-jet Pelton turbine using Finite Volume Particle Method". In: *Renewable Energy* 148 (2020), pp. 234–246.

[80] Z. Ji et al. "Numerical simulations of oil flow inside a gearbox by Smoothed Particle Hydrodynamics (SPH) method". In: *Tribology International* 127 (2018), pp. 47–58.

[81] C. Zhang et al. "An efficient fully Lagrangian solver for modeling wave interaction with oscillating wave surge converter". In: *Ocean Engineering* 236 (2021), p. 109540.

[82] A. J. Crespo et al. "Floating moored oscillating water column with meshless SPH method". In: *ASME 2018 37th International Conference on Ocean, Offshore and Arctic Engineering*. American Society of Mechanical Engineers Digital Collection. 2018.

[83] C. Zhang et al. "An integrative smoothed particle hydrodynamics method for modeling cardiac function". In: *Computer Methods in Applied Mechanics and Engineering* 381 (2021), p. 113847.

[84] J. M. Domínguez et al. "Development of a new pre-processing tool for SPH models with complex geometries". In: *6th International SPHERIC workshop*. 2011, pp. 117–124.

[85] R. Vignjevic et al. "A parametric study of bird strike on engine blades". In: *International Journal of Impact Engineering* 60 (2013), pp. 44–57.

[86] S. Heimbs. "Computational methods for bird strike simulations: A review". In: *Computers & Structures* 89.23-24 (2011), pp. 2093–2112.

[87] S. Diehl et al. "Generating optimal initial conditions for Smoothed Particle Hydrodynamics simulations". In: *Publications of the Astronomical Society of Australia* 32 (2015).

[88] L. V. Vela, R. Sanchez, and J. Geiger. "ALARIC: An algorithm for constructing arbitrarily complex initial density distributions with low particle noise for SPH/SPMHD applications". In: *Computer Physics Communications* 224 (2018), pp. 186–197.

[89] L. Fu and Z. Ji. "An optimal particle setup method with Centroidal Voronoi Particle dynamics". In: *Computer Physics Communications* 234 (2019), pp. 72–92.

[90] Y. Abe et al. "Conservative metric evaluation for high-order finite difference schemes with the GCL identities on moving and deforming grids". In: *Journal of Computational Physics* 232.1 (2013), pp. 14–21.

[91] S. Osher and J. A. Sethian. "Fronts propagating with curvature-dependent speed: Algorithms based on Hamilton-Jacobi formulations". In: *Journal of Computational Physics* 79.1 (1988), pp. 12–49.

[92] B. Sjögreen, H. C. Yee, and M. Vinokur. "On high order finite-difference metric discretizations satisfying GCL on moving and deforming grids". In: *Journal of Computational Physics* 265 (2014), pp. 211–220.

[93] Z. Ji et al. "A new multi-resolution parallel framework for SPH". In: *Computer Methods in Applied Mechanics and Engineering* 346 (2019), pp. 1156–1178.

Appendix A

Original journal papers

Here, the peer-reviewed journal publications of the present work are attached.

A.1   Paper I

Yujie Zhu, Xiangyu Hu

An L2-norm regularized incremental-stencil WENO scheme for compressible flows

Contribution: My contribution to this work was the development of the method and the corresponding computer code for its implementation. I performed simulations and analyzed the results, and wrote the manuscript for the publication.

An L2-norm regularized incremental-stencil WENO scheme for compressible flows

Author: Yujie Zhu,Xiangyu Hu

Publication: Computers & Fluids

Publisher: Elsevier

Date: 15 December 2020

Journal Author Rights

BACK   CLOSE WINDOW

An L2-norm regularized incremental-stencil WENO scheme for compressible flows

Yujie Zhu, Xiangyu Hu[*]

Department of Mechanical Engineering, Technical University of Munich Graching 85748, Germany

ABSTRACT

For the simulation of compressible flow with a broadband of length scales and discontinuities, the WENO schemes using incremental stencil sizes other than uniform ones are promising for more robustness and less numerical dissipation. However, in smooth region, large weights may be assigned to smaller stencils due to the lack of high-order derivatives in the smoothness indicator compared with that of larger stencils, and may degrade the order accuracy especially in the region near critical points. In order to cope with this drawback, based on the stencil selection of WENO-IS [Wang et al., IJMF 104 (2018): 20–31], we propose an L2-norm regularized incremental-stencil WENO scheme in this paper. In order to avoid the above mentioned order degeneration, a new L2-norm regularization is introduced into the WENO weighting strategy by taking account the L2-norm error term. In addition, a high-order non-dimensional discontinuity detector is utilized as the regularization parameter for adaptive control. Then, a hybrid method is adopted to further improve the performance and the computational efficiency. A number of benchmark cases suggest that the present scheme achieves very good robustness and fine-structure resolving capabilities.

© 2020 Elsevier Ltd. All rights reserved.

1. Introduction

The simulation of compressible flow is challenging when there present a broadband of length scales and discontinuities. The numerical schemes must be of low dissipation in smooth region without damping the fine flow structures, and be able to introduce sufficient dissipation in vicinity of discontinuities for suppressing non-physical oscillations. In order to address this issue, many high-order shock capturing schemes, like total variation diminishing (TVD) [1], essentially non-oscillatory (ENO) [2] and weighted essentially non-oscillatory (WENO) [3] schemes, have been developed. Among them, the WENO-JS scheme proposed by Jiang and Shu [4] exhibits high-order accuracy and robust shock-capturing properties and has been extensively employed in direct numerical simulations (DNS) and large eddy simulations (LES). In spite of these advantages, the classic WENO-JS scheme still faces several shortcomings. It suffers from order-degeneration, e.g. not able to recover the formal order of accuracy near critical points where the first or higher derivatives vanish [5], and is too dissipative for sustaining fine structures in turbulence or aeroacoustic flows [6]. Furthermore, the computation may fail when very strong discontinuities exist or multiple discontinuities are too close to each other [7].

In order to overcome the drawbacks of order-degeneration and excessive dissipation of the classical WENO-JS scheme, one approach is to modify the weighting strategy, e.g. the adaptation mechanism, by increasing the weight of the optimal upwind linear scheme in relatively smooth regions. Following this idea, various schemes have been developed, such as WENO-M scheme [5] with a corrective mapping applied to the classical WENO weights, WENO-Z scheme [8,9] with a new high-order smoothness indicator and WENO-RL or WENO-RLTV [10] scheme switching on the optimal weights when the magnitude of smoothness indicators are comparable. Another approach is to introduce the contribution of the downwind stencil and use optimal weights for central scheme instead of upwind scheme as pointed in Refs. [6,11,12]. Take WENO-CU6 scheme [12] as an example, Hu et al. employed the 6th-order central scheme as the optimal linear scheme and introduced a new smooth indicator for the adaptation between central and upwind stencils. Later, this scheme was extended to WENO-CU6-M with a physically-motivated scale separation approach for implicit large eddy simulation (ILES) [13]. While WENO-CU6-M works well for incompressible and compressible turbulence simulation with low dissipation and maintains the shock-capturing capability, it produces spurious waves because of the non-dissipative optimal scheme. In addition, as demonstrated in Ref. [14], one version of

---

* Corresponding author.
E-mail addresses: yujie.zhu@tum.de (Y. Zhu), xiangyu.hu@tum.de (X. Hu).

WENO-CU6-M scheme fails in the benchmark test cases "Interacting blast waves" and "Double Mach reflection" suggesting the inferior robustness compared to the classic WENO-JS scheme. Fu et al. [14] proposed a family of TENO scheme which dynamically assembles a set of low-order candidate stencils with incrementally increasing stencil width. The combination of low-order approximation polynomials with incremental stencils makes TENO scheme considerably more robust. However, positivity-preserving methods, such as those in Ref. [15,16], are still required for TENO schemes when high density ratio or strong shock waves present. Besides, other notable central-upwind schemes with good wave-resolving and shock-capturing properties, like EWCNS [17–19] and EWENO [20,21] schemes, have also been proposed. In these methods, an adaptive parameter is introduced into the nonlinear weights to restrain numerical dissipation in smooth region and to preserve shock capturing around discontinuities.

Recently, Wang et al. [22] developed a 5th-order incremental-stencil WENO (denote as WENO-IS) scheme for multi-phase flows. Since both 2- and 3-point stencils are used, in the region with strong discontinuities, the reconstruction would prefer to choose the 2-point stencils, which makes the scheme, compared to the classic WENO-JS schemes, very robust for material interface with high density ratio and strong shock waves. In their weighting strategy, a slight modification is introduced to decrease the weights for 2-point stencils in relatively smooth region and to avoid excessive dissipation and order degeneration near critical points. However, for single-phase flow with shocks and broadband waves, this scheme is too dissipative to capture fine flow structures, as also shown in Section 4, due to the still too much weights for the 2-point stencils.

In this paper, we propose an L2-norm regularized incremental-stencil WENO scheme following the idea of neural-network optimization [23]. Similar to WENO-IS scheme, the incremental 2- and 3-point stencils are used for the 5th-order reconstruction. The difference is that an L2-norm regularization is introduced to address the problem of order degeneration and excessive dissipation. First, the L2-norm errors between the approximations from 2-point stencils and classical 3-point stencils are utilized to modulate the weights of the incremental stencils. Then, a high-order non-dimensional discontinuity detector is adopted as the regularization parameter to control the influence of the error term. With a further hybridization with a linear scheme, less numerical dissipation in very smooth region and considerable higher computational efficiency are achieved. The reminder of the paper is organized as follows. Section 2 gives a brief review of the WENO-IS scheme following Wang et al. [22] and the application of WENO-IS to Euler equations is given. In Section 3, the L2-norm regularization and control parameter are proposed. Benchmark test cases with strong discontinuities and fine flow structures are presented in Section 4, and brief concluding remarks are given in the last Section 5.

2. WENO-IS Scheme

In this section, we briefly review the 5th-order WENO-IS scheme for hyperbolic conservation laws following Ref. [22]. First, we illustrate the details of WENO-IS scheme based on the discretization of one-dimensional scalar hyperbolic conservation law. Then, its application in Euler equations is given.

2.1. Semi-discretization of a hyperbolic conservation law

For simplicity, we consider the following one-dimensional scalar hyperbolic conservation law

$$\frac{\partial u}{\partial t} + \frac{\partial f(u)}{\partial x} = 0, \tag{1}$$

where u denotes the conservative variable and $f(u)$ is the flux function. Here, the characteristic velocity is assumed to be positive with $\frac{\partial f(u)}{\partial u} > 0$.

On a uniform grid, we denote $x_j = j\Delta x$, where Δx is the grid spacing. The quantities at the point x_j are identified by the subscript j. The semi-discretized form of Eq. (1) using the method of lines can be approximated by a conservative finite difference scheme as

$$\frac{du_j}{dt} = -\frac{1}{\Delta x}\big(h_{j+1/2} - h_{j-1/2}\big), \tag{2}$$

where $h_{j\pm1/2} = h(x_{j\pm1/2})$ and is implicitly defined by

$$f[u(x)] = \frac{1}{\Delta x} \int_{x-\Delta x/2}^{x+\Delta x/2} h(\xi)d\xi. \tag{3}$$

Numerically, $h_{j\pm1/2}$ are approximated by high-order polynomial interpolations $\widehat{f}_{j\pm1/2}$ or numerical fluxes and Eq. (2) can be expressed as

$$\frac{du_j}{dt} \approx -\frac{1}{\Delta x}\big(\widehat{f}_{j+1/2} - \widehat{f}_{j-1/2}\big). \tag{4}$$

2.2. Candidate stencils with incremental width

For 5th-order WENO-IS scheme, the 5-point stencil S_5 as shown in Fig. 1 is served as the full stencil for the evaluation of numerical fluxes $\widehat{f}_{j+1/2}$. Different from the classic WENO-JS scheme, which subdivides the full stencil into three stencils with the same width, the WENO-IS scheme uses four stencils with incremental width including two 2-point and two 3-point stencils, e.g. S_0, S_1, S_2 and S_3 as shown in Fig. 1, for reconstruction.

The numerical flux $\widehat{f}_{j+1/2}$ is computed by a convex combination of the four candidate stencils fluxes as

$$\widehat{f}_{j+1/2} = \sum_{k=0}^{3} \omega_k \widehat{f}_{k,j+1/2}, \tag{5}$$

where $\widehat{f}_{k,j+1/2}$ and ω_k are the reconstructed fluxes by candidate stencils and their non-linear weights, respectively. These reconstructed fluxes are

$$\widehat{f}_{0,j+1/2} = \frac{1}{2}f_j + \frac{1}{2}f_{j+1},$$

$$\widehat{f}_{1,j+1/2} = -\frac{1}{2}f_{j-1} + \frac{3}{2}f_j,$$

$$\widehat{f}_{2,j+1/2} = \frac{1}{3}f_j + \frac{5}{6}f_{j+1} - \frac{1}{6}f_{j+2},$$

$$\widehat{f}_{3,j+1/2} = \frac{1}{3}f_{j-2} - \frac{7}{6}f_{j-1} + \frac{11}{6}f_j. \tag{6}$$

From Taylor series expansion, we can obtain

$$\widehat{f}_{k,j+1/2} = h_{j+1/2} + A_k\Delta x^{r_k} + O\big(\Delta x^{r_k+1}\big), \tag{7}$$

where A_k is a constant and may be different for different candidate stencils. r_k denotes the points of the candidate stencil.

The non-linear weights ω_k are given by

$$\omega_k = \frac{\alpha_k}{\sum_{s=0}^{3}\alpha_s}, \quad \alpha_k = d_k\Big(1 + \frac{\tau_5}{\beta_k+\varepsilon}\Big), \tag{8}$$

where coefficients $d_0 = \frac{4}{10}, d_1 = \frac{2}{10}, d_2 = \frac{3}{10}, d_3 = \frac{1}{10}$ are the optimal weights and ε is a small positive parameter to prevent division by zero and we choose $\varepsilon = 10^{-20}$ in this paper. β_k are the smoothness indicators of each candidate stencil, while τ_5 is the global reference smoothness indicator on the full stencil. Following Jiang and Shu [4], the smoothness indicators at S_k are evaluated by

$$\beta_k = \sum_{l=1}^{r_k-1} \Delta x^{2l-1} \int_{x_{j-1/2}}^{x_{j+1/2}} \left(\frac{d^l}{dx^l}\widehat{f}_k(x)\right)^2 dx. \tag{9}$$
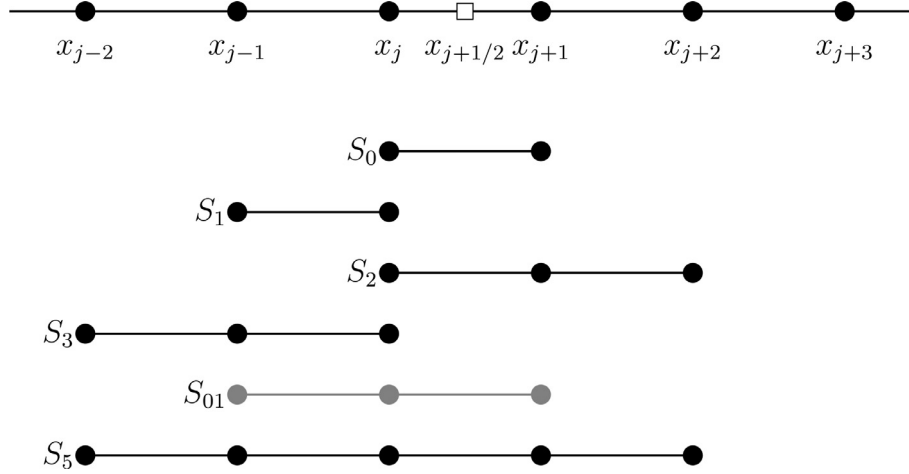
Fig. 1. Full stencil and candidate stencils with incremental width for WENO-IS reconstruction. Here, S_{01} is an original 3-point stencil used for WENO-JS reconstruction.

The global reference smoothness indicator is obtained by

$$\tau_5 = \sum_{l=3}^{4} \Delta x^{2l-1} \int_{x_{j-1/2}}^{x_{j+1/2}} \left(\frac{d^l}{dx^l}\widehat{f}_k(x)\right)^2 dx, \tag{10}$$

which only contains the high-order component of the smoothness indicator for the full stencil [14,22]. The formulations of β_k and τ_5 in terms of cell-centered fluxes f_j can be expressed as

$$\beta_0 = \left(f_{j+1} - f_j\right)^2,$$

$$\beta_1 = \left(f_j - f_{j-1}\right)^2,$$

$$\beta_2 = \frac{13}{12}\left(f_j - 2f_{j+1} + f_{j+2}\right)^2 + \frac{1}{4}\left(3f_j - 4f_{j+1} + f_{j+2}\right)^2,$$

$$\beta_3 = \frac{13}{12}\left(f_{j-2} - 2f_{j-1} + f_j\right)^2 + \frac{1}{4}\left(f_{j-2} - 4f_{j-1} + 3f_j\right)^2,$$

$$\tau_5 = \frac{13}{12}\left(f_{j+2} - 4f_{j+1} + 6f_j - 4f_{j-1} + f_{j-2}\right)^2$$
$$+ \frac{1}{4}\left(f_{j+2} - 2f_{j+1} + 2f_{j-1} - f_{j-2}\right)^2, \tag{11}$$

and their Taylor series expansions at x_j are

$$\beta_0 = f'^2_j \Delta x^2 + f'_j f''_j \Delta x^3 + \left(\frac{1}{4}f''^2_j + \frac{1}{3}f'_j f'''_j\right)\Delta x^4$$
$$+ \left(\frac{1}{12}f'_j f''''_j + \frac{1}{6}f''_j f'''_j\right)\Delta x^5 + O\left(\Delta x^6\right),$$

$$\beta_1 = f'^2_j \Delta x^2 - f'_j f''_j \Delta x^3 + \left(\frac{1}{4}f''^2_j + \frac{1}{3}f'_j f'''_j\right)\Delta x^4$$
$$- \left(\frac{1}{12}f'_j f''''_j + \frac{1}{6}f''_j f'''_j\right)\Delta x^5 + O\left(\Delta x^6\right),$$

$$\beta_2 = f'^2_j \Delta x^2 + \left(\frac{13}{12}f''^2_j - \frac{2}{3}f'_j f'''_j\right)\Delta x^4$$
$$+ \left(-\frac{1}{2}f'_j f''''_j + \frac{13}{6}f''_j f'''_j\right)\Delta x^5 + O\left(\Delta x^6\right),$$

$$\beta_3 = f'^2_j \Delta x^2 + \left(\frac{13}{12}f''^2_j - \frac{2}{3}f'_j f'''_j\right)\Delta x^4$$
$$- \left(-\frac{1}{2}f'_j f''''_j + \frac{13}{6}f''_j f'''_j\right)\Delta x^5 + O\left(\Delta x^6\right),$$

$$\tau_5 = f'''_j \Delta x^6 + \frac{13}{12}f''''_j \Delta x^8 + O\left(\Delta x^{10}\right). \tag{12}$$

Substituting Eqs. (12) to (8), we can observe that

$$\frac{\tau_5}{\beta_k + \varepsilon} = O\left(\Delta x^4\right), \quad k = 0, 1, 2, 3. \tag{13}$$

Therefore, the condition of $\omega_k - d_k = O\left(\Delta x^4\right)$ is satisfied at the region without critical points, implying that the WENO-IS scheme has the expected 5th-order convergence from the analysis in Ref. [22].

2.3. Weighting strategy

From Eqs. (9) and (11), we can observe that the smoothness indicators of 2-point stencils are evaluated from the 1st-order derivatives of linear functions, while these of 3-point stencils are from the 1st and 2nd-order derivatives of parabolic functions. Due to the lack of 2nd-order derivative term, the smoothness indicator of 2-point stencils can be much smaller than that of stencils with 3-point especially near critical points and larger weights will be posed on 2-point stencils, which may cause order degeneration eventually. In order to address this issue, Wang et al. [22] made a slight modification of the weighting strategy in Eq. (8) as

$$\alpha_0 = d_0\left(1 + \frac{\tau_5}{\beta_0 + \varepsilon}\cdot\frac{\tau_5}{\beta_{01} + \varepsilon}\right), \quad \alpha_1 = d_1\left(1 + \frac{\tau_5}{\beta_1 + \varepsilon}\cdot\frac{\tau_5}{\beta_{01} + \varepsilon}\right), \tag{14}$$

where

$$\beta_{01} = \frac{13}{12}\left(f_{j-1} - 2f_j + f_{j+1}\right)^2 + \frac{1}{4}\left(f_{j-1} - f_{j+1}\right)^2 \tag{15}$$

is the smoothness indicator of S_{01}, an original 3-point stencil of WENO-JS as shown in Fig. 1, and is obtained from 1st and 2nd-order derivatives. This modification decreases the weights of 2-point stencils considerably and avoids order degeneration at critical points.

In relatively smooth region, the effectiveness of this modification has been confirmed by a number of test cases in Ref. [22]. The WENO-IS scheme achieves the formal order of accuracy and produces less errors than classical WENO-JS scheme. However, in the region with shocks or high wavenumber waves, this modification may not decrease the weights of 2-point stencils sufficiently, which can still lead to excessive numerical dissipation. Suppose there is a shock locating in stencil S_3 and the solutions in stencils S_0, S_1 and S_2 are smooth (see Fig. 1). Under this condition, τ_5 is comparable to β_3 and $\tau_5 = O(1)$, while $\beta_k = O\left(\Delta x^2\right)$ ($k = 0, 1, 2, 01$) are all small numbers. It is straightforward to show that

$$\frac{\tau_5}{\beta_0 + \varepsilon}\cdot\frac{\tau_5}{\beta_{01} + \varepsilon} \gg \frac{\tau_5}{\beta_2 + \varepsilon}, \quad \frac{\tau_5}{\beta_1 + \varepsilon}\cdot\frac{\tau_5}{\beta_{01} + \varepsilon} \gg \frac{\tau_5}{\beta_2 + \varepsilon}, \tag{16}$$

which means larger weights will be posed on 2-point stencils. Same conclusion can be drawn when the shock locates in other

stencils. Thus, this modification enlarges the numerical dissipation near discontinuities. Although larger numerical dissipation improves the robustness of the scheme, this modification imposes too much excessive numerical dissipation to resolve fine flow structures with broadband length scales well (also see the cases in Section 4).

Note that TENO scheme [14] avoids the problem of large weight posed on low-order stencils by an ENO-like strategy. However, the numerical stability of TENO scheme is inferior to WENO-JS hence also WENO-IS scheme.

2.4. Application in Euler equations

For simplicity, the detailed procedure on the application of WENO-IS for Euler equations is illustrated based on the one-dimensional Euler equations of gas dynamics

$$\frac{\partial \boldsymbol{U}}{\partial t} + \frac{\partial \boldsymbol{F}(\boldsymbol{U})}{\partial x} = 0, \tag{17}$$

where

$$\boldsymbol{U} = \begin{bmatrix} \rho \\ \rho u \\ E \end{bmatrix}, \boldsymbol{F}(\boldsymbol{U}) = \begin{bmatrix} \rho u \\ \rho u^2 + p \\ (E+p)u \end{bmatrix}. \tag{18}$$

Here, ρ is density, p is pressure and u denotes the velocity in x−direction. $E = p/(\gamma - 1) + 1/2\rho u^2$ is total energy per unit volume with ideal-gas equation of states used.

Within a uniform grid, at the point x_j, the semi-discretized form of Eq. (17) gives

$$\frac{d\boldsymbol{U}_j}{dt} = -\frac{1}{\Delta x}\big(\hat{\boldsymbol{F}}_{j+1/2} - \hat{\boldsymbol{F}}_{j-1/2}\big), \tag{19}$$

where $\hat{\boldsymbol{F}}_{j\pm1/2}$ are the numerical fluxes at $x_{j\pm1/2}$. With a typical characteristic-wise method, the numerical fluxes are reconstructed within the local characteristic flied. The procedure to obtain $\hat{\boldsymbol{F}}_{j+1/2}$ includes the following steps:

(1) At $x_{j+1/2}$, evaluate the Jacobian matrix $\boldsymbol{A} = \partial \boldsymbol{F}/\boldsymbol{U}$ at a Roe-average state.
(2) Compute the left and right eigenvector matrix $\boldsymbol{L}_{j+1/2}^s$, $\boldsymbol{R}_{j+1/2}^s (s = 1, 2, 3)$ as well as the eigenvalues $\lambda_{j+1/2}^s (s = 1, 2, 3)$ of the Roe-average Jacobian matrix $\boldsymbol{A}$.
(3) Within each candidate stencils, transform the physical fluxes and conservative variables into characteristic filed as

$$v_m^s = \boldsymbol{L}_{j+1/2}^s \cdot \boldsymbol{U}_m, \quad g_m^s = \boldsymbol{L}_{j+1/2}^s \cdot \boldsymbol{F}_m, \tag{20}$$

where $j - 2 \leq m \leq j + 3$ and $s = 1, 2, 3$.
(4) Carry out flux splitting in characteristic space. We can obtain

$$f_m^{s,\pm} = \frac{1}{2}(g_m^s \pm \alpha^s v_m^s), \tag{21}$$

where $\alpha^s = \left|\lambda_{j+1/2}^s\right|$ for Roe flux (RF) splitting. Otherwise, $\alpha^s = max\left|\lambda_l^s\right|$ for Lax-Friedrichs flux (LF) splitting with l representing the entire computational domain or for local Lax-Friedrichs flux (LLF) splitting when l represents the local stencil.
(5) Then, reconstruct the numerical flux with WENO-IS scheme, which gives

$$f_{j+1/2}^{s,+} = \sum_{k=0}^{3} \omega_k^+ f_{k,j+1/2}^{s,+}, \quad f_{j+1/2}^{s,-} = \sum_{k=0}^{3} \omega_k^- f_{k,j+1/2}^{s,-}, \tag{22}$$

where $f_{k,j+1/2}^{s,+}$ and ω_k^+ are the positive fluxes by candidate stencils and their non-linear weights as defined in Eq. (6) and Eq. (8), respectively. The negative terms $f_{k,j+1/2}^{s,-}$ and ω_k^- can be computed in the similar way according to the symmetry at the point $x_{j+1/2}$. The numerical flux in each characteristic space can be finally evaluated by

$$\hat{f}_{j+1/2}^s = f_{j+1/2}^{s,+} + f_{j+1/2}^{s,-}. \tag{23}$$

(6) At last, transform the numerical flux back into physical space as

$$\hat{\boldsymbol{F}}_{j+1/2} = \sum_{s=0}^{2} \boldsymbol{R}_{j+1/2}^s \hat{f}_{j+1/2}^s. \tag{24}$$

3. An L2-norm regularized WENO-IS scheme

In Ref. [23] (their section 3.2.1), in order to find a way to reduce overfitting of the neural-network, an optimization technique, known as L2-norm regularization, is introduced. The essential idea of L2-norm regularization is to add an extra term, called the regularization term, to the original cost function which only contains the L2-norm error term, with a hyper-parameter to control the relative amount of regularization. This technique can be viewed as a way of compromising between the original L2-norm error term and the L2-norm regularization term, which makes the neural-network better at generalizing beyond the training data.

In the classical WENO schemes, as an analog of optimization technique, we can find that only the regularization terms based on the smoothness indicators are utilized. The L2-norm error term is neglected due to the same order of accuracy for each candidate stencil. However, for WENO-IS scheme, the reconstruction accuracy of 2-point stencil is different from that of the 3-point stencil, therefore, neglecting the L2-norm error terms is not suitable anymore. To cope with the discrepancy of numerical accuracy between 2-point and 3-point stencils, an optimization strategy, L2-norm regularization, is introduced to the WENO weighting strategy.

3.1. L2-norm regularization

For the conservation law in Eq. (1), a form of L2-norm error term is

$$E_k = \frac{1}{\Delta x} \int_{x_{j-1/2}}^{x_{j+1/2}} \big(\widehat{f}_k(x) - f_k(x)\big)^2 dx, \tag{25}$$

which is obtained by the difference between reconstruct flux and reference flux. For the 5th-order WENO-IS scheme, the three reconstructed fluxes of classic WENO-JS scheme are chosen as the reference fluxes. Therefore, the L2-norm error term of each stencil for WENO-IS scheme can be evaluated by

$$E_0 = \frac{1}{\Delta x} \int_{x_{j-1/2}}^{x_{j+1/2}} \big(\widehat{f}_0(x) - f_{01}(x)\big)^2 dx,$$

$$E_1 = \frac{1}{\Delta x} \int_{x_{j-1/2}}^{x_{j+1/2}} \big(\widehat{f}_1(x) - f_{01}(x)\big)^2 dx,$$

$$E_2 = \frac{1}{\Delta x} \int_{x_{j-1/2}}^{x_{j+1/2}} \big(\widehat{f}_2(x) - f_2(x)\big)^2 dx,$$

$$E_3 = \frac{1}{\Delta x} \int_{x_{j-1/2}}^{x_{j+1/2}} \big(\widehat{f}_3(x) - f_3(x)\big)^2 dx, \tag{26}$$

where $f_{01}(x)$, $f_2(x)$ and $f_3(x)$ are the reconstructed fluxes of the corresponding stencils S_{01}, S_2 and S_3 as shown in Fig. 1. Since the reconstructed fluxes and the reference fluxes of stencil S_2 and S_3 are the same, their L2-norm error terms equal to zero accordingly. Therefore, the above error terms yield

$$E_0 = \frac{1}{45}\big(f_{j+1}^2 - 4f_j f_{j+1} + 2f_{j-1}f_{j+1} + 4f_j^2 - 4f_{j-1}f_j + f_{j-1}^2\big),$$

$$E_1 = \frac{1}{45}\big(f_{j+1}^2 - 4f_j f_{j+1} + 2f_{j-1}f_{j+1} + 4f_j^2 - 4f_{j-1}f_j + f_{j-1}^2\big),$$

$$E_2 = 0,$$

$$E_3 = 0. \tag{27}$$

With L2-norm regularization, the weighting strategy of WENO-IS scheme is modified as

$$\omega_k^r = \frac{\alpha_k^r}{\sum_{s=0}^3 \alpha_s^r}, \quad \alpha_k^r = d_k \left(1 + \frac{\lambda \tau_5}{\lambda \beta_k + E_k + \varepsilon} \right), \tag{28}$$

where λ is known as the regularization parameter and we will discuss it in later subsection. The Taylor series expansions at x_j of the L2-norm error term E_k as shown in Eq. (27) are

$$E_0 = E_1 = \frac{1}{45} \left(f''_j \Delta x^4 + \frac{1}{6} f''_j f''''_j \Delta x^6 + O\left(\Delta x^6\right) \right),$$
$$E_2 = E_3 = 0. \tag{29}$$

It is straightforward to check from Eq. (12) that $\omega_k^r - d_k = O\left(\Delta x^4\right)$ is still satisfied for the present weighting strategy. Hence, with L2-norm regularization the modified WENO-IS scheme also has the expect 5th-order convergence in smooth solution without critical point. Note that, this modification doesn't solve the order degeneration problem at the points with first order derivatives vanish or discontinuities. Although some weighting strategies can be applied to cope with this case as noted by Borges et al. [8], it will increase numerical dissipation inevitably. Alternatively, in the present paper, we introduce a hybrid scheme to resolve the order degeneration problem in smooth region, which will be discussed in Section 3.3.

3.2. An adaptive weights control

It is obvious that the effect of the regularization is to make up the discrepancy of numerical accuracy between 2-point and 3-point stencils so as to reduce the weights of 2-point stencils. The relative importance of the regularization term and the added L2-norm error term depends on the value of λ. Here, we introduce a non-dimensional discontinuity detector following Hu et al. [24] to devise an adaptive regularization parameter. Due to the design of non-dimensional discontinuity detector is based on Euler equations, in this section, the detailed procedure is illustrated using one dimensional Euler equations as presented in Section 2.3.

Noticing that the characteristic variables have dimension of density [24], the non-dimensional discontinuity detector can be thus defined by

$$\sigma^s = \left(\frac{\Delta v_{j+\frac{1}{2}}^s}{\tilde{\rho}} \right)^2, \tag{30}$$

where

$$\Delta v_{j+\frac{1}{2}}^s = \frac{1}{60} \boldsymbol{L}_{j+\frac{1}{2}}^s \cdot \left(\boldsymbol{U}_{j-2} - 5\boldsymbol{U}_{j-1} + 10\boldsymbol{U}_j - 10\boldsymbol{U}_{j+1} + 5\boldsymbol{U}_{j+2} - \boldsymbol{U}_{j+3} \right), \tag{31}$$

and $\tilde{\rho}$ is the Roe-average density corresponding to the Jacobian matrix $\boldsymbol{A}$ at $x_{j+\frac{1}{2}}$. $\boldsymbol{L}_{j+\frac{1}{2}}^s$ is the sth left eigenvector of the Jacobian matrix.

We define a regularization parameter by

$$\lambda = \sigma^s. \tag{32}$$

When the full 6-point stencil contains discontinuities, the regularization parameter becomes a large number, which makes the original smoothness indicator the leading term and 2-point stencils will be assigned larger weights. Note that, the relatively large weights of 2-point stencils evaluated by the present method are less than these of the original WENO-IS scheme under this condition. As will be shown in Section 4, with this treatment the scheme is still robust even for strong discontinuities and less numerical dissipation is imposed. Otherwise, the reconstruction prefers to choose 3-point stencils in the flow field with fine flow structures or the smooth region where λ is small. This adaptive regularization parameter helps the scheme decrease numerical dissipation in the
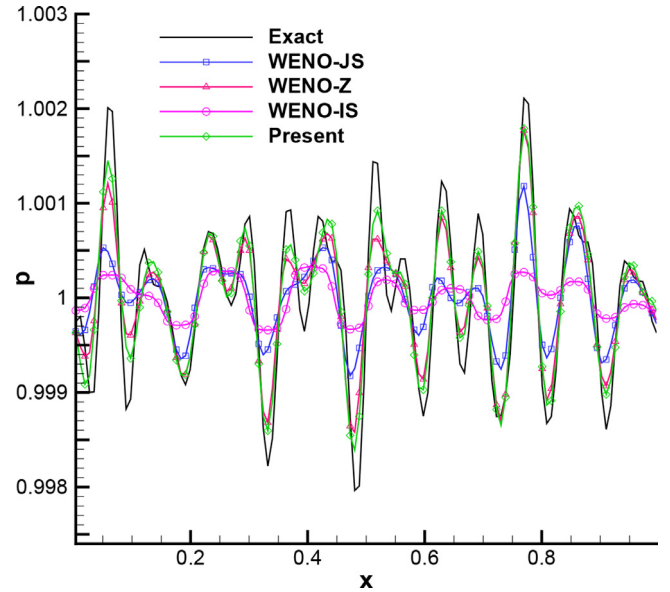

Fig. 2. Broadband wave propagation: density profile with $k_0 = 12$.

region with fine flow structures as well as shocklets and keep well shock capturing properties.

3.3. The hybrid scheme

Although the added L2-norm error term and the designed adaptive parameter have the advantages as discussed above, the modified WENO-IS scheme is not suitable for smooth region due to the preference of 3-point stencil of the reconstruction when λ is small. Furthermore, compared with its optimal linear scheme, the calculation of the modified WENO-IS scheme is time-consuming. To overcome these limitations, with the discontinuity detector presented in above section, it is easy to introduce a hybrid scheme flowing Hu et al. [24] to achieve good spectral properties in the smooth region and improve computational efficiency. The numerical flux of this hybrid scheme is switching from that of the nonlinear WENO-IS scheme and its optimal linear upwind scheme, which is given by

$$\hat{\boldsymbol{F}}_{j+1/2} = \sigma_{j+1/2} \hat{\boldsymbol{F}}_{j+1/2}^{UPS} + \left(1 - \sigma_{j+1/2}\right) \hat{\boldsymbol{F}}_{j+1/2}^{WENO-IS}, \tag{33}$$

where $\sigma_{j+1/2}$ equals to one in smooth region otherwise zero in vicinity of discontinuities. Here, the numerical flux $\hat{\boldsymbol{F}}_{j+1/2}^{UPS}$ of the optimal linear upwind scheme is evaluated by

$$\hat{\boldsymbol{F}}_{j+1/2}^{UPS} = \frac{1}{60} \left(\boldsymbol{F}_{j-2} - 8\boldsymbol{F}_{j-1} + 37\boldsymbol{F}_j + 37\boldsymbol{F}_{j+1} - 8\boldsymbol{F}_{j+2} + \boldsymbol{F}_{j+3} \right)$$
$$+ \frac{1}{60} \sum_{s=0}^2 \boldsymbol{R}_{j+1/2}^s \lambda^s \boldsymbol{L}_{j+1/2}^s \cdot \left(\boldsymbol{U}_{j-2} - 5\boldsymbol{U}_{j-1} \right.$$
$$\left. + 10\boldsymbol{U}_j - 10\boldsymbol{U}_{j+1} + 5\boldsymbol{U}_{j+2} - \boldsymbol{U}_{j+3} \right). \tag{34}$$

It is obvious that this linear scheme omits the computation of the nonlinear weights as presented in Eq. (8) and (22), and decreases by 5/6 the characteristic-projection operations of Eq. (20) as noted in Ref. [24]. Therefore, the hybridization will save much computational time. In addition, the high-order accuracy with less numerical dissipation of this linear scheme will improve the spectral properties of the scheme in smooth region.

The threshold is defined as

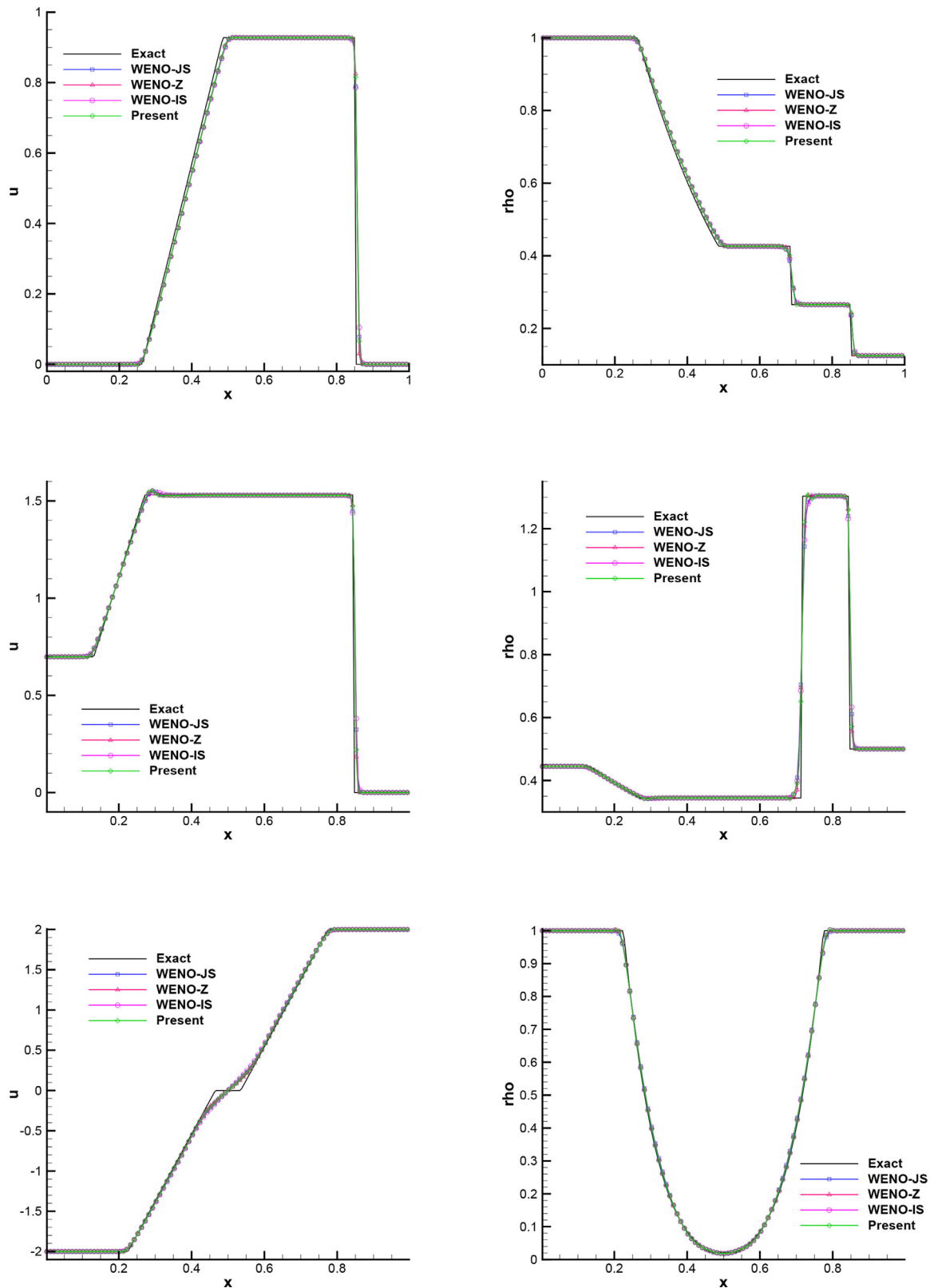$$\epsilon = C \left(\frac{\Delta x}{L} \right)^\alpha, \tag{35}$$

Fig. 3. Shock tube problems: velocity and density profiles of Sod (top), Lax (middle) and 123 problems (bottom).

where L is the characteristic length scale of the problem, α is a positive integer and C is a positive constant. In this paper, we choose $C = 1$ and $\alpha = 3$. When $\sigma^s < \epsilon$, we think the flow field is smooth enough and numerical flux is evaluated by the optimal linear upwind scheme. Otherwise, it is obtained by the regularized WENO-IS scheme.

Note that, many other hybrid methods have also been proposed based on various shock sensors. A recent example is the one in Ref. [25]., which judges the regularity of solution based on the dis-
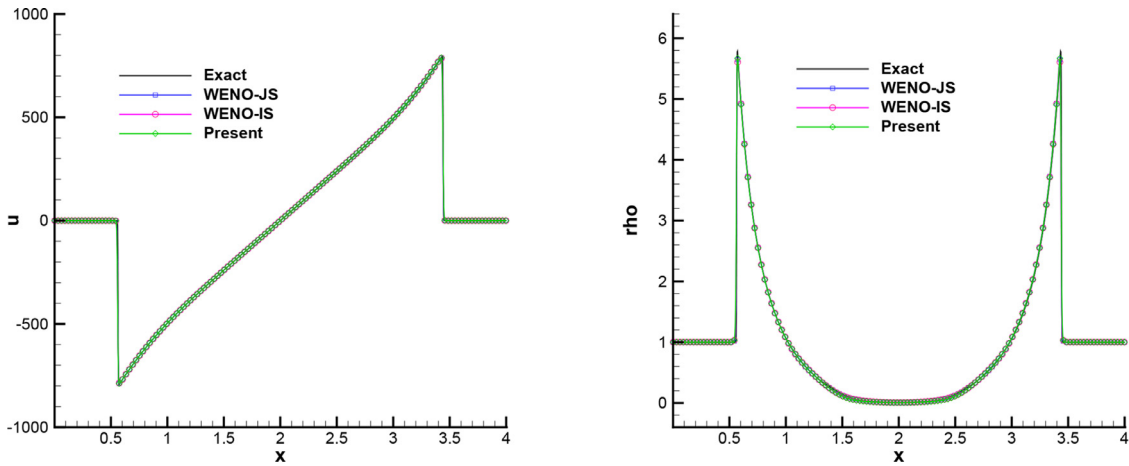
Fig. 4. Sedov blast wave problem: velocity (left) and density profiles (right).
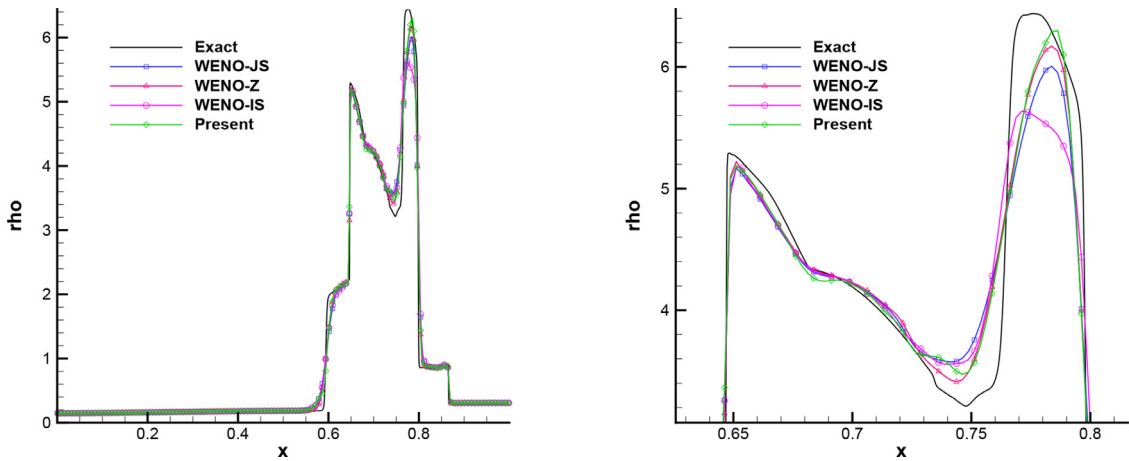
Fig. 5. Interacting blast waves: density profile (left) and a zoom of the density profile (right).
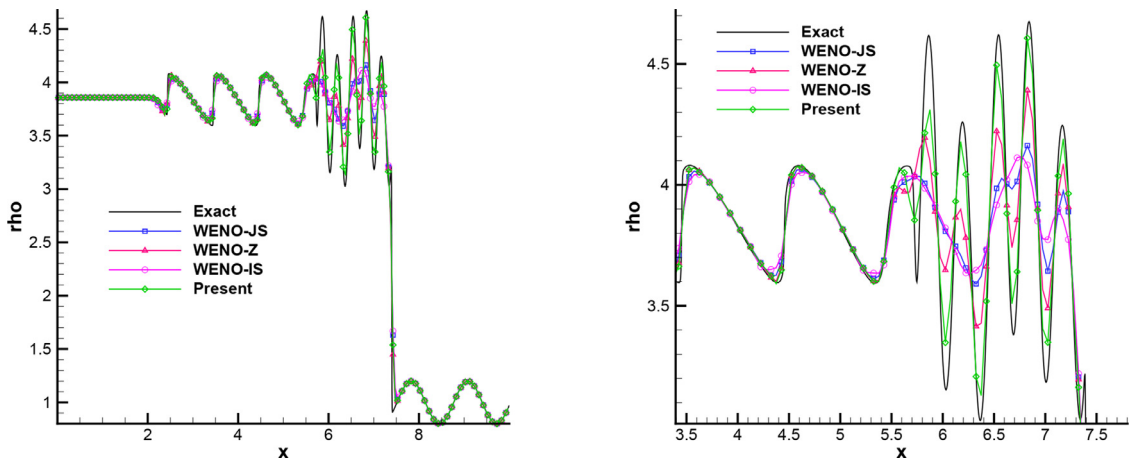

Fig. 6. Shu-osher problem: density profile (left) and a zoom of the density profile (right).

tance between the WENO weights from their ideal values on all the sub-stencils. Although good performance has been achieved by these shock sensors, they are not able to be applied directly to the present method because they are not relevant to the regularization parameter in the weighting strategy, see Eq. (30), as the present hybridization.

4. Numerical cases

In order to assess the performance of the proposed scheme, various test cases are considered, including shock tube problems, shock/entropy wave interaction problems and a problem involving very strong discontinuities. In this section, the local Lax-Friedrichs
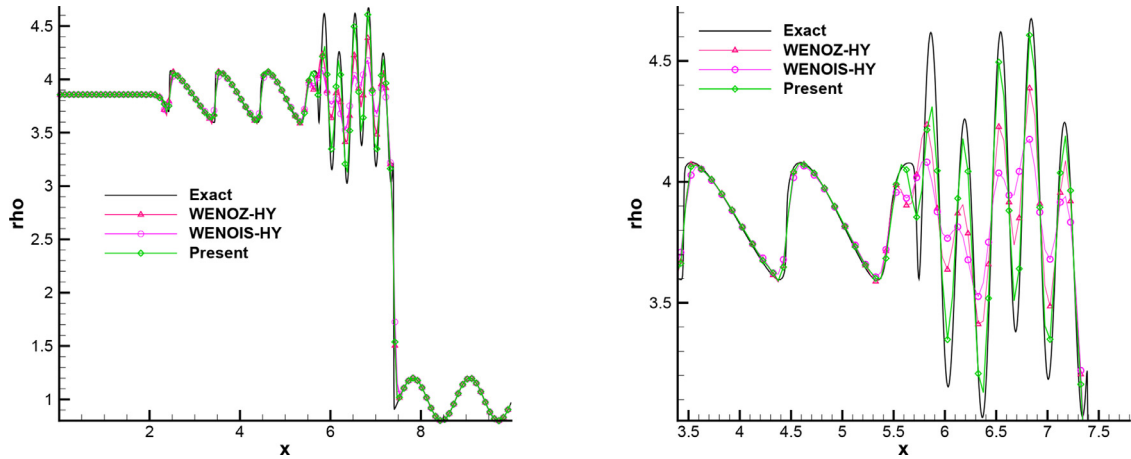
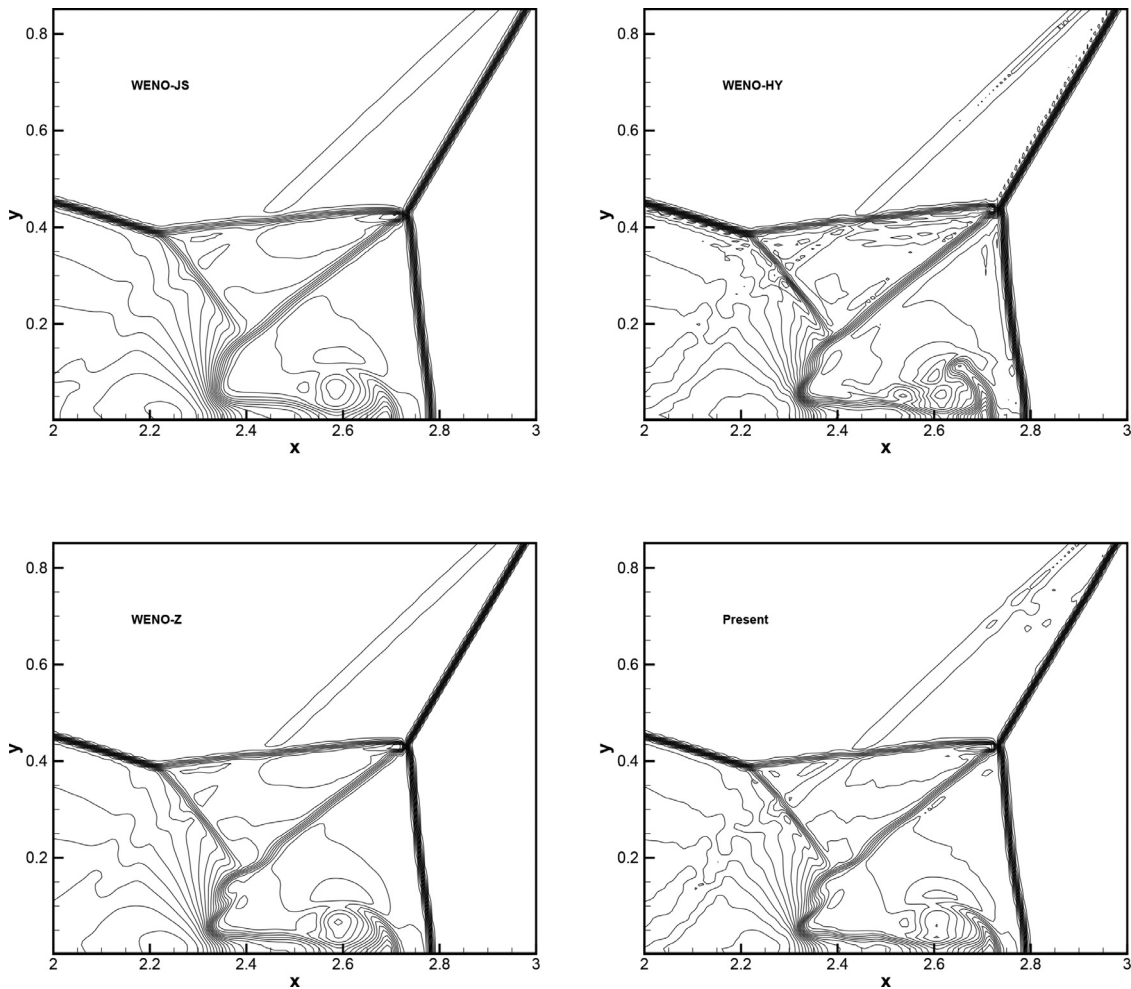**Fig. 7.** Shu-osher problem: the comparison with hybrid method.

Fig. 8. Density profiles of double Mach reflection of a strong shock on the 512 × 128 grid. 43 density contours between 1.887 and 20.9 are shown in this figure.

flux is adopted for flux splitting in one dimensional cases, while Lax-Friendrichs flux is used for two dimensional cases if not mentioned otherwise. The third order TVD Runge-Kutta scheme is utilized for time integration with a CFL number of 0.5. In the following, "WENO-JS" denotes the classical 5th-order WENO scheme [4], "WENO-Z" represents the scheme devised in Ref. [8], "WENO-IS" denotes the original scheme in Ref. [22], "WENO-HY" is the hybrid

method devised by Hu et al. [24], "Present" is the proposed scheme of this paper, and "Exact" denotes the theoretical or convergent solution.

4.1. Propagation of broadband sound waves

This case is taken form Ref. [11]. A propagation of sound wave packet which contains various length scales of acoustic turbulent
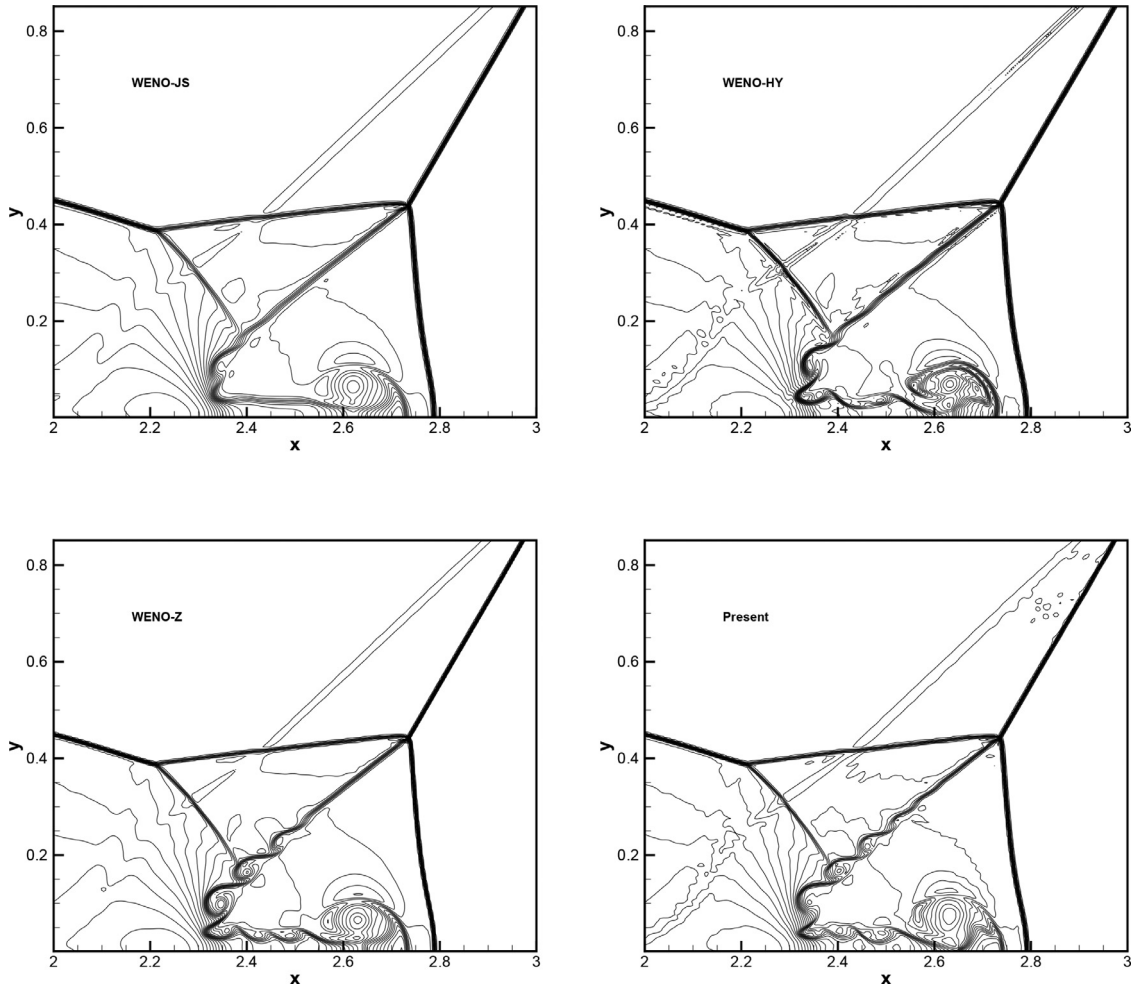
Fig. 9. Density profiles of double Mach reflection of a strong shock on the 1024 × 256 grid. 43 density contours between 1.887 and 20.9 are shown in this figure.

structures is computed. The initial condition is given as

$$p(x, 0) = p_0 \left(1 + \varepsilon \sum_{k=0}^{N/2} (E_p(k))^{1/2} sin(2\pi k(x + \phi_k)) \right),$$

$$\rho(x, 0) = \rho_0 (p(x, 0)/p_0)^{1/\gamma},$$

$$u(x, 0) = u_0 + \frac{2}{\gamma - 1} (c(x, 0)/c_0), \tag{36}$$

where

$$E_p(k) = \left(\frac{k}{k_0} \right)^4 exp^{-2(k/k_0)^2} \tag{37}$$

is the energy spectrum which reaches its maximum at $k = k_0$. Here, ϕ_k is a random number between 0 and 1, $\varepsilon = 0.001$, $\gamma = 1.4$ and the sound speed $c = \sqrt{\gamma p/\rho}$. The computational domain is $x \in [0, 1]$ and period boundary conditions are imposed at the boundaries. The computing is executed on a 128-point grid for one period of time with CFL number of 0.2. In this case, we choose $k_0 = 12$, which means most part of the energy is concentrated on high wavenumbers [11]. The numerical result of pressure distribution is shown in Fig. 2. We can find that the original WENO-IS scheme produces more excessive numerical dissipation for the high wavenumber waves although it has better numerical stability property as stated in Ref. [22]. However, with the modification of this paper, the present method achieves better resolution than WENO-Z and WENO-JS schemes, especially in the region near critical points.

4.2. Shock-tube problems

In this test case, we show the proposed regularized WENO-IS scheme passing the shock tube problems, which include the Sod problem [26], the Lax problem [27] and the 1-2-3 problem [28]. These computations are executed on a 200-point grid.

The initial condition for Sod problem is

$$(\rho, u, p) = \begin{cases} (1, 0, 1) & 0 \le x < 0.5 \\ (0.125, 0, 0.1) & 0.5 \le x < 1 \end{cases} \tag{38}$$

and the final time is $t = 2$.

The initial condition for Lax problem is

$$(\rho, u, p) = \begin{cases} (0.445, 0.698, 3.528) & 0 \le x < 0.5 \\ (0.5, 0, 0.5710) & 0.5 \le x < 1 \end{cases} \tag{39}$$

and the final time is $t = 0.14$.

The initial condition for 123 problem is

$$(\rho, u, p) = \begin{cases} (1, -2, 0.4) & 0 \le x < 0.5 \\ (1, 2, 0.4) & 0.5 \le x < 1 \end{cases} \tag{40}$$

and the final time is $t = 1$.

The comparison of the numerical results of density and velocity distribution is shown in Fig. 3. The "Exact" denotes the theoretical solution. It is obvious that the present method performs as well as other WENO schemes.
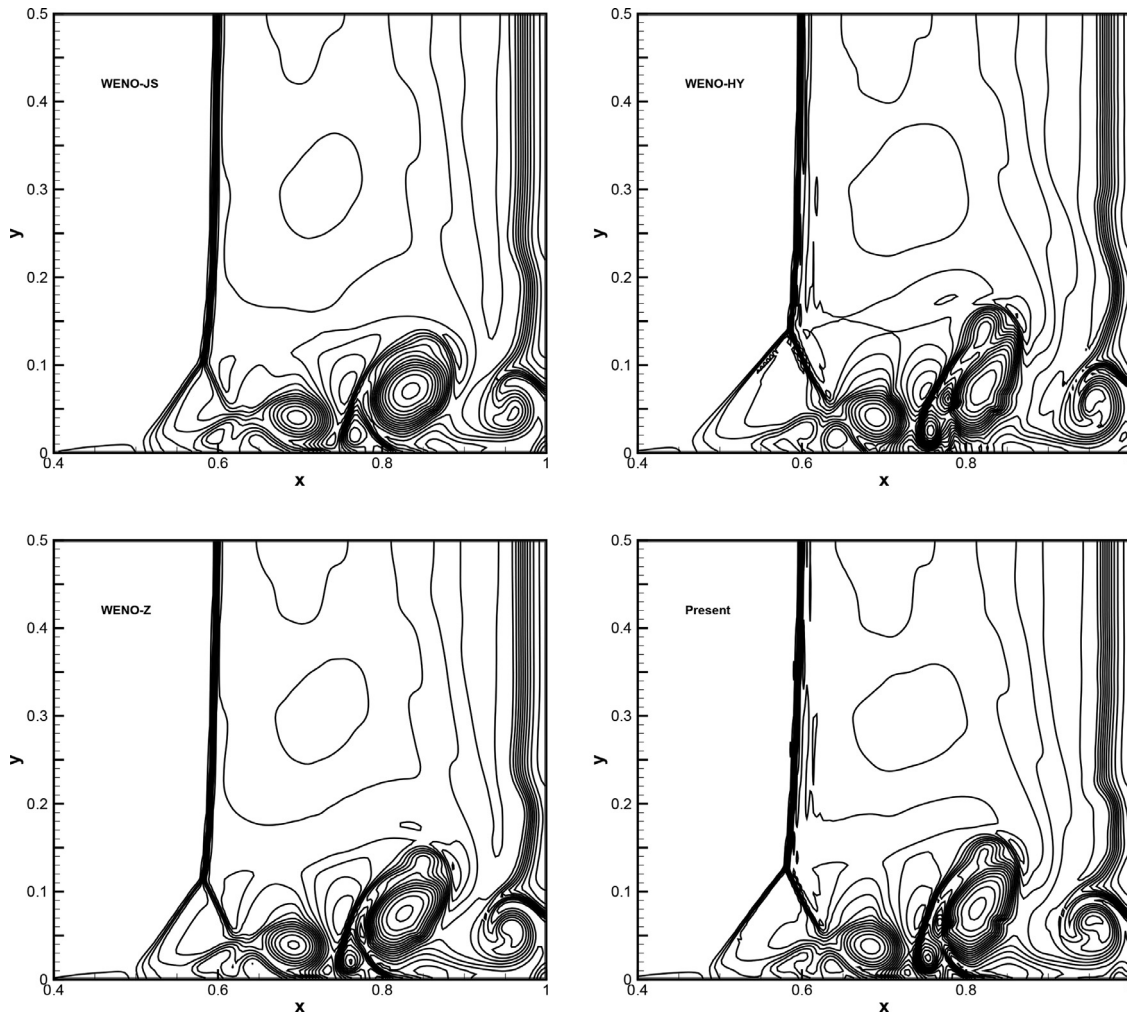
Fig. 10. Viscous shock tube problem: 20 density contours between 15 and 125. This result is solved on the 250 × 125 grid.

4.3. Sedov blast wave problem

Inspired by Refs[29,30]., the planar Sedov blast wave problem [31] is considered here to check the robustness of the present scheme. This is a severe one-dimensional problem, in which a point-blast wave propagates and a vacuum is produced during the simulation. The initial condition is

$$(\rho, u, p) = \begin{cases} (1, 0, 4 \times 10^{-13}) & 0 < x < 2 - 0.5\Delta x, 2 + 0.5\Delta x < x < 4 \\ (1, 0, 2.56 \times 10^8) & 2 - 0.5\Delta x < x < 2 + 0.5\Delta x \end{cases},$$

(41)

where $\Delta x = 5 \times 10^{-3}$ and the final time is $t = 10^{-3}$.

While WENO-Z blows up due to the severe condition caused by the sharp blast wave, the present method as well as WENO-JS and WENO-IS pass the computation and their results are shown in Fig. 4. The "Exact" denotes a result computed by WENO-JS at the high resolution of $N = 1600$. It is clearly shown that the result of present method agrees well with that at high resolution.

4.4. Interaction blast waves

A two-blast-wave interaction problem [32] is considered and the initial condition is

$$(\rho, u, p) = \begin{cases} (1, 0, 1000) & 0 \le x < 0.1 \\ (1, 0, 0.01) & 0.1 \le x < 0.9 \\ (1, 0, 100) & 0.9 \le x < 1. \end{cases}$$

(42)

The Roe flux is adopted for flux splitting and a reflection boundary condition is applied at $x = 0$ and $x = 1$. The computing is carried on up to $t = 0.038$ on a 400-point grid.

Fig. 5 gives the comparison of density profile and an enlarged part. The "Exact" denotes the convergent result which is computed by WENO-JS at the resolution of $N = 2500$. It can be observed that all methods capture the strong shock waves very well. However, the original WENO-IS scheme shows considerable larger numerical dissipation and the present method exhibits comparatively less dissipation than others, especially near the right peak of the density profile as shown in Fig. 5.

4.5. The Shu-osher problem

This case gives a Mach 3 shock wave interaction with a sine entropy wave and the initial condition is

$$(\rho, u, p) = \begin{cases} (3.857143, 2.629369, 10.3333) & x \le 1 \\ (1 + 0.2sin(5x), 0, 1) & otherwise. \end{cases}$$

(43)

The computing is carried on a 200-point grid with the domain of $x \in [0, 10]$ and the finial time is $t = 1.8$. The density profiles computed by different schemes are shown in Fig. 6. The reference "Exact" denotes a high-resolution result solved by WENO-JS on a 3200-point grid. It can be clearly noticed that all schemes can capture the shock waves well. However, in the region downstream the shock wave, the present method shows superior res-
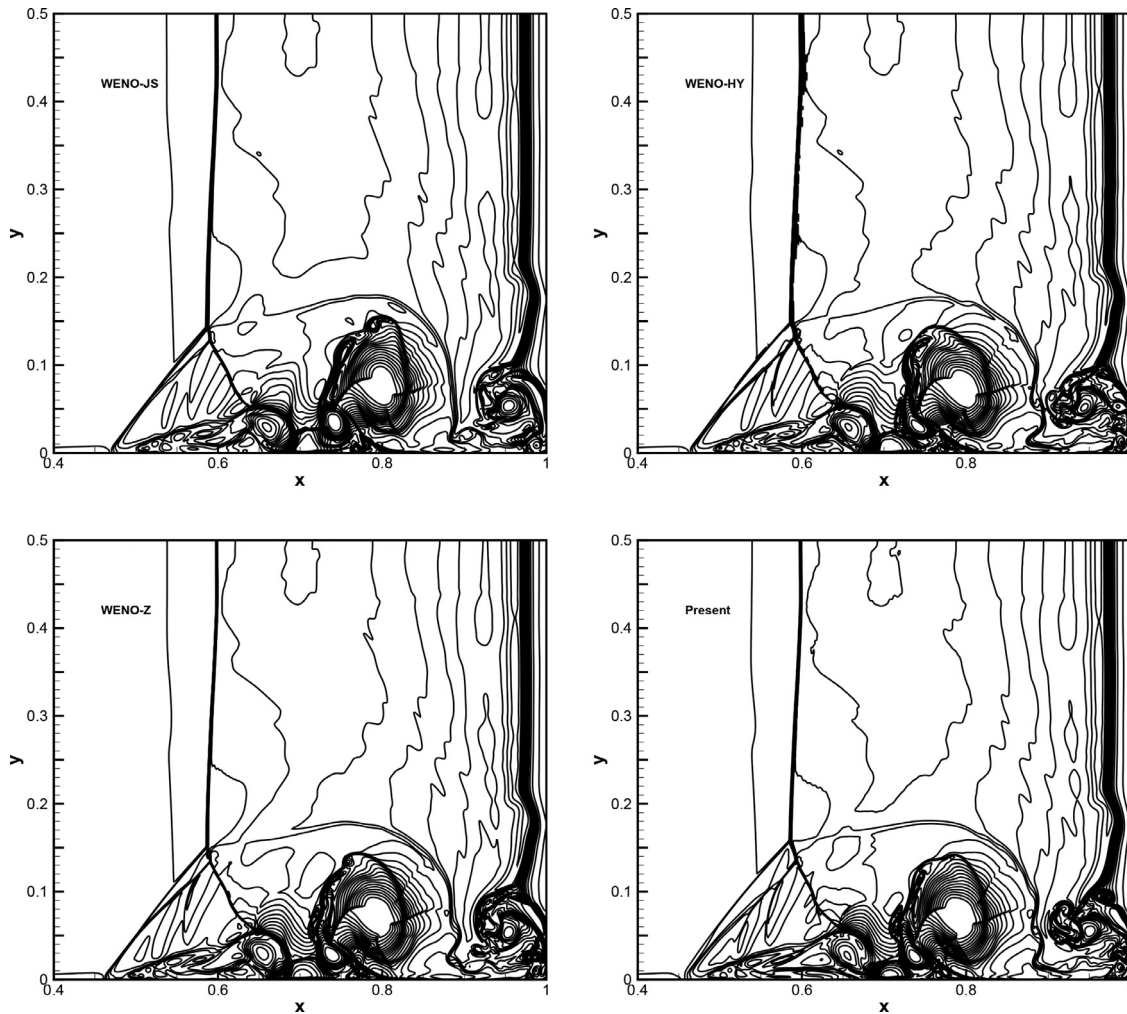
Fig. 11. Viscous shock tube problem: 20 density contours between 20 and 115. This result is solved on the 1280 × 640 grid.

olution than WENO-Z, WENO-JS and WENO-IS schemes in reproducing the fine flow structures. Also, compared with TENO5 and TENO5-opt scheme as shown in [14](their Fig. 15), the density profile of the present method is more close to the convergent density profile especially in the region downstream the shock wave.

Besides, in order to identify the improvements of the present scheme is not just the result of hybridization, we also compare with the hybrid scheme of WENO-Z and WENO-IS as shown in Fig. 7. WENOZ-HY and WENOIS-HY denote the hybrid of WENO-Z and WENO-IS with their optimal linear scheme, respectively. The hybrid method and parameters setting are the same with the present scheme. From Figs. 6 and 7, we can observe that compared with WENO-Z and WENO-IS, their hybridizations achieve a slight improvement in reproducing the fine structures. However, they are still inferior to the present scheme.

4.6. Double Mach reflection of a strong shock

This is a two-dimensional test case taken from Woodward and Colella [32] on the double Mach reflection of a strong shock. The initial condition is

$$(\rho, u, v, p) = \begin{cases} (1.4, 0, 0, 1.0) & y \leq 1.732(x - 0.1667) \\ (8.0, 7.145, -4.125, 116.8333) & otherwise, \end{cases}$$

(44)

and the computation is solved on the domain of [0, 4] × [0, 1]. This case represents a right moving shock wave with Mach 10 initially locates at $x = 0.1667$, $y = 0$ and makes an angle of 60° with x−axis. For the lower boundary, the reflection wall condition is imposed at the region $0.1667 < x < 4$, while the post shock condition is applied at $0 < x < 0.1667$. The computation is carried on two grids with solutions of 512 × 128 and 1024 × 256 and the final time is $t = 0.2$.

The density profiles on 512 × 128 and 1024 × 256 grids are shown in Fig. 8 and 9, respectively. The close-up view of the "blow up" region is presented to compare the wave resolving abilities of different schemes. It can be noticed that all methods can capture the main flow features, such as the Mach stem and the near wall jet. However, small scale structures around the slip line and the near wall jet are considerably different in their solutions. Among these schemes, the present method resolves the finest flow structures and strongest near wall jet. Although WENO-Z scheme resolves nearly the same amount of roll-up structures with the present method, it is inferior to the present method in terms of the direction and the shape of the near wall jet compared with the results with a very high resolution, e.g. Fig. 8 in Ref. [33], Fig. 2.1 in Ref. [34] and Fig. 20 in Ref. [7].

Table 1 gives the CPU time for different methods of the computing on the 512 × 128 grid. We can find that the present method is computational efficient and only costs less than three fourth of WENO-Z. Also note that the present method is a little
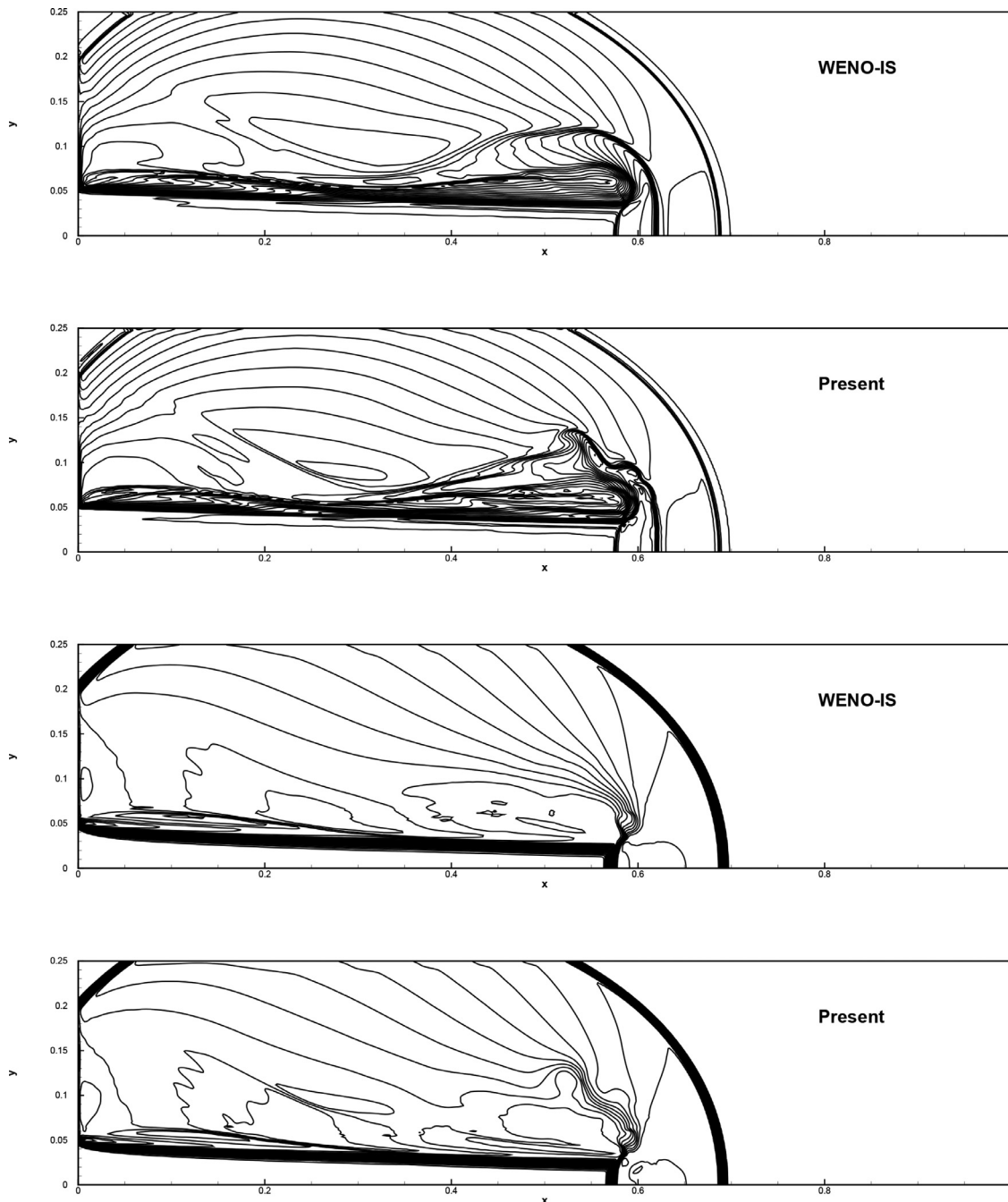
Fig. 12. Ma 2000 jet problem: 30 density contours of logarithmic scale between −4 and 4(upper); 30 pressure contours of logarithmic scale between −1 and 13(lower).

Table 1
Computational time for double Mach reflection of a strong shock on the 512 × 128 grid.

	WENO-JS	WENO-HY	WENO-Z	Present
CPU time (s)	1721	1146	1986	1446

bit time-consuming compared to WENO-HY. However, from above results and discussions, it is clear that the present method gives significant improvement results in terms of accuracy and robustness. Therefore, we believe that the slight sacrifice of efficiency of present method compared to WENO-HY is worthy, and the cost/error balance, an essential property for numerical schemes [35], of present method is better.

4.7. Two-dimensional viscous shock-tube problem

This viscous shock tube problem is taken from Ref. [36] and has been investigated in Refs. [37,38]. In this problem, the shock wave reflected from the end wall interacts with the boundary layer on the side wall induced by the incident shock. These interactions result in a complex system of vortices, shock wave bifurcation and other various flow structures. The flow filed containing various length scale structures makes it a perfect case for testing high-order schemes. The initial condition is

$$(\rho, u, v, p) = \begin{cases} (120, 0, 0, 120/\gamma) & 0 \le x < 1/2 \\ (1.2, 0, 0, 1.2/\gamma) & 1/2 \le x < 1, \end{cases} \tag{45}$$

Table 2
Computational time for viscous shock tube problem on the 250×125 grid.

	WENO-JS	WENO-HY	WENO-Z	Present
CPU time (s)	1690	1176	1740	1343

where $\gamma = 1.4$ with ideal gas used. The non-slip adiabatic condition is applied to all boundary conditions of the tube. Since the configuration is symmetric about the line $y = 0.5$, only half of the domain is solved, which is $[0, 1] \times [0, 0.5]$. Here, we set the Prandtl number $Pr = 0.73$ and the final time is 1.0. The viscosity is assumed to be constant and the Reynolds number of 200 and 1000 are considered.

The density profiles of the problem with the Reynolds number of 200 are shown in Fig. 10. The grid converged density profiles in Sjögreen and Yee [37] (their Fig. 2) and Zhou et al. [38] (their Fig. 3) obtained with much higher grid resolutions are taken as the reference for comparison. Considering the position of the triple point, the shape and the height of the primary vortex and the orientation of the long axis of the primary vortex, it is obvious that the present method gives considerable better result than other schemes. The comparison of computational time of various methods is shown in Table 2. We can see that the present method is more efficient than WENO-JS and WENO-Z scheme and only costs nearly three fourth of WENO-Z in this case.

Fig. 11 gives the density profile of the problem with the Reynolds number of 1000. The grid convergent result can be found in Ref. [38] (their Fig. 6) and Ref. [14] (their Fig. 21). With the Reynolds number increased to 1000, more fine flow structures appear in the flow field, which needs the scheme with good spectral properties to resolve them. As shown in Fig. 11, the present method performs well in terms of shock capturing and fine-structure resolution. We can see that the lambda-shape shocks captured by the present method and the WENO-Z scheme are more sharp than that of WENO-JS and WENO-HY. The big rotating structures at the lower right corner obtained by WENO-JS, WENO-HY, WENO-Z and TENO5 (see Fig. 22 in Ref. [14]) are obviously different from the reference solution. However, the one produced by the present method fits the reference well. Furthermore, the primary vortex, the adjacent small vortices as well as the jet beneath the oblique shock are predicted quite well with the present method.

4.8. Mach 2000 jet flows

In order to verify the outstanding numerical stability of the present method, the Mach 2000 jet problem, which has been computed in Zhang and Shu [16], is introduced. The computing is carried out on the domain $[0, 1] \times [0, 0.25]$ with the resolution of 640×160. The initial condition is $(\rho, u, v, p) = (0.5, 0, 0, 0.4127)$ for the entire domain. A reflective condition is applied at the bottom boundary and an outflow condition is used at the right and top boundaries. For the left boundary, an inflow condition is adopted with states $(\rho, u, v, p) = (5, 800, 0, 0.4127)$ when $y < 0.05$ and $(\rho, u, v, p) = (0.5, 0, 0, 0.4127)$ otherwise. We set $\gamma = 5/3$ and the speed of the jet is 800, which gives about Mach 2100 with respect to the sound speed in the jet gas. In the computing, the CFL number is set to 0.25 and the final time is 0.001 as in the reference [15]. Note that, without additional positive preserving method applied, the WENO-JS, WENO-HY and WENO-Z schemes all blow out during the computing. However, WENO-IS and the present method perform well. The computed density and pressure profiles of WENO-IS and the present method are shown in Fig. 12. We can observe that these results are in good agreement with those in Zhang and Shu [16] (their Fig. 4.6) and Hu et al. [15](their

Fig. 4). Furthermore, the present method shows better resolution than WENO-IS scheme and the classical WENO scheme combined with positive preserving flux limiters [15,16] with more fine flow structures resolved.

5. Conclusions

In this paper, an L2-norm regularized incremental-stencil WENO scheme is proposed for compressible flows. Following the stencil selection of WENO-IS scheme, we make the following modifications: (a) an L2-norm error term is introduced in the weighting strategy of WENO-IS scheme to cope with the discrepancy of the smoothness indicators between 2- and 3-point stencils; (b) a suitable non-dimensional regularization parameter is chosen to adaptively control the contribution of the error and regularized terms; (c) a hybridization with the optimal linear scheme is introduced to improve the performance of the scheme at smooth region and further improve computational efficiency. These modifications make the method can predict more fine flow structures by reducing numerical dissipation, and the remaining of 2-point stencils helps to compute the flow field with strong discontinuities. A set of test cases including broadband waves and discontinuities reveal that the proposed method has good wave resolving capability and keeps the superior numerical stability.

Declaration of Competing Interest

The authors declare that they have no known competing financial interests or personal relationships that could have appeared to influence the work reported in this paper.

CRediT authorship contribution statement

Yujie Zhu: Investigation, Writing - original draft. **Xiangyu Hu:** Conceptualization, Supervision.

Acknowlgedgments

References

[1] Harten A. High resolution schemes for hyperbolic conservation laws. J Comput Phys 1983;49(3):357–93.

[2] Harten A, Engquist B, Osher S, Chakravarthy SR. Uniformly high order accurate essentially non-oscillatory schemes, iii. In: Upwind and high-resolution schemes. Springer; 1987. p. 218–90.

[3] Liu X-D, Osher S, Chan T. Weighted essentially non-oscillatory schemes. J Comput Phys 1994;115(1):200–12.

[4] Jiang G-S, Shu C-W. Efficient implementation of weighted eno schemes. J Comput Phys 1996;126(1):202–28.

[5] Henrick AK, Aslam TD, Powers JM. Mapped weighted essentially non-oscillatory schemes: achieving optimal order near critical points. J Comput Phys 2005;207(2):542–67.

[6] Martín MP, Taylor EM, Wu M, Weirs VG. A bandwidth-optimized weno scheme for the effective direct numerical simulation of compressible turbulence. J Comput Phys 2006;220(1):270–89.

[7] Gerolymos G, Sénéchal D, Vallet I. Very-high-order weno schemes. J Comput Phys 2009;228(23):8481–524.

[8] Borges R, Carmona M, Costa B, Don WS. An improved weighted essentially non-oscillatory scheme for hyperbolic conservation laws. J Comput Phys 2008;227(6):3191–211.

[9] Castro M, Costa B, Don WS. High order weighted essentially non-oscillatory weno-z schemes for hyperbolic conservation laws. J Comput Phys 2011;230(5):1766–92.

[10] Taylor EM, Wu M, Martín MP. Optimization of nonlinear error for weighted essentially non-oscillatory methods in direct numerical simulations of compressible turbulence. J Comput Phys 2007;223(1):384–97.

[11] Sun Z-S, Ren Y-X, Larricq C, Zhang S-y, Yang Y-c. A class of finite difference schemes with low dispersion and controllable dissipation for dns of compressible turbulence. J Comput Phys 2011;230(12):4616–35.

[12] Hu X, Wang Q, Adams NA. An adaptive central-upwind weighted essentially non-oscillatory scheme. J Comput Phys 2010;229(23):8952–65.

[13] Hu X, Adams NA. Scale separation for implicit large eddy simulation. J Comput Phys 2011;230(19):7240–9.

[14] Fu L, Hu XY, Adams NA. A family of high-order targeted eno schemes for compressible-fluid simulations. J Comput Phys 2016;305:333–59.

[15] Hu XY, Adams NA, Shu C-W. Positivity-preserving method for high-order conservative schemes solving compressible euler equations. J Comput Phys 2013;242:169–80.

[16] Zhang X, Shu C-W. On positivity-preserving high order discontinuous galerkin schemes for compressible euler equations on rectangular meshes. J Comput Phys 2010;229(23):8918–34.

[17] Zhao G, Sun M, Xie S, Wang H. Numerical dissipation control in an adaptive wcns with a new smoothness indicator. Appl Math Comput 2018;330:239–53.

[18] Guo-yan Z, Ming-bo S. Robust and low-dissipation explicit formulation of improved adaptive wcns scheme. In: International Symposium on Shock Waves. Springer; 2017. p. 1191–9.

[19] Zhao G-y, Sun MB. Numerical dissipation control in an adaptive wcns scheme for high-speed flows. In: 21st AIAA International Space Planes and Hypersonics Technologies Conference; 2017. p. 2246.

[20] Zhao G-Y, Sun M-B, Mei Y, Li L, Wang H-B, Li G-X, et al. An efficient adaptive central-upwind weno-cu6 numerical scheme with a new sensor. J Sci Comput 2019;81(2):649–70.

[21] Li L, Wang H, Xiong D, Sun M, Tang T, Zhao G, et al. An adaptive high-resolution and low-dissipation hybrid energy consistent/wenocu scheme. MS&E 2020;790(1):012078.

[22] Wang B, Xiang G, Hu XY. An incremental-stencil weno reconstruction for simulation of compressible two-phase flows. Int J Multiphase Flow 2018;104:20–31.

[23] Nielsen MA. Neural networks and deep learning, 25. USA: Determination press; 2015.

[24] Hu X, Wang B, Adams NA. An efficient low-dissipation hybrid weighted essentially non-oscillatory scheme. J Comput Phys 2015;301:415–24.

[25] Zhao G-Y, Sun M-B, Pirozzoli S. On shock sensors for hybrid compact/weno schemes. Comput Fluid 2020;199:104439.

[26] Sod GA. A survey of several finite difference methods for systems of nonlinear hyperbolic conservation laws. J Comput Phys 1978;27(1):1–31.

[27] Lax PD. Weak solutions of nonlinear hyperbolic equations and their numerical computation. Commun Pure Appl Math 1954;7(1):159–93.

[28] Einfeldt B, Munz C-D, Roe PL, Sjögreen B. On godunov-type methods near low densities. J Comput Phys 1991;92(2):273–95.

[29] Kamiya T, Asahara M, Nonomura T. Effect of flux evaluation methods on the resolution and robustness of the two-step finite-difference weno scheme. Numer Math 2020;13(4):1068–97.

[30] Kamiya T, Asahara M, Nonomura T. Application of central differencing and low-dissipation weights in a weighted compact nonlinear scheme. Int J Numer Methods Fluids 2017;84(3):152–80.

[31] Zhang X, Shu C-W. Positivity-preserving high order finite difference weno schemes for compressible euler equations. J Comput Phys 2012;231(5):2245–58.

[32] Woodward P, Colella P. The numerical simulation of two-dimensional fluid flow with strong shocks. J Comput Phys 1984;54(1):115–73.

[33] Han L, Indinger T, Hu X, Adams NA. Wavelet-based adaptive multi-resolution solver on heterogeneous parallel architecture for computational fluid dynamics. Comput Sci-Res Develop 2011;26(3–4):197.

[34] Shi J, Zhang Y-T, Shu C-W. Resolution of high order weno schemes for complicated flow structures. J Comput Phys 2003;186(2):690–6.

[35] Zhao G, Sun M, Memmolo A, Pirozzoli S. A general framework for the evaluation of shock-capturing schemes. J Comput Phys 2019;376:924–36.

[36] Daru V, Tenaud C. Evaluation of tvd high resolution schemes for unsteady viscous shocked flows. Comput Fluid 2000;30(1):89–113.

[37] Sjögreen B, Yee HC. Grid convergence of high order methods for multiscale complex unsteady viscous compressible flows. J Comput Phys 2003;185(1):1–26.

[38] Zhou G, Xu K, Liu F. Grid-converged solution and analysis of the unsteady viscous flow in a two-dimensional shock tube. Phys Fluid 2018;30(1):016102.
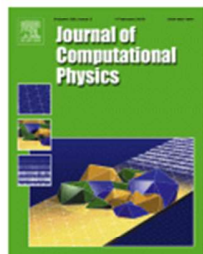
A.2 Paper II

Yujie Zhu, Xiangyu Hu

Free-stream preserving linear-upwind and WENO schemes on curvilinear grids

Contribution: My contribution to this work was the development of the method and the corresponding computer code for its implementation. I performed simulations and analyzed the results, and wrote the manuscript for the publication.

Free-stream preserving linear-upwind and WENO schemes on curvilinear grids

Author: Yujie Zhu,Xiangyu Hu

Publication: Journal of Computational Physics

Publisher: Elsevier

Date: 15 December 2019

Journal Author Rights

BACK   CLOSE WINDOW

Free-stream preserving linear-upwind and WENO schemes on curvilinear grids

Yujie Zhu, Xiangyu Hu *

Department of Mechanical Engineering, Technical University of Munich, 85748 Garching, Germany

ABSTRACT

Applying high-order finite-difference schemes, like the extensively used linear-upwind or WENO schemes, to curvilinear grids can be problematic. If the scheme doesn't satisfy the geometric conservation law, the geometrically induced error from grid Jacobian and metrics evaluation can pollute the flow field, and degrade the accuracy or cause the simulation failure even when uniform flow imposed, i.e. free-stream preserving problem. In order to address this issue, a method for general linear-upwind and WENO schemes preserving free-stream on stationary curvilinear grids is proposed. Following Lax-Friedrichs splitting, this method rewrites the numerical flux into a central term, which achieves free-stream preserving by using symmetrical conservative metric method, and a numerical dissipative term with a local difference form of conservative variables for neighboring grid-point pairs. In order to achieve free-stream preservation for the latter term, the local differences are modified to share the same Jacobian and metric terms evaluated by high order schemes. In addition, this method allows a simple hybridization switching between linear-upwind and WENO schemes is proposed for improving computational efficiency and reducing numerical dissipation. A number of testing cases including free-stream, isentropic vortex convection, double Mach reflection, flow past a cylinder and supersonic wind tunnel with a step are computed to verify the effectiveness of this method.

© 2019 Elsevier Inc. All rights reserved.

1. Introduction

In computational fluid dynamics (CFD), it is well known that finite-difference schemes are more computational efficient compared with the same order accurate finite-volume schemes [1]. Therefore, many linear, nonlinear and hybrid high-order finite-different schemes have been developed. However, despite the above-mentioned advantages, these high-order schemes are problematic when they are applied to curvilinear grids due to the lack of geometric conservation law (GCL) [2,3]. The grid Jacobian and metrics calculated in curvilinear coordinates can introduce large errors, degrade accuracy or cause numerical instability even when the flow is uniform, i.e. free-stream preserving problem. Since body-fitted curvilinear grids are widely used for computing flow problems involving practical geometries, GCL is of great importance. GCL comprises two components, i.e. the volume conservation law (VCL) relevant to moving grid and the surface conservation law (SCL) to stationary curvilinear grid. While violating VCL causes non-physical extra source or sinks, violating SCL leads to a misrepresentation of the convective velocities, which can be explained as inconsistence of vectorized computational cell surfaces in

---

* Corresponding author.
E-mail address: xiangyu.hu@tum.de (X. Hu).

a finite-volume point of view [4,3,5]. Here, we focus on free-stream preserving problem of stationary grids on which VCL is automatically satisfied and only SCL is relevant.

For low-order schemes, SCL can be achieved by simple averaging method [6], conservative form of metrics [2] or finite-volume-like technique [3]. It has also been shown that SCL can be satisfied for high-order central schemes which are characterized by non-dissipation property. In a study of central compact scheme [7] on curvilinear grid, Visbal and Gaitonde [8] found that the SCL error can be largely decreased by a two-step procedure: (a) utilizing the conservative form of metrics [2], (b) discretizing the metric terms with the same compact scheme which is used for calculating the convective-flux derivatives. In a further analysis, Deng et al. [9] identified the outer- and inner-level differential operators for the metrics, and obtained a sufficient SCL condition for general high-order central schemes [5,10]. However, as also pointed in Refs. [11,5], this condition is difficult to be satisfied for dissipative, i.e. upwind schemes due to the inconsistent outer-level differential operators used for flux splitting.

Since numerical dissipation is essential for stabilizing the solution, especially for compressible flow with shock, such difficulty is usually circumvented by the combination of finite-difference and finite-volume schemes. One typical formulation is first obtaining, usually nonlinear, dissipative convective-fluxes by finite-volume approach and then computing their derivatives by applying non-dissipative central schemes [11,5,12]. Note that this formulation is in agreement with that of the original weighted compact nonlinear scheme (WCNS) developed by Deng and Zhang [13], in which the convective-fluxes are computed with the finite-volume version of a weighted essentially non-oscillatory (WENO) scheme [14]. Another formulation is first split the upwind scheme into a non-dissipative central part and a dissipative part, and then implementing them, respectively, with high-order finite-difference and finite-volume-like schemes by freezing Jacobian and metric terms for the entire stencil [15] or by replacing the transformed conservative variables with the original ones [16,17]. Recently, a finite-difference based free-stream preserving technique was proposed by Zhu et al. [18] for WENO scheme. In this technique, the consistency of outer-level difference operators is imposed by introducing offsetting terms with the same WENO nonlinear weights for computing the corresponding inviscid fluxes. While this technique is generally effective, it may lead to large errors due to the resulting non-conservative formulation.

In this work, we propose a simple technique to impose SCL for linear-upwind and WENO schemes to achieve free-stream preserving property. The method follows a Lax-Friedrichs splitting to rewrite the numerical flux of an upwind scheme into a central term of the flux functions and a dissipative term. Since the latter term is transformed into a formulation of local differences for neighboring grid-point pairs, the Jacobian and metric terms can be evaluated with high-order schemes and applied for each of these pairs. The reminder of the paper is organized as follows. Section 2 describes the classic formulation of central schemes satisfying SCL, linear-upwind and WENO scheme on curvilinear grids based on Lax-Friedrichs splitting and their difficult on free-stream preserving. In Section 3, the local-difference formulations of the dissipative term for linear-upwind and WENO schemes are introduced with a further application of hybrid-WENO scheme following Hu et al. [19]. Validation tests and further numerical examples are presented in Section 4, and brief concluding remarks are given in the last Section 5.

2. Preliminaries

In Cartesian coordinates (t, x, y, z), the three-dimensional Euler equation is given as follows:

$$\boldsymbol{U}_t + \boldsymbol{F}_x + \boldsymbol{G}_y + \boldsymbol{H}_z = 0, \tag{1}$$

where the subscripts t, x, y, z denote temporal and spatial partial derivatives, respectively, and

$$
\begin{aligned}
\boldsymbol{U} &= \begin{pmatrix} \rho & \rho u & \rho v & \rho w & E \end{pmatrix}^T, \\
\boldsymbol{F} &= \begin{pmatrix} \rho u & \rho u^2 + p & \rho u v & \rho u w & u(E+p) \end{pmatrix}^T, \\
\boldsymbol{G} &= \begin{pmatrix} \rho v & \rho u v & \rho v^2 + p & \rho v w & v(E+p) \end{pmatrix}^T, \\
\boldsymbol{H} &= \begin{pmatrix} \rho w & \rho u w & \rho v w & \rho w^2 + p & w(E+p) \end{pmatrix}^T,
\end{aligned}
\tag{2}
$$

are conservative variables and convective fluxes, respectively. Here, ρ is density; p is pressure; u, v, w denote the velocity components in x-, y- and z-direction, respectively; and E is total energy per unit volume. In this study, the ideal gas is used and E can be expressed as

$$E = \frac{p}{\gamma - 1} + \frac{1}{2}\rho \left(u^2 + v^2 + w^2 \right). \tag{3}$$

2.1. Governing equations in curvilinear coordinates

When a curvilinear grid is used for numerical discretization, the governing equation (1) is first transformed into curvilinear coordinates (τ, ξ, η, ζ) with the following relationships

$$\tau = t, \quad \xi = \xi(x, y, z), \quad \eta = \eta(x, y, z), \quad \zeta = \zeta(x, y, z). \tag{4}$$

The transformed equation can be written as

$$\tilde{\boldsymbol{U}}_\tau + \tilde{\boldsymbol{F}}_\xi + \tilde{\boldsymbol{G}}_\eta + \tilde{\boldsymbol{H}}_\zeta = 0, \tag{5}$$

where the subscripts τ, ξ, η, ζ denote the transformed temporal and spatial partial derivatives, respectively, and

$$
\begin{aligned}
\tilde{\boldsymbol{U}} &= \frac{\boldsymbol{U}}{J}, \\
\tilde{\boldsymbol{F}} &= \frac{\xi_x}{J}\boldsymbol{F} + \frac{\xi_y}{J}\boldsymbol{G} + \frac{\xi_z}{J}\boldsymbol{H}, \\
\tilde{\boldsymbol{G}} &= \frac{\eta_x}{J}\boldsymbol{F} + \frac{\eta_y}{J}\boldsymbol{G} + \frac{\eta_z}{J}\boldsymbol{H}, \\
\tilde{\boldsymbol{H}} &= \frac{\zeta_x}{J}\boldsymbol{F} + \frac{\zeta_y}{J}\boldsymbol{G} + \frac{\zeta_z}{J}\boldsymbol{H}.
\end{aligned}
\tag{6}
$$

Here, the transformation Jacobian J and metrics are

$$
\begin{aligned}
\frac{1}{J} &= x_\xi y_\eta z_\zeta - x_\eta y_\xi z_\zeta + x_\zeta y_\xi z_\eta - x_\xi y_\zeta z_\eta + x_\eta y_\zeta z_\xi - x_\zeta y_\eta z_\xi, \\
\frac{\xi_x}{J} &= y_\eta z_\zeta - y_\zeta z_\eta, \quad \frac{\xi_y}{J} = x_\zeta z_\eta - x_\eta z_\zeta, \quad \frac{\xi_z}{J} = x_\eta y_\zeta - x_\zeta y_\eta, \\
\frac{\eta_x}{J} &= y_\zeta z_\xi - y_\xi z_\zeta, \quad \frac{\eta_y}{J} = x_\xi z_\zeta - x_\zeta z_\xi, \quad \frac{\eta_z}{J} = x_\zeta y_\xi - x_\xi y_\zeta, \\
\frac{\zeta_x}{J} &= y_\xi z_\eta - y_\eta z_\xi, \quad \frac{\zeta_y}{J} = x_\eta z_\xi - x_\xi z_\eta, \quad \frac{\zeta_z}{J} = x_\xi y_\eta - x_\eta y_\xi.
\end{aligned}
\tag{7}
$$

The equation Jacobian matrix, say $\boldsymbol{A} = \partial \tilde{\boldsymbol{F}}/\partial \tilde{\boldsymbol{U}}$, is

$$
\boldsymbol{A} = \begin{bmatrix}
0 & \xi_x & \xi_y & \xi_z & 0 \\
\xi_x\phi - u\theta & \theta - (\gamma-2)u\xi_x & u\xi_y - (\gamma-1)v\xi_x & u\xi_z - (\gamma-1)w\xi_x & (\gamma-1)\xi_x \\
\xi_y\phi - v\theta & v\xi_x - (\gamma-1)u\xi_y & \theta - (\gamma-2)v\xi_y & v\xi_z - (\gamma-1)w\xi_y & (\gamma-1)\xi_y \\
\xi_z\phi - w\theta & w\xi_x - (\gamma-1)u\xi_z & w\xi_y - (\gamma-1)v\xi_z & \theta - (\gamma-2)w\xi_z & (\gamma-1)\xi_z \\
(\phi - h)\theta & H\xi_x - (\gamma-1)u\theta & H\xi_y - (\gamma-1)v\theta & H\xi_z - (\gamma-1)w\theta & \gamma\theta
\end{bmatrix}, \tag{8}
$$

where

$$
\begin{aligned}
\theta &= \frac{\gamma-1}{2}\left(u^2 + v^2 + w^2\right), \\
\theta &= \xi_x u + \xi_y v + \xi_z w, \\
H &= \frac{\gamma p}{(\gamma-1)\rho} + \frac{1}{2}\left(u^2 + v^2 + w^2\right).
\end{aligned}
\tag{9}
$$

The eigenvalues of $\boldsymbol{A}$ are

$$
\begin{aligned}
\lambda_1 &= u\xi_x + v\xi_y + w\xi_z - a\sqrt{\xi_x^2 + \xi_y^2 + \xi_z^2}, \\
\lambda_2 = \lambda_3 = \lambda_4 &= u\xi_x + v\xi_y + w\xi_z, \\
\lambda_5 &= u\xi_x + v\xi_y + w\xi_z + a\sqrt{\xi_x^2 + \xi_y^2 + \xi_z^2},
\end{aligned}
\tag{10}
$$

where $a = \sqrt{\gamma p/\rho}$ is the speed of sound.

2.2. SCL and free-stream preserving problem

When a uniform flow is imposed, Eq. (5) can be simplified as

$$\tilde{\boldsymbol{U}}_\tau = -\left(I_x\boldsymbol{F} + I_y\boldsymbol{G} + I_z\boldsymbol{H}\right) = 0, \tag{11}$$

where

$$I_x = \left(\frac{\xi_x}{J}\right)_\xi + \left(\frac{\eta_x}{J}\right)_\eta + \left(\frac{\zeta_x}{J}\right)_\zeta = 0,$$

$$I_y = \left(\frac{\xi_y}{J}\right)_\xi + \left(\frac{\eta_y}{J}\right)_\eta + \left(\frac{\zeta_y}{J}\right)_\zeta = 0, \tag{12}$$

$$I_z = \left(\frac{\xi_z}{J}\right)_\xi + \left(\frac{\eta_z}{J}\right)_\eta + \left(\frac{\zeta_z}{J}\right)_\zeta = 0.$$

Note that, Eq. (12) may not be strictly satisfied when I_x, I_y and I_z are represented by numerical discretization. Such inconsistency can introduce artificial disturbances and lead to the free-stream preserving problem. As Eq. (12) can be explained as the consistence of vectorized computational cell surfaces in finite-volume method [3], Zhang et al. [4] proposed the surface conservation law (SCL), by which Eq. (12) is still satisfied by the numerical approximation of Jacobian, metrics and their derivative operators. It is obvious that a numerical scheme satisfying SCL has the free-stream preserving property [4,11,9].

Considering the errors of the numerically computed metrics as discussed by Deng et al. [5] and Abe et al. [20], the metric terms in Eq. (7) are rewritten as a symmetrical conservative form:

$$\frac{\xi_x}{J} = \frac{1}{2}\left[(y_\eta z)_\zeta - (y_\zeta z)_\eta + (yz_\zeta)_\eta - (yz_\eta)_\zeta\right],$$

$$\frac{\xi_y}{J} = \frac{1}{2}\left[(xz_\eta)_\zeta - (xz_\zeta)_\eta + (x_\zeta z)_\eta - (x_\eta z)_\zeta\right],$$

$$\frac{\xi_z}{J} = \frac{1}{2}\left[(x_\eta y)_\zeta - (x_\zeta y)_\eta + (xy_\zeta)_\eta - (xy_\eta)_\zeta\right],$$

$$\frac{\eta_x}{J} = \frac{1}{2}\left[(y_\zeta z)_\xi - (y_\xi z)_\zeta + (yz_\xi)_\zeta - (yz_\zeta)_\xi\right],$$

$$\frac{\eta_y}{J} = \frac{1}{2}\left[(xz_\zeta)_\xi - (xz_\xi)_\zeta + (x_\xi z)_\zeta - (x_\zeta z)_\xi\right], \tag{13}$$

$$\frac{\eta_z}{J} = \frac{1}{2}\left[(x_\zeta y)_\xi - (x_\xi y)_\zeta + (xy_\xi)_\zeta - (xy_\zeta)_\xi\right],$$

$$\frac{\zeta_x}{J} = \frac{1}{2}\left[(y_\xi z)_\eta - (y_\eta z)_\xi + (yz_\eta)_\xi - (yz_\xi)_\eta\right],$$

$$\frac{\zeta_y}{J} = \frac{1}{2}\left[(xz_\xi)_\eta - (xz_\eta)_\xi + (x_\eta z)_\xi - (x_\xi z)_\eta\right],$$

$$\frac{\zeta_z}{J} = \frac{1}{2}\left[(x_\xi y)_\eta - (x_\eta y)_\xi + (xy_\eta)_\xi - (xy_\xi)_\eta\right]$$

and

$$\frac{1}{J} = \frac{1}{3}\left[\left(x\frac{\xi_x}{J} + y\frac{\xi_y}{J} + z\frac{\xi_z}{J}\right)_\xi + \left(x\frac{\eta_x}{J} + y\frac{\eta_y}{J} + z\frac{\eta_z}{J}\right)_\eta + \left(x\frac{\zeta_x}{J} + y\frac{\zeta_y}{J} + z\frac{\zeta_z}{J}\right)_\zeta\right]. \tag{14}$$

As shown in Refs. [8,11,9], when the derivative operators within the above conservative form are kept the same with that of fluxes, Eq. (12) is satisfied and uniform flow can be preserved. Taking I_x as an example,

$$\begin{aligned}
I_x = \frac{1}{2}\big[&\delta_1{}^\xi \delta_2{}^\zeta \left(z\delta_3{}^\eta y\right) - \delta_1{}^\xi \delta_2{}^\eta \left(z\delta_3{}^\zeta y\right) + \delta_1{}^\xi \delta_2{}^\eta \left(y\delta_3{}^\zeta z\right) - \delta_1{}^\xi \delta_2{}^\zeta \left(y\delta_3{}^\eta z\right) \\
&+ \delta_1{}^\eta \delta_2{}^\xi \left(z\delta_3{}^\zeta y\right) - \delta_1{}^\eta \delta_2{}^\zeta \left(z\delta_3{}^\xi y\right) + \delta_1{}^\eta \delta_2{}^\zeta \left(y\delta_3{}^\xi z\right) - \delta_1{}^\eta \delta_2{}^\xi \left(y\delta_3{}^\zeta z\right) \\
&+ \delta_1{}^\zeta \delta_2{}^\eta \left(z\delta_3{}^\xi y\right) - \delta_1{}^\zeta \delta_2{}^\xi \left(z\delta_3{}^\eta y\right) + \delta_1{}^\zeta \delta_2{}^\xi \left(y\delta_3{}^\eta z\right) - \delta_1{}^\zeta \delta_2{}^\eta \left(y\delta_3{}^\xi z\right)\big].
\end{aligned} \tag{15}$$

Here, δ_1, δ_2 are outer derivative operators and δ_3 is inner derivative operator for calculating the corresponding level of the metric terms. The superscript ξ, η and ζ denote the operators in ξ-, η- and ζ-direction, respectively. It is straightforward to see that I_x equals to zero when $\delta_2{}^\xi = \delta_1{}^\xi$, $\delta_2{}^\eta = \delta_1{}^\eta$ and $\delta_2{}^\zeta = \delta_1{}^\zeta$. This technique is called symmetrical conservative metric method (SCMM) in Ref. [5] and is effective for central schemes. However, as will be shown in the following subsection, this method is difficult to be applied for upwind schemes.

2.3. Linear-upwind scheme

Without loss of generality, we explain the explicit 5th-order linear upwind scheme with local Lax-Friedrichs splitting.
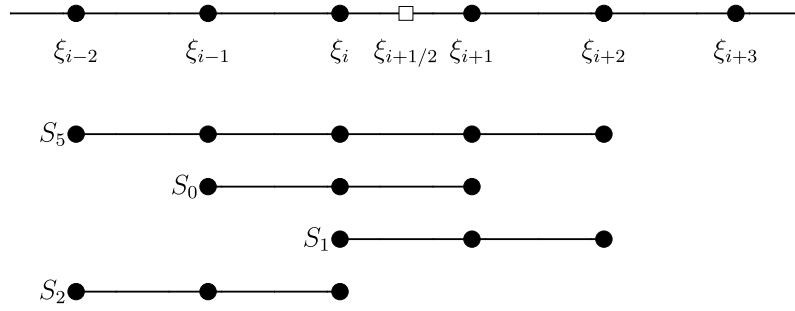
Fig. 1. Full stencil and candidate stencils for constructing the positive characteristic fluxes at the half point $\xi_{i+1/2}$. Here, the stencil S_5 is used for the 5th-order linear-upwind scheme and the stencils S_0, S_1, S_2 for WENO scheme.

The semi-discrete approximation of the governing equation (5) at a grid point indexed as (i, j, k) is as follows:

$$\left(\frac{d\tilde{U}}{d\tau}\right)_{i,j,k} = -\left(\delta_1^\xi \tilde{F}_{i,j,k} + \delta_1^\eta \tilde{G}_{i,j,k} + \delta_1^\zeta \tilde{H}_{i,j,k}\right), \tag{16}$$

where δ_1^ξ, δ_1^η and δ_1^ζ are flux derivative operators in ξ-, η- and ζ-direction, respectively. A conservative formulation of the operators, say $\delta_1^\xi \tilde{F}_{i,j,k}$, is

$$\delta_1^\xi \tilde{F}_{i,j,k} = \frac{1}{\delta\xi}\left(\tilde{F}_{i+\frac{1}{2},j,k} - \tilde{F}_{i-\frac{1}{2},j,k}\right), \tag{17}$$

where $\tilde{F}_{i\pm\frac{1}{2},j,k}$ are the numerical fluxes at half points. Here, $\delta\xi$ is the equidistant space step and is selected as follows in this work,

$$\delta\xi = \frac{L_\xi}{N_\xi}, \tag{18}$$

where L_ξ and N_ξ are the characteristic length scale and the grid number in ξ-direction, respectively. The detailed calculating procedure, say for $\tilde{F}_{i+\frac{1}{2}}$, includes the following steps. (Here, since a one-dimensional stencil is used, as shown in Fig. 1, the subscripts j and k are omitted in this section for simplicity.) First, transform the fluxes and conservative variables at all grid-points within the stencil into characteristic space and carry out a local Lax-Friedrichs splitting:

$$f_m^{s,\pm} = \frac{1}{2}L_{i+\frac{1}{2}}^s \cdot \left(\tilde{F}_m \pm \lambda^s \tilde{U}_m\right) \quad m = i-2, i+3, \tag{19}$$

where $f_m^{s,\pm}$ denote the s-th positive and negative characteristic fluxes, $L_{i+\frac{1}{2}}^s$ is the s-th left eigenvector vector of the linearized Roe-average Jacobian matrix $A_{i+1/2} = \left(\partial \tilde{F}/\partial \tilde{U}\right)_{i+1/2}$ [21] and $\lambda^s = \max\left(|\lambda_m^s|\right)$ denotes the largest s-th eigenvalue of the Jacobian A across the stencil. Then, construct the characteristic fluxes at the half point as follows:

$$\begin{aligned}
f_{i+\frac{1}{2}}^{s,+} &= \frac{1}{60}\left(2f_{i-2}^{s,+} - 13f_{i-1}^{s,+} + 47f_i^{s,+} + 27f_{i+1}^{s,+} - 3f_{i+2}^{s,+}\right), \\
f_{i+\frac{1}{2}}^{s,-} &= \frac{1}{60}\left(-3f_{i-1}^{s,-} + 27f_i^{s,-} + 47f_{i+1}^{s,-} - 13f_{i+2}^{s,-} + 2f_{i+3}^{s,-}\right).
\end{aligned} \tag{20}$$

Finally, transform the characteristic fluxes back into physical space by

$$\tilde{F}_{i+\frac{1}{2}} = \sum_s R_{i+\frac{1}{2}}^s \left(f_{i+\frac{1}{2}}^{s,+} + f_{i+\frac{1}{2}}^{s,-}\right), \tag{21}$$

where $R_{i+\frac{1}{2}}^s$ is the s-th right eigenvector vector of $A_{i+1/2}$. Substituting Eqs. (19) and (20) into Eq. (21), the numerical flux can be expressed as

$$\begin{aligned}
\tilde{F}_{i+\frac{1}{2}} &= \frac{1}{60}\left(\tilde{F}_{i-2} - 8\tilde{F}_{i-1} + 37\tilde{F}_i + 37\tilde{F}_{i+1} - 8\tilde{F}_{i+2} + \tilde{F}_{i+3}\right) \\
&\quad + \frac{1}{60}\sum_s R_{i+\frac{1}{2}}^s \lambda^s L_{i+\frac{1}{2}}^s \cdot \left(\tilde{U}_{i-2} - 5\tilde{U}_{i-1} + 10\tilde{U}_i - 10\tilde{U}_{i+1} + 5\tilde{U}_{i+2} - \tilde{U}_{i+3}\right).
\end{aligned} \tag{22}$$

Note that, the numerical flux corresponding to δ_1^ξ of Eq. (17) contains not only the central fluxes term but the numerical dissipation term which consists of conservative variables $\tilde{U}$. The central flux term can be applied with the symmetric

conservative metric method to achieve free-stream preserving by adopting 6th-order central scheme for δ_2^ξ as in Eq. (15). However, the extra term of conservative variables $\tilde{U}$ leads to that the overall δ_1^ξ is not consistent with δ_2^ξ because the numerical dissipation term doesn't vanish when a free-stream is imposed.

2.4. WENO scheme

In the typical 5th-order WENO scheme [14] with local Lax-Friedrichs flux splitting as given in Eq. (19), the positive WENO characteristic flux can be expressed as

$$f_{i+\frac{1}{2}}^{s,+} = \sum_{k=0}^{2} \omega_k^+ q_k^+, \tag{23}$$

where

$$
\begin{aligned}
q_0^+ &= \frac{1}{3} f_{i-2}^{s,+} - \frac{7}{6} f_{i-1}^{s,+} + \frac{11}{6} f_i^{s,+}, \\
q_1^+ &= -\frac{1}{6} f_{i-1}^{s,+} + \frac{5}{6} f_i^{s,+} + \frac{1}{3} f_{i+1}^{s,+}, \\
q_2^+ &= \frac{1}{3} f_i^{s,+} + \frac{5}{6} f_{i+1}^{s,+} - \frac{1}{6} f_{i+2}^{s,+},
\end{aligned}
\tag{24}
$$

are 3rd-order approximations using the stencils as shown in Fig. 1. ω_k^+ in Eq. (23) are the corresponding nonlinear weights determined by

$$\omega_k^+ = \frac{C_k^+}{\left(\varepsilon + \beta_k^+\right)^2} \Bigg/ \sum_{r=0}^{2} \frac{C_r^+}{\left(\varepsilon + \beta_r^+\right)^2}, \tag{25}$$

where

$$
\begin{aligned}
&C_0^+ = \frac{1}{10}, \quad C_1^+ = \frac{3}{5}, \quad C_2^+ = \frac{3}{10}, \\
&\beta_0^+ = \frac{1}{4}\left(f_{i-2}^{s,+} - 4f_{i-1}^{s,+} + 3f_i^{s,+}\right)^2 + \frac{13}{12}\left(f_{i-2}^{s,+} - 2f_{i-1}^{s,+} + f_i^{s,+}\right)^2, \\
&\beta_1^+ = \frac{1}{4}\left(-f_{i-1}^{s,+} + f_{i+1}^{s,+}\right)^2 + \frac{13}{12}\left(f_{i-1}^{s,+} - 2f_i^{s,+} + f_{i+1}^{s,+}\right)^2, \\
&\beta_2^+ = \frac{1}{4}\left(-3f_i^{s,+} + 4f_{i+1}^{s,+} - f_{i+2}^{s,+}\right)^2 + \frac{13}{12}\left(f_i^{s,+} - 2f_{i+1}^{s,+} + f_{i+2}^{s,+}\right)^2,
\end{aligned}
\tag{26}
$$

are the optimal weights for a background linear-upwind scheme and smoothness indicators of the corresponding stencil, respectively. $\varepsilon = 10^{-6}$ is a small positive parameter to prevent division by zero. Note that, the negative fluxes $f_{i+\frac{1}{2}}^{s,-}$ can be obtained in a similar way by flipping the stencils respect to $\xi_{i+1/2}$. Then, similar to linear-upwind schemes, the numerical fluxes at the half point in physical space are constructed by Eq. (21).

In Refs. [22,15], the WENO fluxes are divided into a central part and a dissipation part as follows:

$$
\begin{aligned}
\tilde{F}_{i+\frac{1}{2}} &= \tilde{F}_{i+\frac{1}{2}}^+ + \tilde{F}_{i+\frac{1}{2}}^- \\
&= \sum_s R_{i+\frac{1}{2}}^s f_{i+\frac{1}{2}}^{s,+} + \sum_s R_{i+\frac{1}{2}}^s f_{i+\frac{1}{2}}^{s,-} \\
&= \frac{1}{60}\left(\tilde{F}_{i-2} - 8\tilde{F}_{i-1} + 37\tilde{F}_i + 37\tilde{F}_{i+1} - 8\tilde{F}_{i+2} + \tilde{F}_{i+3}\right) \\
&\quad - \frac{1}{60}\sum_s R_{i+\frac{1}{2}}^s \left\{\left(20\omega_0^+ - 1\right)\hat{f}_{i,1}^{s,+} - \left(10\left(\omega_0^+ + \omega_1^+\right) - 5\right)\hat{f}_{i,2}^{s,+} + \hat{f}_{i,3}^{s,+}\right\} \\
&\quad + \frac{1}{60}\sum_s R_{i+\frac{1}{2}}^s \left\{\left(20\omega_0^- - 1\right)\hat{f}_{i,1}^{s,-} - \left(10\left(\omega_0^- + \omega_1^-\right) - 5\right)\hat{f}_{i,2}^{s,-} + \hat{f}_{i,3}^{s,-}\right\},
\end{aligned}
\tag{27}
$$

where

$$
\begin{aligned}
\hat{f}_{i,r+1}^{s,+} &= f_{i+r+1}^{s,+} - 3f_r^{s,+} + 3f_{i+r-1}^{s,+} - f_{i+r-2}^{s,+}, \quad r = 0, 1, 2, \\
\hat{f}_{i,r+1}^{s,-} &= f_{i-r+3}^{s,-} - 3f_{i-r+2}^{s,-} + 3f_{i-r+1}^{s,-} - f_{i-r}^{s,-}, \quad r = 0, 1, 2.
\end{aligned}
\tag{28}
$$

Similar to the linear-upwind scheme, the central flux term as in Eq. (27) of WENO scheme can also achieve free-stream preserving by using 6th-order central scheme for δ_2^ξ. However, the extra numerical dissipation term leads inconsistency between δ_2^ξ and δ_1^ξ. Another issue is that the approximation of Jacobian and metrics also introduces disturbances into the smoothness indicators of Eq. (26), so that the optimal background linear scheme is not recovered for a uniform flow either.

3. Free-stream preserving upwind schemes

From Eqs. (22) and (27), we can observe that, for the two terms in the numerical flux, since the central flux term can be applied with the symmetrical conservative metric method, free-stream preserving can be achieved by canceling the dissipative term when the flow is uniform. In previous work, this is done either by replacing the transformed conservative variables in the difference operator of the dissipative term with the original ones and simply neglecting the effect of grid Jacobian [16,17], or freezing the metric terms at the point $i + 1/2$ to construct the upwind flux [15]. In this work, we split the difference operator of the dissipative term into several local differences involving only two successive grid points and impose free-stream condition individually for each local difference.

3.1. Free-stream preserving linear-upwind scheme

The dissipation term $\tilde{\boldsymbol{F}}_{i+\frac{1}{2}}^D$ of the linear-upwind numerical flux in Eq. (22) can be rewritten into a local difference form as follows:

$$
\begin{aligned}
\tilde{\boldsymbol{F}}_{i+\frac{1}{2}}^D = \frac{1}{60} \sum_s \boldsymbol{R}_{i+\frac{1}{2}}^s \lambda^s \boldsymbol{L}_{i+\frac{1}{2}}^s \cdot \Big[\Big(\tilde{\boldsymbol{U}}_{i-2} - \tilde{\boldsymbol{U}}_{i-1} \Big) - 4 \Big(\tilde{\boldsymbol{U}}_{i-1} - \tilde{\boldsymbol{U}}_i \Big) \\
+ 6 \Big(\tilde{\boldsymbol{U}}_i - \tilde{\boldsymbol{U}}_{i+1} \Big) - 4 \Big(\tilde{\boldsymbol{U}}_{i+1} - \tilde{\boldsymbol{U}}_{i+2} \Big) + \Big(\tilde{\boldsymbol{U}}_{i+2} - \tilde{\boldsymbol{U}}_{i+3} \Big) \Big].
\end{aligned}
\tag{29}
$$

Then, we can modify Eq. (29) into a free-stream preserving formulation

$$
\begin{aligned}
\tilde{\boldsymbol{F}}_{i+\frac{1}{2}}^D = \frac{1}{60} \sum_s \boldsymbol{R}_{i+\frac{1}{2}}^s \lambda^s \boldsymbol{L}_{i+\frac{1}{2}}^s \cdot \Bigg[(\boldsymbol{U}_{i-2} - \boldsymbol{U}_{i-1}) \left(\frac{1}{J} \right)_{i-\frac{3}{2}} - 4(\boldsymbol{U}_{i-1} - \boldsymbol{U}_i) \left(\frac{1}{J} \right)_{i-\frac{1}{2}} \\
+ 6(\boldsymbol{U}_i - \boldsymbol{U}_{i+1}) \left(\frac{1}{J} \right)_{i+\frac{1}{2}} - 4(\boldsymbol{U}_{i+1} - \boldsymbol{U}_{i+2}) \left(\frac{1}{J} \right)_{i+\frac{3}{2}} + (\boldsymbol{U}_{i+2} - \boldsymbol{U}_{i+3}) \left(\frac{1}{J} \right)_{i+\frac{5}{2}} \Bigg],
\end{aligned}
\tag{30}
$$

by introducing local averaged grid Jacobian $\left(\frac{1}{J} \right)_{i-\frac{3}{2}}$, $\left(\frac{1}{J} \right)_{i-\frac{1}{2}}$, $\left(\frac{1}{J} \right)_{i+\frac{1}{2}}$, $\left(\frac{1}{J} \right)_{i+\frac{3}{2}}$ and $\left(\frac{1}{J} \right)_{i+\frac{5}{2}}$, which are evaluated by the 6th-order central scheme. Taking $\left(\frac{1}{J} \right)_{i+\frac{1}{2}}$ as an example,

$$
\left(\frac{1}{J} \right)_{i+\frac{1}{2}} = \frac{1}{60} \left[\left(\frac{1}{J} \right)_{i-2} - 8 \left(\frac{1}{J} \right)_{i-1} + 37 \left(\frac{1}{J} \right)_i + 37 \left(\frac{1}{J} \right)_{i+1} - 8 \left(\frac{1}{J} \right)_{i+2} + \left(\frac{1}{J} \right)_{i+3} \right].
\tag{31}
$$

In order to increase the numerical accuracy as far as possible, the symmetrical conservative form of the metric terms and Jacobian in Eqs. (13) and (14) are employed here. Note that, when free-stream is imposed, the modification of Eq. (30) leads to the dissipation term vanishing. In addition, this modified method recovers the original linear-upwind scheme on Cartesian grids. Also note that, this technique can be applied to general explicit linear-upwind schemes. Taking a linear-upwind scheme with 6 points stencil as an example,

$$
\tilde{\boldsymbol{F}}_{i+\frac{1}{2}} = \sum_{k=1}^3 a_k \left(\tilde{\boldsymbol{F}}_{i+k} + \tilde{\boldsymbol{F}}_{i-k+1} \right) + \sum_s \boldsymbol{R}_{i+\frac{1}{2}}^s \lambda^s \boldsymbol{L}_{i+\frac{1}{2}}^s \cdot \sum_{k=1}^3 b_k \left(\tilde{\boldsymbol{U}}_{i+k} - \tilde{\boldsymbol{U}}_{i-k+1} \right),
\tag{32}
$$

where a_k, b_k are the linear coefficients and $2(a_1 + a_2 + a_3) = 1$. The dissipative part can be rewritten as

$$
\begin{aligned}
\tilde{\boldsymbol{F}}_{i+\frac{1}{2}}^D = -\sum_s \boldsymbol{R}_{i+\frac{1}{2}}^s \lambda^s \boldsymbol{L}_{i+\frac{1}{2}}^s \cdot \Big[b_3 \Big(\tilde{\boldsymbol{U}}_{i-2} - \tilde{\boldsymbol{U}}_{i-1} \Big) + (b_2 + b_3) \Big(\tilde{\boldsymbol{U}}_{i-1} - \tilde{\boldsymbol{U}}_i \Big) \\
+ (b_1 + b_2 + b_3) \Big(\tilde{\boldsymbol{U}}_i - \tilde{\boldsymbol{U}}_{i+1} \Big) + (b_2 + b_3) \Big(\tilde{\boldsymbol{U}}_{i+1} - \tilde{\boldsymbol{U}}_{i+2} \Big) + b_3 \Big(\tilde{\boldsymbol{U}}_{i+2} - \tilde{\boldsymbol{U}}_{i+3} \Big) \Big],
\end{aligned}
\tag{33}
$$

which gives a local difference form. Then, the same treatment as Eq. (30) can be applied.

3.2. Free-stream preserving WENO scheme

Unlike the treatment of the dissipative term as in Ref. [15], we rewrite Eq. (28), say $\widehat{f}_{i,1}^{s,+}$, into a local difference form

$$
\begin{aligned}
\widehat{f}_{i,1}^{s,+} &= f_{i+1}^{s,+} - 3 f_i^{s,+} + 3 f_{i-1}^{s,+} - f_{i-2}^{s,+}, \\
&= \frac{1}{2} \boldsymbol{L}_{i+\frac{1}{2}}^s \cdot \left[\left(\tilde{\boldsymbol{F}}_{i+1} - \tilde{\boldsymbol{F}}_i \right) - 2 \left(\tilde{\boldsymbol{F}}_i - \tilde{\boldsymbol{F}}_{i-1} \right) + \left(\tilde{\boldsymbol{F}}_{i-1} - \tilde{\boldsymbol{F}}_{i-2} \right) \right] \\
&+ \frac{1}{2} \lambda^s \boldsymbol{L}_{i+\frac{1}{2}}^s \cdot \left[\left(\tilde{\boldsymbol{U}}_{i+1} - \tilde{\boldsymbol{U}}_i \right) - 2 \left(\tilde{\boldsymbol{U}}_i - \tilde{\boldsymbol{U}}_{i-1} \right) + \left(\tilde{\boldsymbol{U}}_{i-1} - \tilde{\boldsymbol{U}}_{i-2} \right) \right].
\end{aligned}
\tag{34}
$$

Then, Eq. (34) can be modified for free-stream preserving, similar to Eq. (30), as

$$
\begin{aligned}
\widehat{f}_{i,1}^{s,+} &= \frac{\boldsymbol{L}_{i+\frac{1}{2}}^s}{2} \cdot \left[(\boldsymbol{F}_{i+1} - \boldsymbol{F}_i) \left(\frac{\xi_x}{J} \right)_{i+\frac{1}{2}} - 2 (\boldsymbol{F}_i - \boldsymbol{F}_{i-1}) \left(\frac{\xi_x}{J} \right)_{i-\frac{1}{2}} + (\boldsymbol{F}_{i-1} - \boldsymbol{F}_{i-2}) \left(\frac{\xi_x}{J} \right)_{i-\frac{3}{2}} \right] \\
&+ \frac{\boldsymbol{L}_{i+\frac{1}{2}}^s}{2} \cdot \left[(\boldsymbol{G}_{i+1} - \boldsymbol{G}_i) \left(\frac{\xi_y}{J} \right)_{i+\frac{1}{2}} - 2 (\boldsymbol{G}_i - \boldsymbol{G}_{i-1}) \left(\frac{\xi_y}{J} \right)_{i-\frac{1}{2}} + (\boldsymbol{G}_{i-1} - \boldsymbol{G}_{i-2}) \left(\frac{\xi_y}{J} \right)_{i-\frac{3}{2}} \right] \\
&+ \frac{\boldsymbol{L}_{i+\frac{1}{2}}^s}{2} \cdot \left[(\boldsymbol{H}_{i+1} - \boldsymbol{H}_i) \left(\frac{\xi_z}{J} \right)_{i+\frac{1}{2}} - 2 (\boldsymbol{H}_i - \boldsymbol{H}_{i-1}) \left(\frac{\xi_z}{J} \right)_{i-\frac{1}{2}} + (\boldsymbol{H}_{i-1} - \boldsymbol{H}_{i-2}) \left(\frac{\xi_z}{J} \right)_{i-\frac{3}{2}} \right] \\
&+ \frac{\lambda^s}{2} \boldsymbol{L}_{i+\frac{1}{2}}^s \cdot \left[(\boldsymbol{U}_{i+1} - \boldsymbol{U}_i) \left(\frac{1}{J} \right)_{i+\frac{1}{2}} - 2 (\boldsymbol{U}_i - \boldsymbol{U}_{i-1}) \left(\frac{1}{J} \right)_{i-\frac{1}{2}} + (\boldsymbol{U}_{i-1} - \boldsymbol{U}_{i-2}) \left(\frac{1}{J} \right)_{i-\frac{3}{2}} \right],
\end{aligned}
\tag{35}
$$

where the half-point metrics and Jacobians, say $\left(\frac{\xi_x}{J} \right)_{i+\frac{1}{2}}$, $\left(\frac{\xi_y}{J} \right)_{i+\frac{1}{2}}$, $\left(\frac{\xi_z}{J} \right)_{i+\frac{1}{2}}$ and $\left(\frac{1}{J} \right)_{i+\frac{1}{2}}$ are all evaluated with a 6th-order central scheme as in Eq. (31).

Furthermore, in order to achieve free-stream preserving for the smooth indicators as in Eq. (26), they are rewritten into a local difference formulation too, say β_0^+ as

$$
\beta_0^+ = \frac{1}{4} \left[\left(f_{i-2}^{s,+} - f_{i-1}^{s,+} \right) - 3 \left(f_{i-1}^{s,+} - f_i^{s,+} \right) \right]^2 + \frac{13}{12} \left[\left(f_{i-2}^{s,+} - f_{i-1}^{s,+} \right) - \left(f_{i-1}^{s,+} - f_i^{s,+} \right) \right]^2.
\tag{36}
$$

Then, the same treatment as Eq. (35) can be applied. Again, since the neighboring grid-point pairs share a common Jacobian and metric value, the smoothness indicators vanish for a uniform flow. Note that this free-stream preserving method also recovers the original WENO scheme on Cartesian grids.

Furthermore, this technique can also be applied to other WENO schemes. Here, we show the detailed formulation for the WENO-CU6 scheme [23] in Appendix A.

3.3. Free-stream preserving hybrid-WENO scheme

In order to achieve less numerical dissipation and higher computational efficiency, we introduce a hybridization based on the above free-stream preserving linear-upwind and WENO schemes following the method of Hu et al. [19]. Since both the candidate schemes are free-stream preserving and recover each other for a uniform flow, it is obvious that their hybridization which switches between them has the same property. The numerical flux of the hybrid scheme in characteristic space is switched between that of the linear-upwind and WENO schemes. To achieve this, a non-dimensional discontinuity detector in the characteristic space is defined by

$$
\sigma_{i+\frac{1}{2}}^s = \left(\frac{\Delta v_{i+\frac{1}{2},s}}{\tilde{\rho}} \right)^2,
\tag{37}
$$

where

$$
\begin{aligned}
\Delta v_{i+\frac{1}{2}}^s &= \frac{1}{60} \boldsymbol{L}_{i+\frac{1}{2}}^s \cdot \left[(\boldsymbol{U}_{i-2} - \boldsymbol{U}_{i-1}) \left(\frac{1}{J} \right)_{i-\frac{3}{2}} - 4 (\boldsymbol{U}_{i-1} - \boldsymbol{U}_i) \left(\frac{1}{J} \right)_{i-\frac{1}{2}} \right. \\
&\left. + 6 (\boldsymbol{U}_i - \boldsymbol{U}_{i+1}) \left(\frac{1}{J} \right)_{i+\frac{1}{2}} - 4 (\boldsymbol{U}_{i+1} - \boldsymbol{U}_{i+2}) \left(\frac{1}{J} \right)_{i+\frac{3}{2}} + (\boldsymbol{U}_{i+2} - \boldsymbol{U}_{i+3}) \left(\frac{1}{J} \right)_{i+\frac{5}{2}} \right],
\end{aligned}
\tag{38}
$$

and $\tilde{\rho}$ is the Roe-average density of $\boldsymbol{A}_{i+\frac{1}{2}}$. A threshold is given as
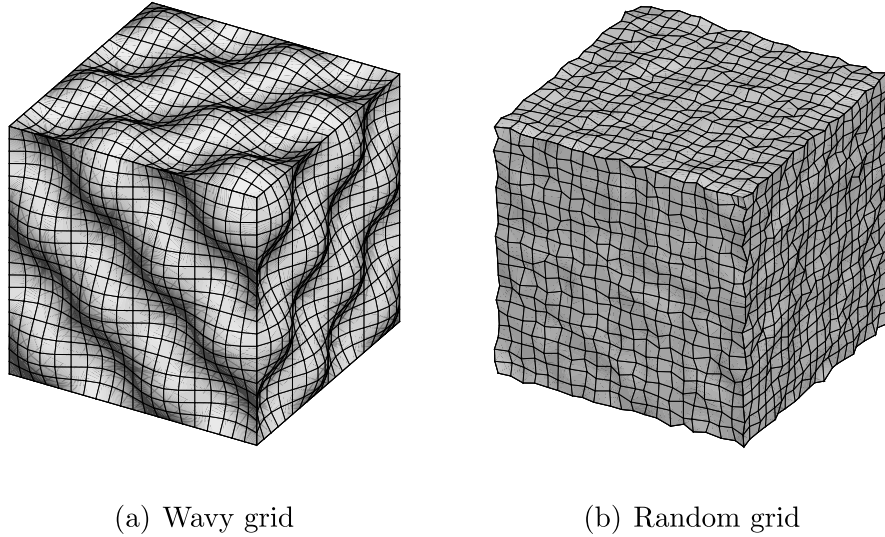
(a) Wavy grid

(b) Random grid

Fig. 2. The three-dimensional wavy and random grids for the free-stream problem.

$$\varepsilon = C \left(\frac{\Delta\xi}{L_\xi} \right)^\alpha, \tag{39}$$

where C is a positive constant, α is a positive integer. The relation between L_ξ and $\Delta\xi$ is defined in Eq. (18). When $\sigma^s_{i+\frac{1}{2}} < \varepsilon$, we believe the stencil is sufficiently smooth and the numerical flux is obtained by the linear-upwind scheme. Otherwise it is obtained by WENO scheme. As will be shown in the next section, since the linear-upwind scheme omits the calculation of non-linear weights and decreases by 5/6 the characteristic-projection operations compared with the characteristic WENO scheme, the computational cost decreases considerably due to the sparsity of discontinuities [19].

4. Numerical tests

To demonstrate the effectiveness of the proposed method, several problems including free-stream, isentropic vortex convection, double Mach reflection and flow pass a cylinder are computed on various non-uniform grids. The local Lax-Friedrichs flux splitting is used for the free-stream and vortex problems and the global Lax-Friedrichs flux splitting for the problems of double Mach, flow past cylinder and Mach 3 wind tunnel with a step. The 3rd-order TVD Runge-Kutta scheme is utilized for time integration. In the following, while "UPW5" denotes the standard 5th-order linear upwind scheme and "WENO" for the classic 5th-order WENO scheme, "UPW5-UFP", "WENO-UFP" and "WENO-HUFP" denote the linear upwind, WENO and hybrid-WENO schemes proposed in this paper, respectively, and "Exact" denotes the exact solution. For WENO-HUFP, the parameters are chosen as $C = 100$ and $\alpha = 3$.

4.1. Free-stream

The free-stream is tested on a three dimensional wavy grid and a random grid, i.e. a randomly disturbed Cartesian grid, respectively. The initial condition of an ideal gas is given as

$$u = u_\infty, \quad v = 0, \quad w = 0, \quad \rho = \rho_\infty, \quad p = p_\infty. \tag{40}$$

In this test, we set $u_\infty = 0.5$, $\rho_\infty = 1$ and $p_\infty = 1/\gamma$, where γ is the specific heat ratio. The Mach number is 0.5, the same as in Ref. [15]. The states at boundaries are set to the same as those of the initial condition. The time-step size is set to 0.1 and the results are examined after 100 time steps.

First, we test the free-stream preservation property on the wavy grid, as shown in Fig. 2(a), defined in the domain $[-2, 2] \times [-2, 2] \times [-2, 2]$ by

$$
\begin{aligned}
x_{i,j,k} &= x_{min} + \Delta x_0 \left[(i-1) + A_x sin \frac{n_{xy}\pi\,(j-1)\,\Delta y_0}{L_y} sin \frac{n_{xz}\pi\,(k-1)\,\Delta z_0}{L_z} \right], \\
y_{i,j,k} &= y_{min} + \Delta y_0 \left[(j-1) + A_y sin \frac{n_{yz}\pi\,(k-1)\,\Delta z_0}{L_z} sin \frac{n_{yx}\pi\,(i-1)\,\Delta x_0}{L_x} \right], \\
z_{i,j,k} &= z_{min} + \Delta z_0 \left[(k-1) + A_z sin \frac{n_{zx}\pi\,(i-1)\,\Delta x_0}{L_x} sin \frac{n_{zy}\pi\,(j-1)\,\Delta y_0}{L_y} \right],
\end{aligned}
\tag{41}
$$

Table 1

L_2 errors of v and w components in the free-stream problem on the wavy grid.

Method	v-component	w-component
UPW5	1.56×10^{-3}	2.48×10^{-3}
WENO	9.25×10^{-3}	1.03×10^{-2}
UPW5-UFP	6.91×10^{-16}	5.70×10^{-16}
WENO-UFP	6.99×10^{-16}	6.86×10^{-16}
WENO-HUFP	6.91×10^{-16}	5.70×10^{-16}

Table 2

L_2 errors of v and w components in the free-stream problem on the random grid.

Method	v-component	w-component
UPW5	4.91×10^{-2}	2.94×10^{-2}
WENO	1.25×10^{-1}	7.81×10^{-2}
UPW5-UFP	6.91×10^{-16}	5.31×10^{-16}
WENO-UFP	6.86×10^{-16}	6.70×10^{-16}
WENO-HUFP	6.91×10^{-16}	5.31×10^{-16}

where $L_x = L_y = L_z = 4$, $A_x = A_y = A_z = 1$, $n_{xy} = n_{xz} = n_{yz} = n_{yx} = n_{zx} = n_{zy} = 4$, and $x_{min} = -L_x/2$, $y_{min} = -L_y/2$, $z_{min} = -L_z/2$. The grid resolution is set to 21×21. The L_2 errors of the velocity components v and w of the flow field are shown in Table 1. One can find that the errors of UPW5-UFP, WENO-UFP and WENO-HUFP are all less than 10^{-15}, which is close to machine zero. However, the results obtained by UPW5 and WENO scheme exhibit much large errors. This test demonstrates that the present method is effectively free-stream preserving. Note that, the errors of WENO-HUFP are the same with that of UPW5-UFP, implying that only the linear-upwind scheme of the hybrid-WENO method is switched on throughout the entire computation.

Similar to the wavy grid, as shown in Fig. 2(b), the random grid has the same domain and grid resolution, but generated by

$$x_{i,j,k} = x_{min} + \Delta x_0 \left[(i-1) + A_x \left(2\varphi_x - 1 \right) \right],$$
$$y_{i,j,k} = y_{min} + \Delta y_0 \left[(j-1) + A_y \left(2\varphi_y - 1 \right) \right], \tag{42}$$
$$z_{i,j,k} = z_{min} + \Delta z_0 \left[(k-1) + A_z \left(2\varphi_z - 1 \right) \right],$$

where $A_x = A_y = A_z = 0.2$ are magnitudes of the random disturbances and φ_x, φ_y, φ_z are random numbers uniformly distributed between 0 and 1. The L_2 errors of velocity components v and w of the flow field are shown in Table 2. These results also prove that the present method eliminates geometrically induced errors effectively and preserves free-stream effectively.

4.2. Isentropic vortex

This two-dimensional case, taken from Ref. [15], is also computed on wavy and random grids to test the vortex preservation property. An isentropic vortex centered at $(x_c, y_c) = (0, 0)$ is superposed to a uniform flow with Mach 0.5 as the initial condition. The perturbations of the isentropic vortex are given by

$$(\delta u, \delta v) = \varepsilon \tau e^{\kappa \left(1 - \tau^2 \right)} \left(sin\theta, -cos\theta \right),$$
$$\delta T = -\frac{(\gamma - 1) \varepsilon^2}{4\kappa\gamma} e^{\kappa \left(1 - \tau^2 \right)}, \tag{43}$$
$$\delta S = 0,$$

where $\kappa = 0.204$, $\varepsilon = 0.02$, $\tau = r/r_c$ and $r = \left[(x - x_c)^2 + (y - y_c)^2 \right]^{1/2}$. Here, $r_c = 1.0$ gives the vortex core size, $T = p/\rho$ is the temperature and $S = p/\rho^\gamma$ is the entropy. The periodic boundary condition is adopted and the flow field is examined when the vortex moving back to the original location.

The first test is on a wavy grid defined in the domain $(x, y) \in [-10, 10] \times [-10, 10]$ by

$$x_{i,j} = x_{min} + \Delta x_0 \left[(i-1) + A_x sin \frac{n_{xy}\pi (j-1) \Delta y_0}{L_y} \right],$$
$$y_{i,j} = y_{min} + \Delta y_0 \left[(j-1) + A_y sin \frac{n_{yx}\pi (i-1) \Delta x_0}{L_x} \right], \tag{44}$$

where $L_x = L_y = 20$, $x_{min} = -L_x/2$, $y_{min} = -L_y/2$, $A_x \times \Delta x_0 = 0.6$, $A_y \times \Delta y_0 = 0.6$ and $n_{xy} = n_{yx} = 4$. In order to evaluate the grid convergence, 4 grids with the resolutions of $21 \times 21, 41 \times 41, 81 \times 81$ and 161×161 are used. The time-step sizes

(a) Exact   (b) UPW5   (c) WENO

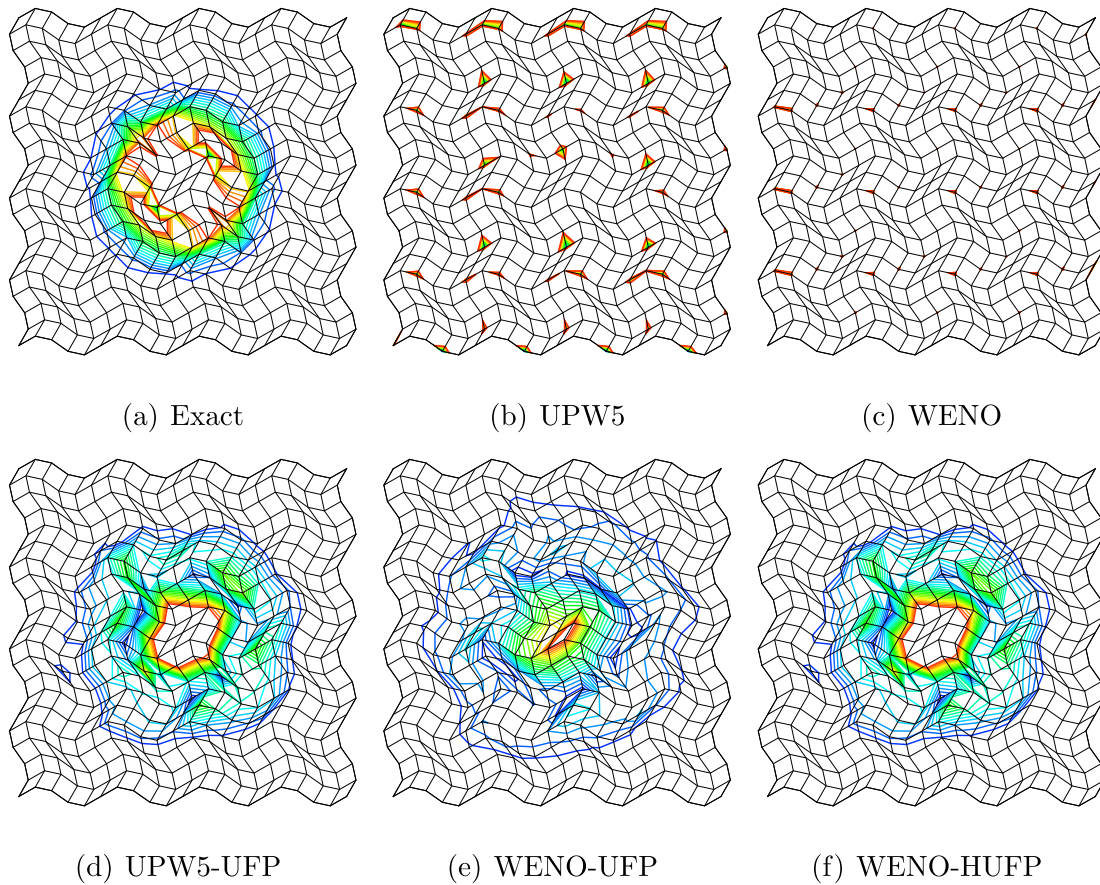(d) UPW5-UFP   (e) WENO-UFP   (f) WENO-HUFP

Fig. 3. 21 equally spaced vorticity contours from 0.0 to 0.006 of moving vortex on a two dimensional wavy grid.

Table 3

L_2, L_∞ errors of v component and their corresponding convergence rates in the vortex problem on different wavy grids.

Method	Grid number	L_2 error	Convergence rate	L_∞ error	Convergence rate
UPW5	21×21	1.20×10^{-2}	–	2.89×10^{-2}	–
	41×41	7.23×10^{-4}	4.05	3.91×10^{-3}	2.89
	81×81	2.99×10^{-5}	4.60	1.64×10^{-4}	4.58
	161×161	9.07×10^{-7}	5.04	5.50×10^{-6}	4.90
WENO	21×21	3.85×10^{-2}	–	8.94×10^{-2}	–
	41×41	2.86×10^{-3}	3.75	1.00×10^{-2}	3.16
	81×81	1.39×10^{-4}	4.36	5.60×10^{-4}	4.16
	161×161	3.16×10^{-6}	5.46	2.06×10^{-5}	4.76
UPW5-UFP	21×21	2.01×10^{-3}	–	1.45×10^{-2}	–
	41×41	3.93×10^{-4}	2.36	3.65×10^{-3}	1.99
	81×81	1.81×10^{-5}	4.44	1.53×10^{-4}	4.58
	161×161	6.13×10^{-7}	4.88	5.56×10^{-6}	4.78
WENO-UFP	21×21	2.70×10^{-3}	–	1.80×10^{-2}	–
	41×41	7.24×10^{-4}	1.90	6.57×10^{-3}	1.45
	81×81	2.19×10^{-5}	5.05	1.97×10^{-4}	5.06
	161×161	6.20×10^{-7}	5.14	5.67×10^{-6}	5.12
WENO-HUFP	21×21	2.01×10^{-3}	–	1.45×10^{-2}	–
	41×41	3.93×10^{-4}	2.36	3.65×10^{-3}	1.99
	81×81	1.81×10^{-5}	4.44	1.53×10^{-4}	4.58
	161×161	6.13×10^{-7}	4.88	5.56×10^{-6}	4.78

Δt respect to those grids are selected carefully as 0.25, 0.0625, 0.0015625 and 0.000390625, respectively, to eliminate the errors induced by time integration.

The flow field computed on the 21×21 grid is shown in Fig. 3. It can be observed that UPW5 and WENO are not able to resolve the moving vortex. The disturbances generated from the wavy grid pollute the entire flow field. However, the vortex is resolved well by both UPW5-UFP and WENO-UFP. In addition, the flow field obtained by UPW5-UFP is closer to
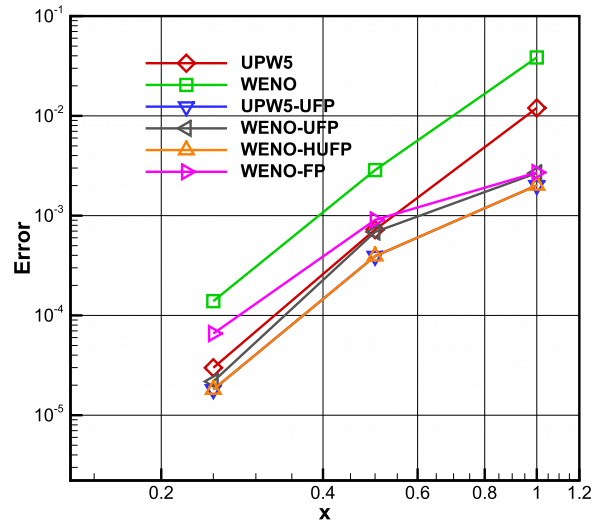
Fig. 4. L_2 errors of vortex on grids with increasing resolution.

    (a) Exact   (b) UPW5   (c) WENO

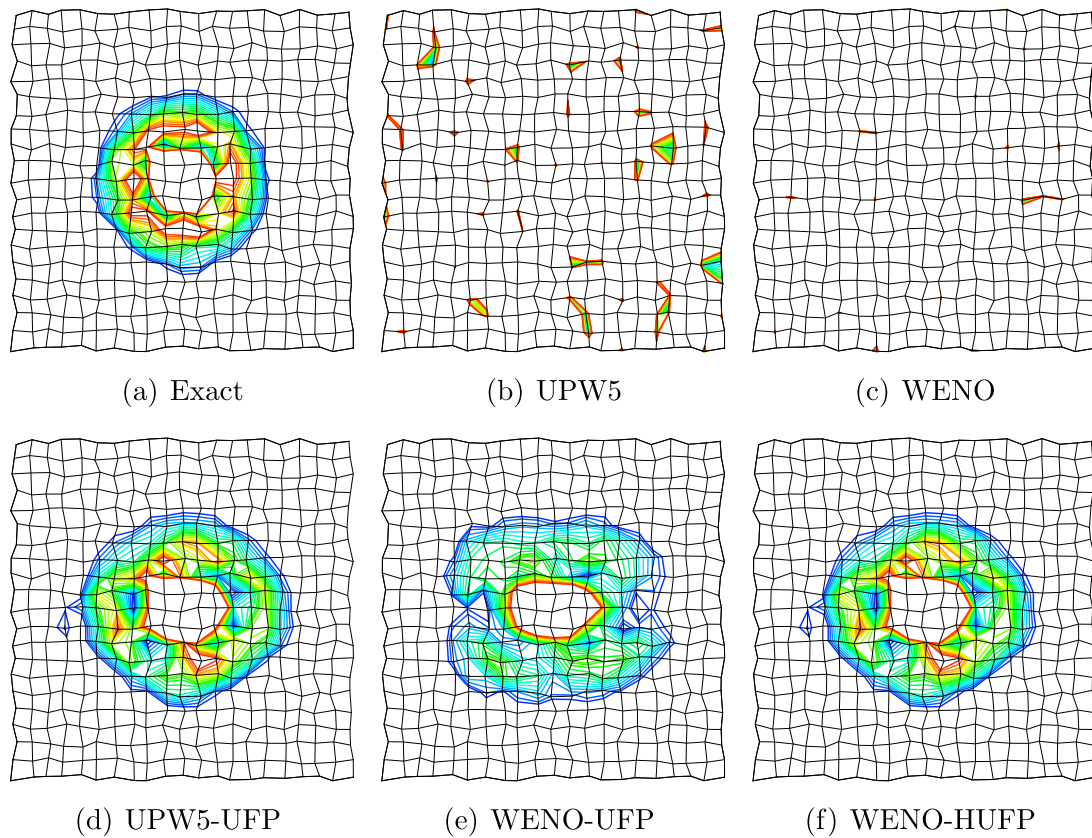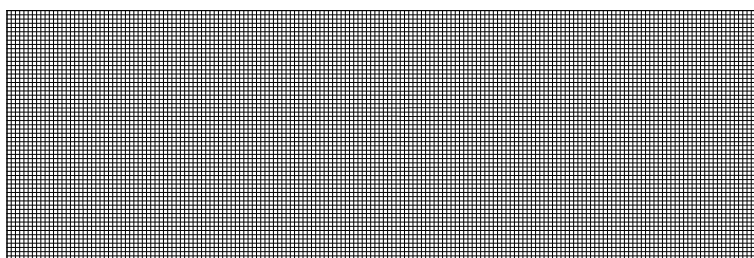   (d) UPW5-UFP   (e) WENO-UFP   (f) WENO-HUFP

Fig. 5. 21 equally spaced vorticity contours from 0.0 to 0.006 of moving vortex on a two dimensional random grid.

the exact solution than that of WENO-UFP. Again, the essentially same results obtained by UPW5 and WENO-HUFP imply that, since there is no discontinuity in the solution, only the linear-upwind scheme of the hybrid-WENO method is switched on throughout the entire computation. The L_2, L_∞ errors of the v component and their corresponding convergence rates on wavy grids at 4 resolutions are shown in Table 3. Fig. 4 gives the relation of L_2 error and the corresponding resolution in logarithmic scale. From these results, we can find that the present method works well and UPW5-UFP, WENO-UFP and WENO-HUFP produce less errors than that of WENO-FP, and achieve higher convergence rates. In addition, the convergence rate of each scheme reaches its optimal 5th-order accuracy with increasing resolution.

Then, the vortex is tested on a random grid at the resolution of 21×21 and with time-step size of $\Delta t = 0.25$. The grid points are randomized in a random direction with 20% of the original Cartesian grid size. The vorticity contours and L_2 errors of the v component are shown in Fig. 5 and Table 4, respectively. From these results, it can be observed that the flows computed by UPW5 and WENO produce much larger disturbances and the present schemes preserve the vortex well.

Table 4
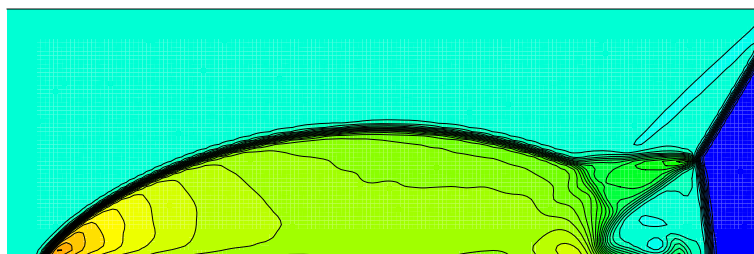L_2 errors of v component in the vortex problem on a randomized grid.

Method	Grid number	Error
UPW5	21×21	3.16×10^{-2}
WENO	21×21	4.72×10^{-2}
UPW5-UFP	21×21	1.34×10^{-3}
WENO-UFP	21×21	2.25×10^{-3}
WENO-HUFP	21×21	1.34×10^{-3}

(a) Grid
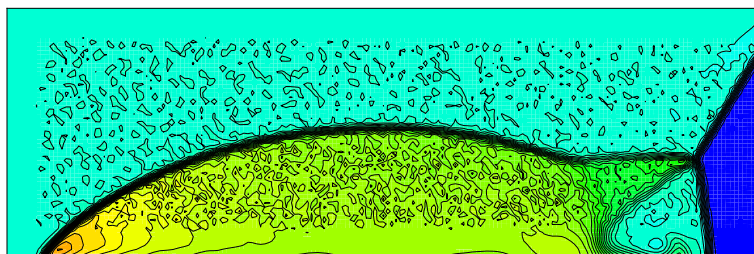
(b) WENO

(c) WENO-UFP
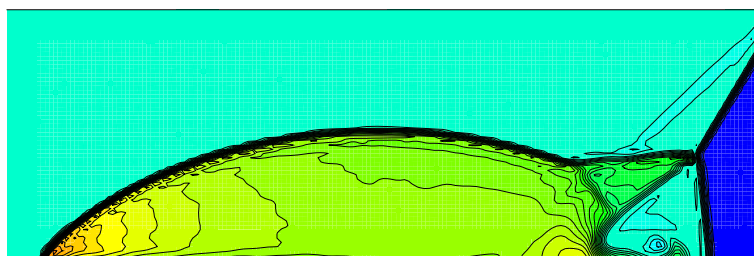
(d) WENO-HUFP

Fig. 6. 41 equally spaced density contours from 1.92 to 22.59 of double Mach reflection problem on the 240×60 grid.

It is clearly shown that the results obtained by the UPW5-UFP and WENO-HUFP are better than that of WENO-UFP due to less numerical dissipation.
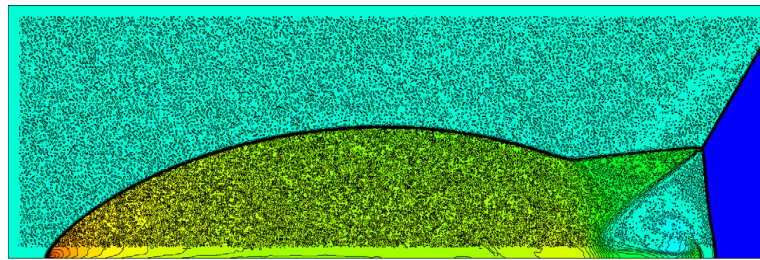
(a) WENO
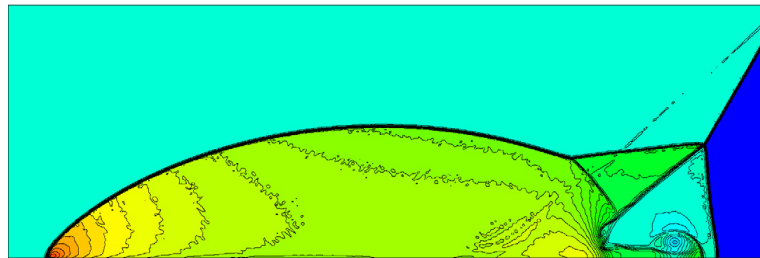
(b) WENO-Like
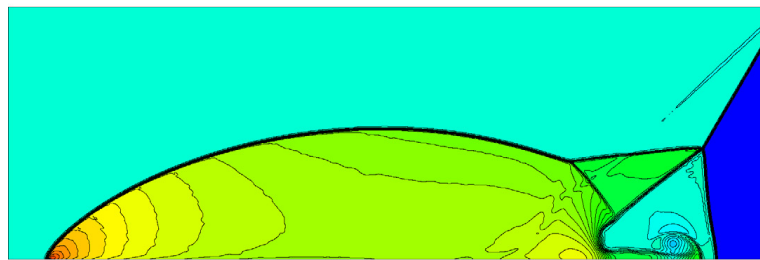
(c) WENO-UFP

(d) WENO-HUFP

Fig. 7. 41 equally spaced density contours from 1.92 to 22.59 of double Mach reflection problem on the 960×240 grid.

4.3. Double Mach reflection

The double Mach reflection problem [24] containing strong shock waves is chosen to examine the shock-capturing property of the present method. In the computational domain $(x, y) \in [0, 4] \times [0, 1]$, the initial conditions are

$$(\rho, u, v, p)^T = \begin{cases} (1.4, 0.0, 0.0, 1.0)^T & x - y \tan \frac{\pi}{6} \geq \frac{1}{6} \\ (8.0, 7.1447, -4.125, 116.5)^T & \text{else} \end{cases} . \tag{45}$$

The computation is conducted up to $t = 0.2$ with the CFL number of 0.6. Two random grids with 5% randomization at two resolutions of 240×60 and 960×240 are used. In order to preserve high accuracy near the boundary, as shown in Fig. 6(a), several points near the edges are left unperturbed. Here, the same as in Refs. [15,18], several points near the edges are left unperturbed as shown in Fig. 6(a).

Since linear schemes are not able to resolve shock wave, their results are not shown here. From the density contours of the flow field obtained on the 240×60 grid, as shown in Fig. 6, it can be observed that WENO produces large disturbances
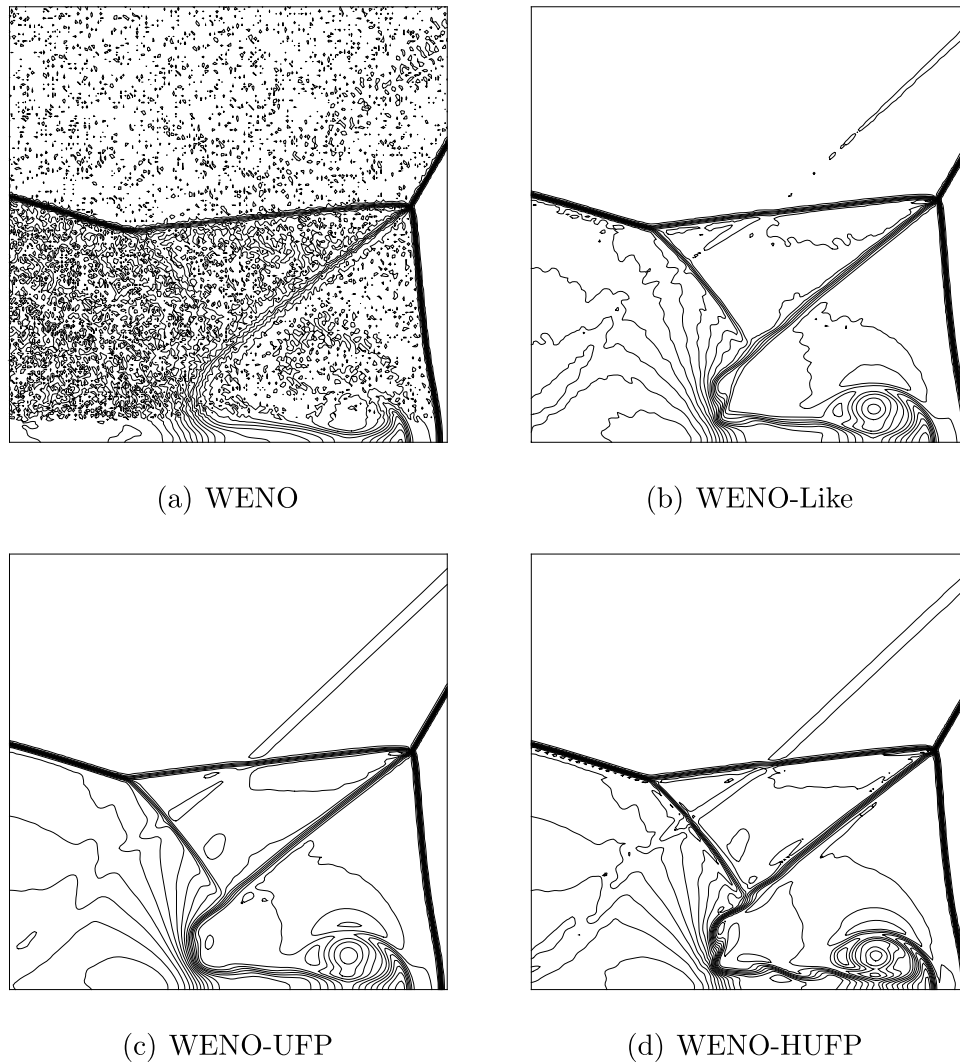
(a) WENO

(b) WENO-Like

(c) WENO-UFP

(d) WENO-HUFP

Fig. 8. The enlarge part of double Mach reflection problem on 960×240 grid.

Table 5
Computational time for double Mach reflection problem on 960×240 grid.

	WENO	WENO-Like	WENO-UFP	WENO-HUFP
CPU time (s)	1923	2951	2248	1834

in the region with grid perturbations. WENO-UFP and WENO-HUFP eliminate these disturbances and capture the shocks well and maintain the shock-capturing ability of the original WENO scheme on Cartesian grid. The density contours computed on the 960×240 grid and their enlarged part are shown in Fig. 7 and Fig. 8, respectively. Here, WENO-Like denotes the method of Zhu et al. [18]. Note that, WENO-HUFP achieves a good agreement with the result of Hu et al. [19] on a Cartesian grid at the same solution (their Fig. 6). It is able to resolve more small-scale structures and stronger wall jet, as shown in Fig. 8, than that of WENO-Like and WENO-UFP due to less numerical dissipation. Also note that, while WENO-Like resolves less flow structures than WENO-HUFP, it produces considerable more fluctuations in the reflection wave region. The computation time for different schemes is summarized in Table 5, it can be found that WENO-HUFP has the most computational efficiency and it costs less than two third of WENO-Like.

In order to check the robustness of the proposed method in the entire computational domain, different from the above chosen grids, the grids with 5% randomization at both inner and boundary points are utilized in the following test. The Jacobian and metrics at ghost cells are obtained by zero-gradient extrapolation. Fig. 9 gives the density contours obtained by WENO-HUFP scheme at two grids with resolutions of 240×60 and 960×240. Compared with the results in Fig. 6(d) and Fig. 7(d), quite good agreements are achieved except small disturbance induced from the boundary. Such small disturbances may be due to the not-exact-flat wall surface induced by the randomization.
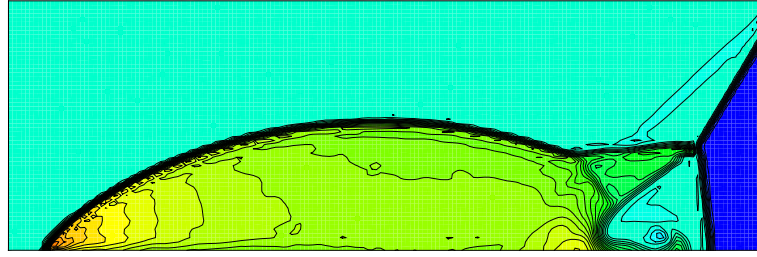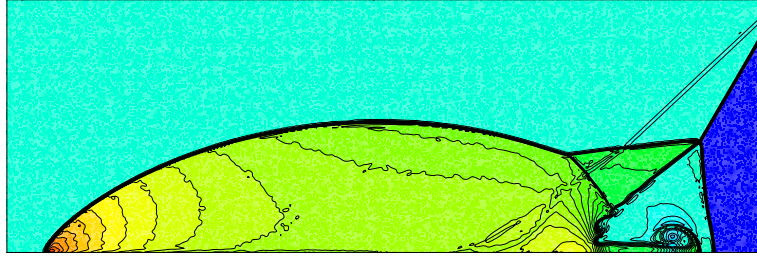
(a) 240×60

(b) 960×240

Fig. 9. 41 equally spaced density contours from 1.92 to 22.59 of double Mach reflection problem on grids with randomization at the entire computational domain.

4.4. Supersonic flow past a cylinder

A supersonic flow past a cylinder [14] is simulated on a grid randomized from a body-fitted grid. The Mach 2 supersonic flow moves toward the cylinder from left. The reflective boundary condition is applied on the cylinder surface, the supersonic inflow condition at the left boundary and the supersonic outflow condition at the other boundaries. The gird with resolution of 81×61 is generated by the curvilinear coordinates

$$
\begin{aligned}
x &= \left(R_x - (R_x - 1)\,\eta' \right) \cos \left(\theta \left(2\xi' - 1 \right) \right) \\
y &= \left(R_y - \left(R_y - 1 \right) \eta' \right) \sin \left(\theta \left(2\xi' - 1 \right) \right),
\end{aligned}
\tag{46}
$$

where

$$
\begin{aligned}
\xi' &= \frac{\xi - 1}{i_{max} - 1}, \quad \xi = i + 0.2 \cdot \varphi_i \\
\eta' &= \frac{\eta - 1}{j_{max} - 1}, \quad \eta = j + 0.2 \cdot \sqrt{1 - \varphi_i^2}.
\end{aligned}
\tag{47}
$$

Here $\theta = 5\pi/12$, $R_x = 3$, $R_y = 6$ and φ_i is a random number uniformly distributed between $[0, 1]$. The inflow pressure and density are $\rho_\infty = 1.0$ and $p_\infty = 1/\gamma$, respectively. Similar to Ref. [24], the time-step size is chosen as $\Delta t = 0.005$ and the results are examined after 5000 steps. The pressure contours and computational costs are given in Fig. 10 and Table 6, respectively. It is found that both WENO-FP and the present method eliminate the geometrically induced errors and maintain the shock capturing ability. Their results all have a good agreement with that of Jiang and Shu [14] (their Fig. 16). Note that, here, WENO-HUFP is the least dissipative and the most computational efficient.

4.5. A Mach 3 wind tunnel with a step

This case is taken from Ref. [24] and also has been investigated by Hu et al. [25]. In this case, a right-going flow with Mach 3 is passing through a wind tunnel with a facing step. The wind tunnel is 1 length unit wide and 3 length units long. The step is 0.2 length unit high and located at the bottom of the wind tunnel which is about 0.6 length unit from the left boundary. Initially, a uniform right-going Mach 3 flow is filled in the tunnel. The reflective boundary condition is applied along the walls, while inflow and outflow boundary conditions are applied at the left and right boundaries. For the singularity point at the step corner, the same modification as in Ref. [24] is adopted. We set the final time at 4.0. A random grid with 5% randomization at both inner and boundary points with the resolution of 240×80 is utilized.

The density profiles obtained by different schemes are given in Fig. 11. Here, WENO-CUFP denotes the WENO-CU6 scheme with the proposed free-stream preserving method. We can find that in results obtained by the original WENO
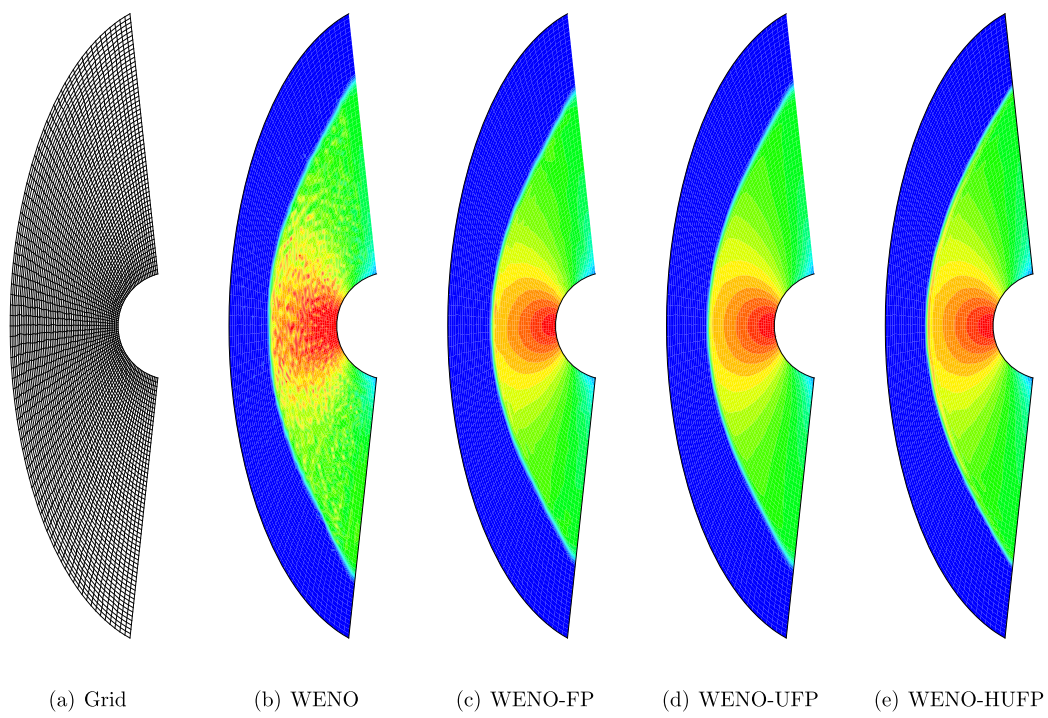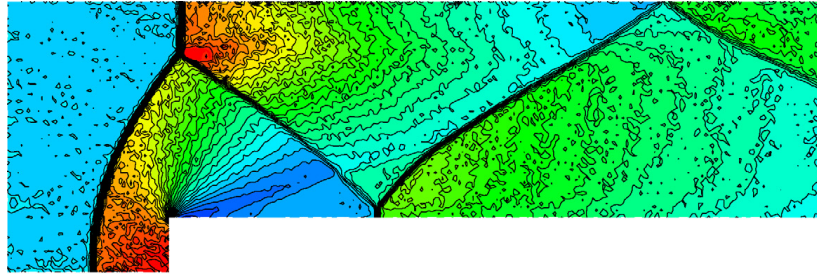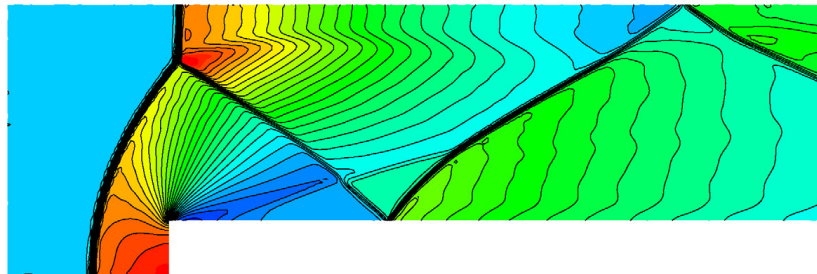
(a) Grid   (b) WENO   (c) WENO-FP   (d) WENO-UFP   (e) WENO-HUFP

Fig. 10. 21 equally spaced pressure contours from 0.86 to 3.88 of the supersonic flow past a cylinder.

Table 6
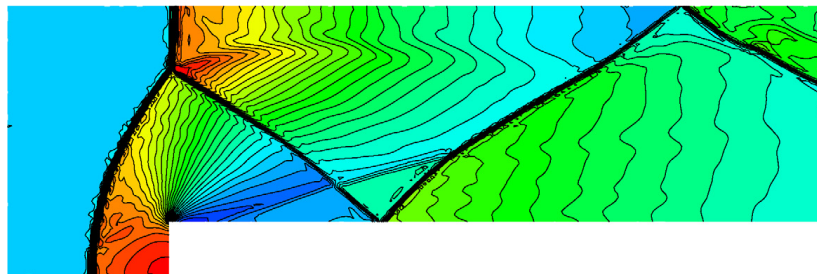Computational time for supersonic flow past a cylinder.

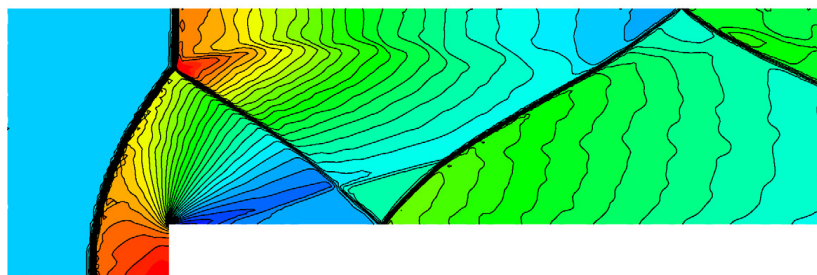|	WENO	WENO-FP	WENO-UFP	WENO-HUFP
CPU time (s)	78	109	104	62

(a) WENO

(b) WENO-UFP

(c) WENO-HUFP

(d) WENO-CUFP

Fig. 11. 30 equally spaced density contours from 0.25 to 6.00 of wind tunnel with a step problem.

scheme disturbances are scattered in the entire computational domain, and an artifact Mach steam also appears at step wall. However, with the present method, all schemes perform well for both inner and boundary points, and the results are in quite good agreement with those in Refs. [24,26].

5. Conclusions

In this paper, we propose a free-stream preserving method for general linear-upwind and WENO schemes on curvilinear grids. Following a Lax-Friedrichs flux splitting, the numerical fluxes of the upwind schemes are rewritten into a central term and a numerical dissipation term with the form of local difference using neighboring grid-point pairs. For the central term, the symmetric conservative metric method is applied straightforwardly to eliminate the geometrically induced error. For the numerical dissipation term, each neighboring grid-point pairs are modified to share a common Jacobian and metrics value which are evaluated by high order schemes. Then, a simple free-stream preserving hybridization switching between linear-upwind and WENO schemes is proposed to further improve computational efficiency and reduce numerical dissipation. A number of numerical examples demonstrate that the proposed method not only achieves good free-stream and vortex preserving properties but also maintains the shock-capturing ability of original WENO scheme. In addition, the hybrid-WENO scheme achieves less dissipative solution with considerable lower computing costs. Finally, as shown in the numerical examples, the method works well for both inner and boundary points, so we believe that this method can also be extended for problems with more complex geometries.

Declaration of competing interest

The authors declare that they have no known competing financial interests or personal relationships that could have appeared to influence the work reported in this paper.

Acknowledgements

Appendix A. Free-stream preserving WENO-CU6 scheme

The positive WENO-CU6 characteristic flux is constructed by

$$f_{i+\frac{1}{2}}^{s,+} = \sum_{k=0}^{3} \omega_k^+ q_k^+, \tag{A.1}$$

where

$$
\begin{aligned}
q_0^+ &= \frac{1}{3} f_{i-2}^{s,+} - \frac{7}{6} f_{i-1}^{s,+} + \frac{11}{6} f_i^{s,+}, \\
q_1^+ &= -\frac{1}{6} f_{i-1}^{s,+} + \frac{5}{6} f_i^{s,+} + \frac{1}{3} f_{i+1}^{s,+}, \\
q_2^+ &= \frac{1}{3} f_i^{s,+} + \frac{5}{6} f_{i+1}^{s,+} - \frac{1}{6} f_{i+2}^{s,+}, \\
q_3^+ &= \frac{11}{6} f_{i+1}^{s,+} - \frac{7}{6} f_{i+2}^{s,+} + \frac{1}{3} f_{i+3}^{s,+}.
\end{aligned}
\tag{A.2}
$$

ω_k^+ in Eq. (A.1) are the corresponding nonlinear weights determined by

$$\omega_k^+ = \frac{\alpha_k^+}{\alpha_0^+ + \alpha_1^+ + \alpha_2^+ + \alpha_3^+} \quad (k = 0, 1, 2, 3), \tag{A.3}$$

where

$$\alpha_k^+ = C_k^+ \left(C + \frac{\tau_6}{\beta_k^+ + \varepsilon} \right) \quad (k = 0, 1, 2, 3). \tag{A.4}$$

Here, $C = 20$ and $\varepsilon = 10^{-20}$. The ideal weights C_k^+, the smoothness indicators β_k^+ and τ_6 are as follows

$$
\begin{aligned}
C_0^+ &= \frac{1}{20}, \quad C_1^+ = \frac{9}{20}, \quad C_2^+ = \frac{9}{20}, \quad C_3^+ = \frac{1}{20}, \\
\beta_0^+ &= \frac{1}{4} \left(f_{i-2}^{s,+} - 4 f_{i-1}^{s,+} + 3 f_i^{s,+} \right)^2 + \frac{13}{12} \left(f_{i-2}^{s,+} - 2 f_{i-1}^{s,+} + f_i^{s,+} \right)^2, \\
\beta_1^+ &= \frac{1}{4} \left(-f_{i-1}^{s,+} + f_{i+1}^{s,+} \right)^2 + \frac{13}{12} \left(f_{i-1}^{s,+} - 2 f_i^{s,+} + f_{i+1}^{s,+} \right)^2,
\end{aligned}
$$

$$\beta_2^+ = \frac{1}{4}\left(-3f_i^{s,+} + 4f_{i+1}^{s,+} - f_{i+2}^{s,+}\right)^2 + \frac{13}{12}\left(f_i^{s,+} - 2f_{i+1}^{s,+} + f_{i+2}^{s,+}\right)^2,$$

$$
\begin{aligned}
\beta_3^+ = \beta_6^+ = \frac{1}{120960}\Big[& f_{i-2}^{s,+}\left(271779 f_{i-2}^{s,+} - 2380800 f_{i-1}^{s,+} + 4086352 f_i^{s,+}\right.\\
& - 3462252 f_{i+1}^{s,+} + 1458762 f_{i+2}^{s,+} - 245620 f_{i+3}^{s,+}\Big) + f_{i-1}^{s,+}\Big(5653317 f_{i-1}^{s,+} \\
& - 20427884 f_i^{s,+} + 17905032 f_{i+1}^{s,+} - 7727988 f_{i+2}^{s,+} + 1325006 f_{i+3}^{s,+}\Big) \\
& + f_i^{s,+}\left(19510972 f_i^{s,+} - 35817664 f_{i+1}^{s,+} + 15929912 f_{i+2}^{s,+} - 2792660 f_{i+3}^{s,+}\right) \\
& + f_{i+1}^{s,+}\left(17195652 f_{i+1}^{s,+} - 15880404 f_{i+2}^{s,+} + 2863984 f_{i+3}^{s,+}\right) \\
& + f_{i+2}^{s,+}\left(3824847 f_{i+2}^{s,+} - 1429976 f_{i+3}^{s,+}\right) + f_{i+3}^{s,+}\left(139633 f_{i+3}^{s,+}\right)\Big],
\end{aligned}
$$

$$\tau_6 = \beta_6^+ - \frac{1}{6}\left(\beta_0^+ + 4\beta_1^+ + \beta_2^+\right). \tag{A.5}$$

The negative flux can be evaluated in the similar way and the numerical flux of WENO-CU6 in physical space is constructed the same as Eq. (21). As shown in Ref. [15], the WENO-CU6 flux consists the following two parts:

$$
\begin{aligned}
\tilde{\boldsymbol{F}}_{i+\frac{1}{2}} &= \tilde{\boldsymbol{F}}_{i+\frac{1}{2}}^+ + \tilde{\boldsymbol{F}}_{i+\frac{1}{2}}^- \\
&= \sum_s \boldsymbol{R}_{i+\frac{1}{2}}^s f_{i+\frac{1}{2}}^{s,+} + \sum_s \boldsymbol{R}_{i+\frac{1}{2}}^s f_{i+\frac{1}{2}}^{s,-} \\
&= \frac{1}{60}\left(\tilde{\boldsymbol{F}}_{i-2} - 8\tilde{\boldsymbol{F}}_{i-1} + 37\tilde{\boldsymbol{F}}_i + 37\tilde{\boldsymbol{F}}_{i+1} - 8\tilde{\boldsymbol{F}}_{i+2} + \tilde{\boldsymbol{F}}_{i+3}\right) \\
&\quad - \frac{1}{60}\sum_s \boldsymbol{R}_{i+\frac{1}{2}}^s \left\{\left(20\omega_0^+ - 1\right)\widehat{f}_{i,1}^{s,+} + \left(10\left(\omega_2^+ + \omega_3^+\right) - 5\right)\widehat{f}_{i,2}^{s,+} + \left(1 - 20\omega_3^+\right)\widehat{f}_{i,3}^{s,+}\right\} \\
&\quad + \frac{1}{60}\sum_s \boldsymbol{R}_{i+\frac{1}{2}}^s \left\{\left(20\omega_0^- - 1\right)\widehat{f}_{i,1}^{s,-} + \left(10\left(\omega_2^- + \omega_3^-\right) - 5\right)\widehat{f}_{i,2}^{s,-} + \left(1 - 20\omega_3^-\right)\widehat{f}_{i,3}^{s,-}\right\},
\end{aligned}
\tag{A.6}
$$

where

$$
\begin{aligned}
\widehat{f}_{i,r+1}^{s,+} &= f_{i+r+1}^{s,+} - 3f_r^{s,+} + 3f_{i+r-1}^{s,+} - f_{i+r-2}^{s,+}, \quad r = 0, 1, 2, \\
\widehat{f}_{i,r+1}^{s,-} &= f_{i-r+3}^{s,-} - 3f_{i-r+2}^{s,-} + 3f_{i-r+1}^{s,-} - f_{i-r}^{s,-}, \quad r = 0, 1, 2.
\end{aligned}
\tag{A.7}
$$

Similar to the treatment for the original WENO flux, the conservative metric method is applied to the central part and the modification as in Eq. (35) is applied for Eq. (A.7). Numerical result in Fig. 11 verified the effectiveness of this modification.

References

[1] C.-W. Shu, High-order finite difference and finite volume WENO schemes and discontinuous Galerkin methods for CFD, Int. J. Comput. Fluid Dyn. 17 (2) (2003) 107–118.

[2] P. Thomas, C. Lombard, Geometric conservation law and its application to flow computations on moving grids, AIAA J. 17 (10) (1979) 1030–1037.

[3] M. Vinokur, An analysis of finite-difference and finite-volume formulations of conservation laws, J. Comput. Phys. 81 (1) (1989) 1–52.

[4] H. Zhang, M. Reggio, J. Trepanier, R. Camarero, Discrete form of the GCL for moving meshes and its implementation in CFD schemes, Comput. Fluids 22 (1) (1993) 9–23.

[5] X. Deng, Y. Min, M. Mao, H. Liu, G. Tu, H. Zhang, Further studies on geometric conservation law and applications to high-order finite difference schemes with stationary grids, J. Comput. Phys. 239 (2013) 90–111.

[6] T.H. Pulliam, J.L. Steger, Implicit finite-difference simulations of three-dimensional compressible flow, AIAA J. 18 (2) (1980) 159–167.

[7] S.K. Lele, Compact finite difference schemes with spectral-like resolution, J. Comput. Phys. 103 (1) (1992) 16–42.

[8] M.R. Visbal, D.V. Gaitonde, On the use of higher-order finite-difference schemes on curvilinear and deforming meshes, J. Comput. Phys. 181 (1) (2002) 155–185.

[9] X. Deng, M. Mao, G. Tu, H. Liu, H. Zhang, Geometric conservation law and applications to high-order finite difference schemes with stationary grids, J. Comput. Phys. 230 (4) (2011) 1100–1115.

[10] Y. Abe, N. Iizuka, T. Nonomura, K. Fujii, Short note: Conservative metric evaluation for high-order finite difference schemes with the GCL identities on moving and deforming grids, J. Comput. Phys. 232 (1) (2013) 14–21.

[11] T. Nonomura, N. Iizuka, K. Fujii, Freestream and vortex preservation properties of high-order WENO and WCNS on curvilinear grids, Comput. Fluids 39 (2) (2010) 197–214.

[12] Y. Jiang, C.-W. Shu, M. Zhang, An alternative formulation of finite difference weighted ENO schemes with Lax–Wendroff time discretization for conservation laws, SIAM J. Sci. Comput. 35 (2) (2013) A1137–A1160.

[13] X. Deng, H. Zhang, Developing high-order weighted compact nonlinear schemes, J. Comput. Phys. 165 (1) (2000) 22–44.

[14] G.-S. Jiang, C.-W. Shu, Efficient implementation of weighted ENO schemes, J. Comput. Phys. 126 (1) (1996) 202–228.

[15] T. Nonomura, D. Terakado, Y. Abe, K. Fujii, A new technique for freestream preservation of finite-difference WENO on curvilinear grid, Comput. Fluids 107 (2015) 242–255.

[16] M. Vinokur, H. Yee, Extension of efficient low dissipation high order schemes for 3-d curvilinear moving grids, in: Frontiers of Computational Fluid Dynamics 2002, World Scientific, 2002, pp. 129–164.

[17] Q. Li, D. Sun, P. Liu, Further study on errors in metric evaluation by linear upwind schemes with flux splitting in stationary grids, Commun. Comput. Phys. 22 (1) (2017) 64–94.

[18] Y. Zhu, Z. Sun, Y. Ren, Y. Hu, S. Zhang, A numerical strategy for freestream preservation of the high order weighted essentially non-oscillatory schemes on stationary curvilinear grids, J. Sci. Comput. 72 (3) (2017) 1021–1048.

[19] X. Hu, B. Wang, N. Adams, An efficient low-dissipation hybrid weighted essentially non-oscillatory scheme, J. Comput. Phys. 301 (2015) 415–424.

[20] Y. Abe, T. Nonomura, N. Iizuka, K. Fujii, Geometric interpretations and spatial symmetry property of metrics in the conservative form for high-order finite-difference schemes on moving and deforming grids, J. Comput. Phys. 260 (2014) 163–203.

[21] P.L. Roe, Approximate Riemann solvers, parameter vectors, and difference schemes, J. Comput. Phys. 43 (2) (1981) 357–372.

[22] G.-S. Jiang, C.-c. Wu, A high-order WENO finite difference scheme for the equations of ideal magnetohydrodynamics, J. Comput. Phys. 150 (2) (1999) 561–594.

[23] X. Hu, Q. Wang, N.A. Adams, An adaptive central-upwind weighted essentially non-oscillatory scheme, J. Comput. Phys. 229 (23) (2010) 8952–8965.

[24] P. Woodward, P. Colella, The numerical simulation of two-dimensional fluid flow with strong shocks, J. Comput. Phys. 54 (1) (1984) 115–173.

[25] C. Hu, C.-W. Shu, Weighted essentially non-oscillatory schemes on triangular meshes, J. Comput. Phys. 150 (1) (1999) 97–127.

[26] G.-S. Jiang, C.-W. Shu, Efficient implementation of weighted ENO schemes, J. Comput. Phys. 126 (1) (1996) 202–228.

A.3   Paper III

Yujie Zhu, Chi Zhang, Yongchuan Yu, Xiangyu Hu

A CAD-compatible body-fitted particle generator for arbitrarily complex geometry and its application to wave-structure interaction

Contribution: My contribution to this work was the development of the method and the corresponding computer code for its implementation. I performed simulations and analyzed the results, and wrote the manuscript for the publication.

SPRINGER NATURE LICENSE
TERMS AND CONDITIONS

Sep 21, 2021

This Agreement between Institute of Aerodynamics and Fluid Mechanics, Technical University of Munich -- Yujie Zhu ("You") and Springer Nature ("Springer Nature") consists of your license details and the terms and conditions provided by Springer Nature and Copyright Clearance Center.

License Number	5153720506254
License date	Sep 21, 2021
Licensed Content Publisher	Springer Nature
Licensed Content Publication	Journal of Hydrodynamics
Licensed Content Title	A CAD-compatible body-fitted particle generator for arbitrarily complex geometry and its application to wave-structure interaction
Licensed Content Author	Yujie Zhu et al
Licensed Content Date	Apr 28, 2021
Type of Use	Thesis/Dissertation
Requestor type	academic/university or research institute
Format	print and electronic
Portion	full article/chapter
Will you be translating?	no

Circulation/distribution 30 - 99

Author of this Springer Nature content	yes
Title	Grid and Particle Based Numerical Methods for Fluid and Solid Dynamics
Institution name	Institute of Aerodynamics and Fluid Mechanics, Technical University of Munich
Expected presentation date	Dec 2021
Requestor Location	Institute of Aerodynamics and Fluid Mechanics, Technical University of Munich Boltzmannstraße 15 Garching bei München, 85748 Germany Attn: Institute of Aerodynamics and Fluid Mechanics, Technical University of Munich
Customer VAT ID	DE170864101
Total	0.00 USD

Terms and Conditions

Springer Nature Customer Service Centre GmbH
Terms and Conditions

This agreement sets out the terms and conditions of the licence (the **Licence**) between you and **Springer Nature Customer Service Centre GmbH** (the **Licensor**). By clicking 'accept' and completing the transaction for the material (**Licensed Material**), you also confirm your acceptance of these terms and conditions.

1. Grant of License

1. 1. The Licensor grants you a personal, non-exclusive, non-transferable, world-wide licence to reproduce the Licensed Material for the purpose specified in your order only. Licences are granted for the specific use requested in the order and for no other use, subject to the conditions below.

1. 2. The Licensor warrants that it has, to the best of its knowledge, the rights to license reuse of the Licensed Material. However, you should ensure that the material you are requesting is original to the Licensor and does not carry the copyright of

another entity (as credited in the published version).

1. 3. If the credit line on any part of the material you have requested indicates that it was reprinted or adapted with permission from another source, then you should also seek permission from that source to reuse the material.

2. Scope of Licence

2. 1. You may only use the Licensed Content in the manner and to the extent permitted by these Ts&Cs and any applicable laws.

2. 2. A separate licence may be required for any additional use of the Licensed Material, e.g. where a licence has been purchased for print only use, separate permission must be obtained for electronic re-use. Similarly, a licence is only valid in the language selected and does not apply for editions in other languages unless additional translation rights have been granted separately in the licence. Any content owned by third parties are expressly excluded from the licence.

2. 3. Similarly, rights for additional components such as custom editions and derivatives require additional permission and may be subject to an additional fee. Please apply to Journalpermissions@springernature.com/bookpermissions@springernature.com for these rights.

2. 4. Where permission has been granted **free of charge** for material in print, permission may also be granted for any electronic version of that work, provided that the material is incidental to your work as a whole and that the electronic version is essentially equivalent to, or substitutes for, the print version.

2. 5. An alternative scope of licence may apply to signatories of the [STM Permissions Guidelines](#), as amended from time to time.

3. Duration of Licence

3. 1. A licence for is valid from the date of purchase ('Licence Date') at the end of the relevant period in the below table:

Scope of Licence	Duration of Licence
Post on a website	12 months
Presentations	12 months
Books and journals	Lifetime of the edition in the language purchased

4. Acknowledgement

4. 1. The Licensor's permission must be acknowledged next to the Licenced Material in print. In electronic form, this acknowledgement must be visible at the same time as the figures/tables/illustrations or abstract, and must be hyperlinked to the journal/book's homepage. Our required acknowledgement format is in the Appendix below.

5. Restrictions on use

5. 1. Use of the Licensed Material may be permitted for incidental promotional use and minor editing privileges e.g. minor adaptations of single figures, changes of format, colour and/or style where the adaptation is credited as set out in Appendix 1 below. Any other changes including but not limited to, cropping, adapting, omitting material that affect the meaning, intention or moral rights of the author are strictly prohibited.

5. 2. You must not use any Licensed Material as part of any design or trademark.

5. 3. Licensed Material may be used in Open Access Publications (OAP) before publication by Springer Nature, but any Licensed Material must be removed from OAP sites prior to final publication.

6. Ownership of Rights

6. 1. Licensed Material remains the property of either Licensor or the relevant third party and any rights not explicitly granted herein are expressly reserved.

7. Warranty

IN NO EVENT SHALL LICENSOR BE LIABLE TO YOU OR ANY OTHER PARTY OR ANY OTHER PERSON OR FOR ANY SPECIAL, CONSEQUENTIAL, INCIDENTAL OR INDIRECT DAMAGES, HOWEVER CAUSED, ARISING OUT OF OR IN CONNECTION WITH THE DOWNLOADING, VIEWING OR USE OF THE MATERIALS REGARDLESS OF THE FORM OF ACTION, WHETHER FOR BREACH OF CONTRACT, BREACH OF WARRANTY, TORT, NEGLIGENCE, INFRINGEMENT OR OTHERWISE (INCLUDING, WITHOUT LIMITATION, DAMAGES BASED ON LOSS OF PROFITS, DATA, FILES, USE, BUSINESS OPPORTUNITY OR CLAIMS OF THIRD PARTIES), AND
WHETHER OR NOT THE PARTY HAS BEEN ADVISED OF THE POSSIBILITY OF SUCH DAMAGES. THIS LIMITATION SHALL APPLY NOTWITHSTANDING ANY FAILURE OF ESSENTIAL PURPOSE OF ANY LIMITED REMEDY PROVIDED HEREIN.

8. Limitations

8. 1. _**BOOKS ONLY:**_ Where **'reuse in a dissertation/thesis'** has been selected the following terms apply: Print rights of the final author's accepted manuscript (for clarity, NOT the published version) for up to 100 copies, electronic rights for use only on a personal website or institutional repository as defined by the Sherpa guideline (www.sherpa.ac.uk/romeo/).

8. 2. For content reuse requests that qualify for permission under the STM Permissions Guidelines, which may be updated from time to time, the STM Permissions Guidelines supersede the terms and conditions contained in this licence.

9. Termination and Cancellation

9. 1. Licences will expire after the period shown in Clause 3 (above).

9. 2. Licensee reserves the right to terminate the Licence in the event that payment is not received in full or if there has been a breach of this agreement by you.

Appendix 1 — Acknowledgements:

For Journal Content:
Reprinted by permission from [**the Licensor**]: [**Journal Publisher** (e.g. Nature/Springer/Palgrave)] [**JOURNAL NAME**] [**REFERENCE CITATION** (Article name, Author(s) Name), [**COPYRIGHT**] (year of publication)

For **Advance Online Publication papers:**
Reprinted by permission from [**the Licensor**]: [**Journal Publisher** (e.g. Nature/Springer/Palgrave)] [**JOURNAL NAME**] [**REFERENCE CITATION** (Article name, Author(s) Name), [**COPYRIGHT**] (year of publication), advance online publication, day month year (doi: 10.1038/sj.[JOURNAL ACRONYM].)

For Adaptations/Translations:
Adapted/Translated by permission from [**the Licensor**]: [**Journal Publisher** (e.g. Nature/Springer/Palgrave)] [**JOURNAL NAME**] [**REFERENCE CITATION** (Article name, Author(s) Name), [**COPYRIGHT**] (year of publication)

Note: For any republication from the British Journal of Cancer, the following credit line style applies:

Reprinted/adapted/translated by permission from [**the Licensor**]: on behalf of Cancer Research UK: : [**Journal Publisher** (e.g. Nature/Springer/Palgrave)] [**JOURNAL NAME**] [**REFERENCE CITATION** (Article name, Author(s) Name), [**COPYRIGHT**] (year of publication)

For **Advance Online Publication** papers:
Reprinted by permission from The [**the Licensor**]: on behalf of Cancer Research UK: [**Journal Publisher** (e.g. Nature/Springer/Palgrave)] [**JOURNAL NAME**] [**REFERENCE CITATION** (Article name, Author(s) Name), [**COPYRIGHT**] (year of publication), advance online publication, day month year (doi: 10.1038/sj.[JOURNAL ACRONYM])

For Book content:
Reprinted/adapted by permission from [**the Licensor**]: [**Book Publisher** (e.g. Palgrave Macmillan, Springer etc) [**Book Title**] by [**Book author**(s)] [**COPYRIGHT**] (year of publication)

Other Conditions:

Version 1.3

Questions? customercare@copyright.com or +1-855-239-3415 (toll free in the US) or +1-978-646-2777.

A CAD-compatible body-fitted particle generator for arbitrarily complex geometry and its application to wave-structure interaction [*]

Yujie Zhu[1], Chi Zhang[1], Yongchuan Yu[2], Xiangyu Hu[1]
1. *Department of Mechanical Engineering, Technical University of Munich, Garching, Germany*
2. *Department of Aerospace and Geodesy, Technical University of Munich, Taufkirchen, Germany*

Abstract: Generating body-fitted particle distribution for arbitrarily complex geometry underpins the applications of particle-based method to engineering and bioengineering and is highly challenging, and thus hinders the potential of particle methods. In this paper, we present a new computer-aided design (CAD) compatible body-fitted particle generator, termed as CAD-BPG, for arbitrarily complex 3-D geometry. By parsing a CAD model, the present method can accurately tackle arbitrarily complex geometry representation and describe the corresponding geometry surface by constructing an implicit zero level-set function on Cartesian background mesh. To achieve a body-fitted and isotropic particle distribution, physics-driven relaxation process with surface bounding governed by the transport-velocity formulation of smoothed particle hydrodynamics (SPH) methodology is conducted to characterize the particle evolution. A set of examples, ranging from propeller, stent structures and anatomical heart models, show simplicity, accuracy and versatility of the present CAD-BPG for generating body-fitted particle distribution of arbitrarily complex 3-D geometry. Last but not least, the present CAD-BPG is applied for modeling wave-structure interaction, where wave interaction with an oscillating wave surge converter is studied, and the results show that the present method not only provides an efficient and easy-to-implement pre-processing tool for particle-based simulation but also improves the numerical accuracy compared with lattice particle distribution. Consequently, the propose CAD-BPG sheds light on simulating real-world applications by particle-based methods for researchers and engineers.

Key words: CAD-compatible, body-fitted, particle distribution, level-set

Introduction

Fully Lagrangian mesh free particle-based methods, in particular smoothed particle hydrodynamics (SPH)[1-2], moving-particle semi-implicit method (MPS)[3] and discrete element method (DEM)[4], have attracted increasing attention in a broad range of fields including fluid dynamics[5-9], solid mechanics[10-13] and fluid structure interactions[14-16]. In the past decades, particle-based methods have been applied in industrial applications where complex 3-D geometry are involved, viz, bird strike[17], high-pressure water jets impacting pelton turbine blades[18], oil flow inside a gearbox[19], wave-structure interactions[20-21] and stent and myocardium deformation in biomechanics[22-23]. These industrial and biomechanical applications pose a challenge of generating high-quality body-fitted particle distribution for arbitrarily complex 3-D geo-metry.

In particle-based methods, initial particle distri-bution is commonly generated by two approaches: (1) direct initiate particles on a lattice structure, (2) generate particles on a volume element mesh. The former approach, where particles are positioned on a cubic lattice structure, is widely used in particle-based methods community. For example, Dominguez et al.[24] proposed a pre-processing tool for their DualSPHysics library, where particles are generated on lattice structure and 3-D object is represented by particle model with excluding the outside particles. This approach has the advantage that particles are equalized, therefore, the induced particles distribution is isotropic. However, portraying the correct surface in particular for complex geometry requires a very fine spatial resolution. The second approach, where particles are generated at the center of tetra- or hexahedron volume elements and its volume is equal to the corresponding element volume, is widely used in the application of bird strike[25-26] and provided by state-of-art commercial pre-processing tools. The approach can accurately portray the complex surface, however, comprises drawbacks of non-uniform

---

[*] **Biography:** Yujie Zhu (1992-), Male, Ph. D. Candidate,
E-mail: yujie.zhu@tum.de
Corresponding author: Chi Zhang, Xiangyu Hu,
E-mail: c.zhang@tum.de, xiangyu.hu@tum.de

particle spacing and volume which reduce the interpolation accuracy. Recently, the weighted Voronoi tessellation (WVT) method has been applied for generating initial particle distribution by Diehl et al.[27] for SPH astrophysical simulation and by Siemann and Ritt[17] for SPH modeling of bird-strike. Also, Vela et al.[28] proposed an algorithm for constructing complex initial density distributions with low noise. More recently, Fu and Ji[29] applied centroidal Voronoi particle method by combining the centroidal Voronoi tessellation and Voronoi particle dynamics for generating isotropic particle distribution for two-dimensional simple geometry. These methods are easy to implement and typically generate optimal particle configuration with very good interpolation properties, however, they need ghost particle to impose proper boundary conditions which hinders the ability of handling complex geometry where ghost particle construction is not an easy task. Notwithstanding the aforementioned efforts, generating isotropic particle distribution for arbitrarily complex 3-D geometry is still in its infancy.

In this paper, we propose a computer-aided design (CAD) compatible body-fitted particle generator, named CAD-BPG thereafter, to generate body-fitted and homogeneous particle distribution for 3-D arbitrarily complex geometry. The key idea is to parse a CAD geometry representation and then conduct particle relaxation with surface bounding governed by the transport-velocity formulation in SPH methodology. More precisely, the CAD-BPG represents an arbitrarily complex geometry by parsing a CAD model, and describes the corresponding geometry surface by constructing an implicit zero level-set function. Starting from a preconditioned lattice particle distribution generated inside the domain of the geometry, a physics-driven relaxation process is introduced to relax particle distributions by applying the transport-velocity formulation[30, 13]. Instead of applying ghost particle as in Ref. [29], we introduce a simple surface bounding method to constrain surface particles to achieve body-fitted particle distribution. Compared with Refs. [24, 29, 27], the present CAD-BPG can achieve body-fitted particle distribution for arbitrarily complex 3-D geometry. The particle distributions for structures, e.g., propeller, stents and anatomical heart model, are generated to demonstrate the simplicity, accuracy and versatility of the proposed CAD-BPG for arbitrarily complex 3-D geometry. Then, the CAD-BPG is applied for modeling wave-structure interaction, where regular wave interacting with an oscillating wave surge converter (OWSC) is considered, and the results show that the present method not only provides an efficient and easy-to-implement pre-processing tool for particle-based simulation but also improves the numerical accuracy compared with lattice particle distribution. Having the validation and implementation, it is not hard to conclude that the CAD-BPG sheds light on particle-based simulation for real-world industrial and engineering applications.

The code of the present particle generator and geometries adopted in this work are available in our open-source SPHinXsys library[31] on GitHub at https://github.com/Xiangyu-Hu/SPHinXsys.

1. Geometry definition and level-set method

In this section, we first briefly present the surface presentation and its parsing of arbitrary complex 3-D geometry. Subsequently, this surface presentation is exploited for constructing a signed-distance level-set function which is applied for surface particle bounding in the physical relaxation process.

1.1 Surface representation

To represent the surface of an arbitrary complex 3-D geometry, one very flexible method is the triangulation of the surface. The surface can be approximated to an arbitrary accuracy by adjusting the spatial resolution of the triangles applied. As a well explored topic, the generation of such triangulations has widely applied in CAD modeling, computer graphics and recently as representation of 3D printing geometries. There are many different file formats, e.g. STL, OBJ and VTK, to save such a triangulation and herein we choose STL file format for the surface representation.

For reading and parsing the STL file, we apply a parser provided by Simbody, an open-source library for multi-body dynamics[32] and is coupled with our SPHinXsys library for soling fluid-multi-body interaction problems[20]. More importantly, Simbody also provides several built-in functions, for example finding the distance from a given point to the surface and determining whether a given point is located inside a geometry surface, and these functions play key role in constructing level-set function. Note that one can build its own CAD-model parser or apply a proper open-source library.

1.2 Level-set method

Following the level-set method[33], the geometry surface can be represented by the zero level-set of the signed-distance function

$$\Gamma = \{(x,y,z) \,|\, \phi(x,y,z,t) = 0\} \tag{1}$$

Then, the normal direction $N = (n_x, n_y, n_z)^{\mathrm{T}}$ of the surface can be computed from

$$N = \frac{\nabla \phi}{|\nabla \phi|} \tag{2}$$

In present work, a Cartesian background mesh is generated in the whole computational domain to discretize the level-set function. For each mesh cell, the level-set value ϕ is equal to the distance from the cell center to the geometry surface. Also, the negative phase with $\phi < 0$ is defined if the cell center is inside the geometry and positive phase with $\phi > 0$ other- wise. Here, computing the distance from a given point i.e., the cell center, to the corresponding surface and checking whether a point is inside the geometry are conducted by calling built-in functions in Simbody library. Notwithstanding, the distance can be com- puted by iterating all triangles to find the nearest triangle and then find the closest point located on the triangle. Also, the checking procedure can be conducted by checking the sign of the dot product between the nearest triangle's norm and the vector pointing from the closest point located on the triangle to the given point.

2. Model equations and numerical algorithm

In this section, we briefly summarize the model equations for physics-driven relaxation and their corresponding SPH discretization. Then, the particle initial condition and evolution strategies are also presented.

2.1 Governing equations and physics-driven relaxation

In present work, the physics-driven relaxation is governed by the conservation of momentum

$$\frac{\mathrm{d}\boldsymbol{v}}{\mathrm{d}t} = \boldsymbol{F}_p \tag{3}$$

where $\boldsymbol{v}$ is the advection velocity, $\boldsymbol{F}_p$ denotes the accelerations due to the repulsive pressure force. Also, $\mathrm{d}(\cdot)/\mathrm{d}t = \partial(\cdot)/\partial t + \boldsymbol{v} \cdot \nabla(\cdot)$ stands for material derivative. Different with the work of Fu et al.[34], the continuity equation is not taken into consideration herein as a homogeneous particle distribution can be obtained by applying the transport-velocity formulation[30, 13, 35] with constant density. Therefore, the pressure term in the right-hand-side (RHS) of Eq. (3) can be computed as

$$\boldsymbol{F}_{p,i} = -\frac{2}{m_i} \sum_j V_i V_j p_0 \nabla_i W_{ij} \tag{4}$$

where m is the particle mass, V the particle volume, p_0 the constant background pressure and $\nabla_i W_{ij}$ represents the gradient of the kernel function $W(|\boldsymbol{r}_{ij}|, h)$ with respect to particle i. Here, $\boldsymbol{r}_{ij} = $

$\boldsymbol{r}_i - \boldsymbol{r}_j$ and h is the smoothing length. As the density is constant and equals to unit, we set p_0 equal to unit for simplicity.

With the acceleration induced by the constant background pressure, the particle evolution is defined by

$$\boldsymbol{r}^{n+1} = \boldsymbol{r}^n + \mathrm{d}\boldsymbol{r} = \boldsymbol{r}^n + \frac{1}{2}\boldsymbol{a}^n \Delta t^2 \tag{5}$$

where $\boldsymbol{a}^n = \boldsymbol{F}_p^n$. Note that only the instant acceleration is considered for the particle evolution and the particle velocity is set to zero at the beginning of each time step to achieve a fully stationary state following Refs. [30, 13, 34]. For numerical stability, the time-step size Δt is constrained by the body force criterion

$$\Delta t \leq 0.25 \sqrt{\frac{h}{|\mathrm{d}\boldsymbol{v}/\mathrm{d}t|}} \tag{6}$$

For uniform particle distributions, the acceleration induced by the background pressure would vanish due to

$$\sum_j V_j \nabla_i W_{ij} = \boldsymbol{0} \tag{7}$$

the satisfactory of 0th-order consistency, as shown in Eq. (4). Otherwise, the non-vanishing contribution of the repulsive pressure force leads an equilibrium particle distribution by relaxation[30, 35, 13, 34]. After adopting a suitable boundary condition, a body-fitted isotropic particle distribution for arbitrary geometry can be thus achieved.

2.2 Particle initial condition and evolution strategies

As introduced in the previous section, a Cartesian lattice grid with specific grid spacing is first generated in the whole computational domain. Subsequently, the particle initial condition can be constructed by generating one particle at the cell center if this cell is located inside the geometry as shown in Fig. 1(a). As observed, the initial particles distribution is not in a body-fitted configuration.

With the physics-driven relaxation, all particles are governed by Eq. (3) to achieve homogeneous particle distribution. However, for particles near the surface, boundary treatment is essential to achieve body-fitted feature. In Ref. [34], a dynamic ghost-particle method enforcing symmetry conditions at all domain boundaries is adopted. However, constructing ghost particles for complex geometry is very challenge. In this work, we introduce a simple surface

particle bounding method. For each particle, its level-set value ϕ_i and normal direction N_i can be interpolated from the background mesh using trilinear interpolation method
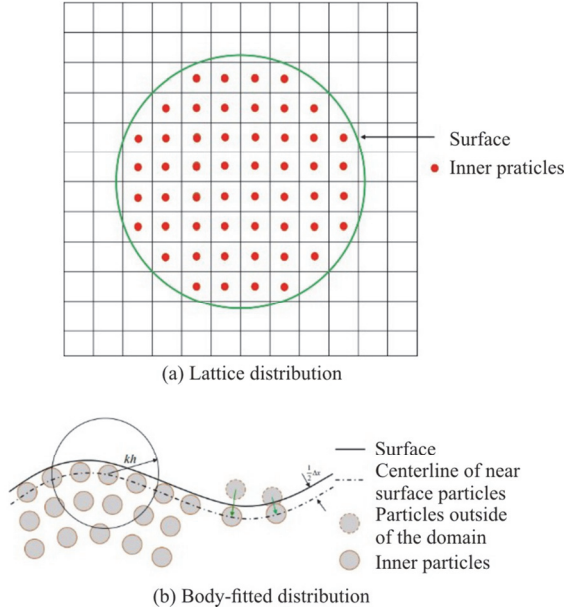

Fig. 1 (Color online) Lattice particle distribution and an illustration of surface particles bounding

$$\phi_i = \phi(r_i), \quad N_i = N(r_i) \tag{8}$$

If the particle satisfies the condition of $\phi_i \geq -1/2\Delta x$, where Δx denotes the initial particle spacing, its position will be updated according to

$$r_i = r_i - \left(\phi_i + \frac{1}{2}\Delta x\right)N_i, \quad \phi_i \geq -\frac{1}{2}\Delta x \tag{9a}$$

$$r_i = r_i \quad \text{otherwise} \tag{9b}$$

as shown in Fig. 1(b). By applying the bounding method, particles near the surface are enforced to locate on geometry surface and a body-fitted particle distribution is achieved accordingly. Note that, the surface particles are relocated at $\phi = -1/2\Delta x$ instead of $\phi = 0$ implying the material interface in the simulation assumed to be located at $\phi = 0$.

2.3 Implementation

In summary, the proposed CAD-BPG consists of the following steps.

(1) Geometry representation in CAD model, in STL format herein, is read and parsed for geometry presentation.

(2) The geometry surface is described implicitly with the level-set function based on a Cartesian background mesh. The level-set field is given by the shortest distance from cell center to the geometry surface, and the corresponding sign is determined by checking whether the cell is inside the geometry.

(3) A preconditioned lattice particle distribution is generated. Then, a physics-driven relaxation process is conducted by imposing the proposed surface bounding method.

The detailed flowchart of the proposed CAD-BPG is outlined in Algorithm 1 (Table 1). It is easy to see that the physics-driven process of the proposed method is almost the same with the SPH for fluid dynamics. This particle generator is simple and can be implemented into an existing SPH code straightforwardly. Also note that the kernel function adopted in this algorithm should be the same with that of the SPH method in real simulation and thus the 0th-order consistency as shown in Eq. (7) of the particle approximation can be achieved. According to our test, the body-fitted particle distribution can be generated within 100 steps relaxation as shown in Section 3.1.

Table 1 Algorithms of the proposed CAD-BPG

Algorithm 1
1. Setup parameters and initialize the physics-driven relaxation
2. Read and parse the polygon mesh of a specific geometry from CAD files
3. Initialize the background Cartesian mesh and the level-set function
4. Generate a preconditioned lattice particle distribution
5. **While** simulation termination condition is not satisfied do
6. Calculate the pressure force F_p (Eq. (4))
7. Set the time-step Δt (Eq. (6))
8. Update particles position r^{n+1} (Eq. (5))
9. Interpolate the attribute function ϕ_i and the corresponding normal direction N_i of each particle (Eq. (8))
10. Constrain outside particles onto surface (Eq. (9))
11. Update the particle-neighbor list and kernel values and gradient
12. Update the particle configuration
13. **End**
14. Terminate the physics-driven relaxation

3. Examples

In this part, we first test the proposed CAD-BPG for a simple sphere and validate its accuracy by the convergence analysis of L2-norm error. Subsequently, the CAD-BPG is applied for generating particle distribution for complex structure including propeller, stents and anatomical heart model. Finally, the CAD-BPG is implemented as a pre-processing tool for modeling regular wave interaction with an OWSC and the predicted surface elevation, flap rotation and pressure loads are compared with experimental data. The 5th-order C2 Wendland[36] is applied and the

smoothing length is set as $h = 1.05\Delta x$ with Δx denoting the initial particle spacing for all cases. Note that we perform the physics-driven relaxation starting from a random particle distribution rather than the lattice one to demonstrate the robustness of the present method. Also, the background mesh for level-set field is only established within a narrow band of the geometry interface to save storage memory.

3.1 *Sphere*

A sphere with radius $R = 40$ as shown in Fig. 2(a) is first considered. Imported from an external STL file, the geometry is read and parsed. The established level-set field and the corresponding geometry surface are given in Fig. 2(b). Although this geometry is simple, it is still difficult to generate a body-fitted uniform particle distribution for traditional methods. In this test, three resolutions with $\Delta x = R / 20$, $\Delta x = R / 40$ and $\Delta x = R / 80$ are adopted.
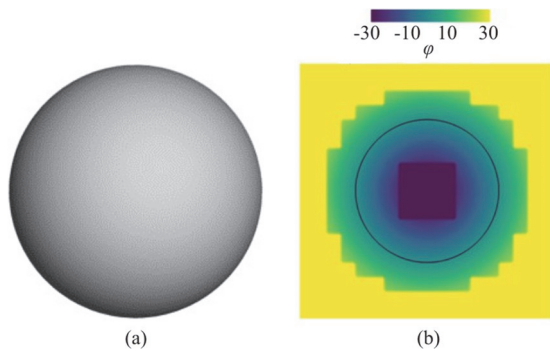
Fig. 2 (Color online) Sphere: (a) Visualization of CAD geometry in STL format and (b) sliced view of the level-set field

Figure 3 shows the lattice and relaxed particle generations of the sphere at the resolution of $\Delta x = R / 20$. We can observe that the lattice particle distribution cannot represent the exact geometry. However, as shown in Fig. 3(c) and the corresponding slice view, the proposed CAD-BPG gives a most realistic representation of the geometry even though the particle evolution starts from a random distribution. Figure 4 gives the particle distribution for two higher resolutions. It is obvious that the particle generated by CAD-BPG is body-fitted and uniformly distributed. The averaged L2-norm distance D_{avg} between surface particles and the surface and the averaged particle kinetic energy are presented in Figs 5(a) and 5(b), respectively. At the beginning, particles distribution is not body-fitted and the distance between surface particle and the surface is large especially for the one with lower resolution. After several steps of relaxation, the distance is approaching to zero and the kinetic energy is tending to stable.

Note that the averaged particle kinetic energy is not vanished in stable state which is caused by the non-vanishing repulsive force for surface particles. Besides, we want to emphasize that the present CAD-BPG can achieve the almost equilibrium state less than 100 steps in this case demonstrating its efficiency.
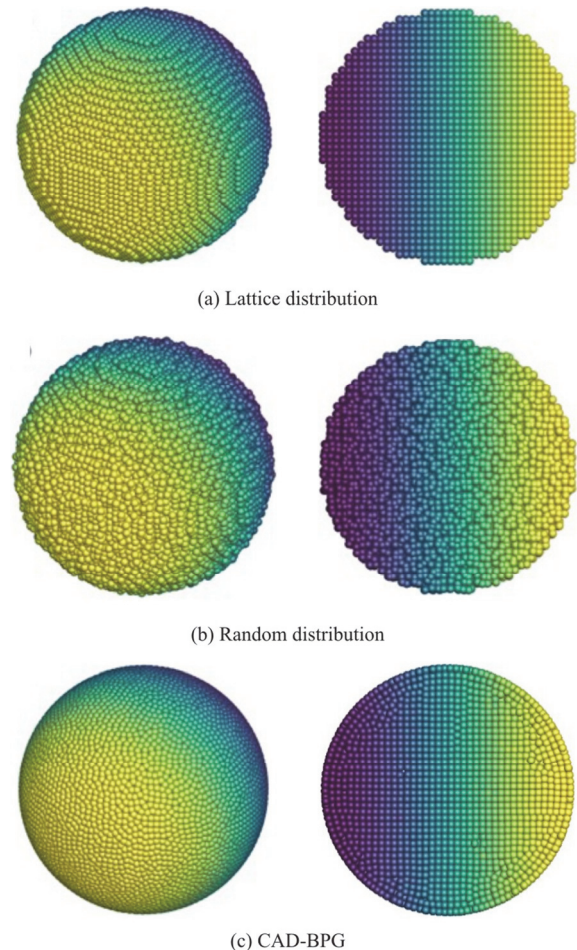

(a) Lattice distribution

(b) Random distribution

(c) CAD-BPG

Fig. 3 (Color online) Particle distributions with spatial resolution of $\Delta x = R / 20$ and their sliced view (right panel) for sphere

3.2 *Applications in complex structure*

In this part, the CAD-BPG is implemented for generating particle for complex structure which are ubiquitous in industrial and biomechanical applications. Firstly, we consider a propeller structure which consists of 12 sharp blades as shown in Fig. 6(a). This structure is very challenging due to its complex geometry and blade's sharp nature. Figure 6 shows the body-fitted particle distribution for the propeller with 955 450 total particles in different points of view. It can be noted that the present CAD-BPG can generate a well-regularized particle distribution for this complex geometry and reproduce the sharp blades well. To the best knowledge of the authors, this is the first

body-fitted particle distribution generated for propeller structure. In the future work, this propeller model will be used for studying the fluid interaction with propeller structure which is our ongoing work.
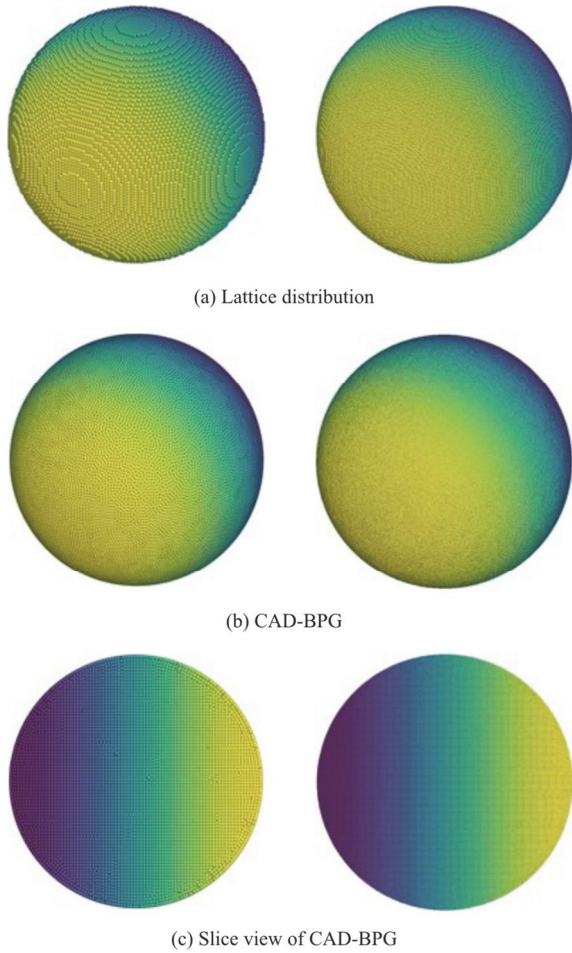

(a) Lattice distribution

(b) CAD-BPG

(c) Slice view of CAD-BPG

Fig. 4 (Color online) Particle distributions with two higher spatial resolutions ($\Delta x = R / 40$ (left panel), $\Delta x = R / 80$ (right panel)) for sphere

Secondly, we consider two realistic cardiovascular stent structures, i.e., Palmaz-Schatz shaped (PS-shaped) stent and Cypher shaped (C-shaped) stent, which are widely used in clinical applications. In recent years, considerable amount of FEM-based researches have been carried out in order to improve the quality and feasibility of stents. However, particle-based research has not been conducted due to the lack of body-fitted particle distribution on them.

Figure 7 shows the CAD geometry of PS-shaped stent and the corresponding body-fitted particle distribution with total 226 775 particles generated by the present CAD-BPG. It is clear that the geometry is well represented and particles are uniformly distributed. For the C-shaped stent, the CAD geometry as well as the corresponding particle distribution with total 45 644 particles are presented in Fig. 8. Again, a

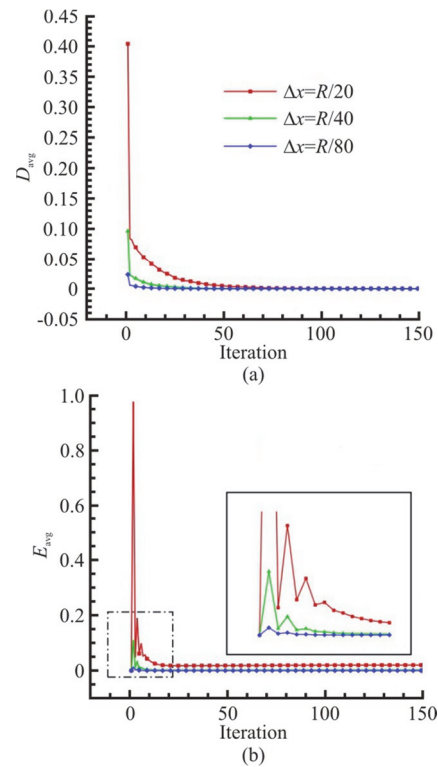body-fitted particle distribution is achieved.

Fig. 5 (Color online) Sphere: (a) Averaged L2-norm distance between surface particles and physics surface and (b) averaged particle kinetic energy

Numerical modeling of the human heart and its function can help us understand various cardiac diseases as noted in Ref. [37]. In our recent work of Ref. [22] an integrative SPH method for addressing the simulation of the principle aspects of cardiac function, including cardiac electrophysiology, passive mechanical response and electromechanical coupling, is presented. For total heart modeling where complex geometry is involved, body-fitted particle distribution is essential for numerical accuracy. In the last but not least case, we consider a total heart model which consists of four chambers. Its CAD geometry and the body-fitted particle distribution with 500091 total particles are shown in Fig. 9. It can be noted that a well-regularized particle distribution is produced demonstrating that the present CAD-BPG can handle very complex geometries. Note that the stent and heart model will be used in our future work concerning the modeling of total heart function.

3.3 Wave interaction with an oscillating wave surge converter

In this section, we implement the proposed CAD-BPG as a pre-processing tool for the modeling of wave interaction with an OWSC. Following the experimental work of Wei et al.[38], the schematic of
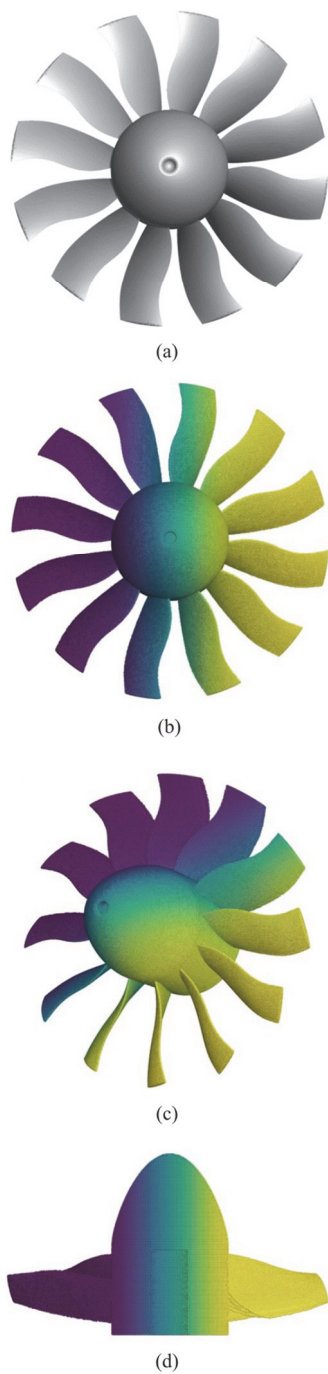
Fig. 6 (Color online) Propeller: (a) Visualization of CAD geometry in STL format, (b) particle distribution by CAD-BPG, (c) one side view of CAD-BPG, (d) another side view of CAD-BPG
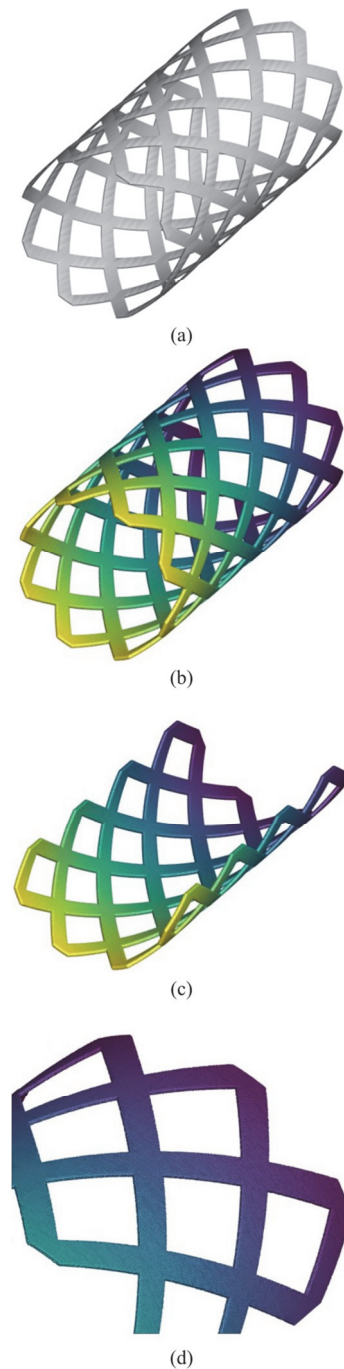

Fig. 7 (Color online) Palmaz-Schatz shaped stent: (a) Visualization of CAD geometry in STL format, (b) particle distribution by CAD-BPG, (c) sliced view of CAD-BPG, (d) a zoom of CAD-BPG

the numerical setup is shown in Fig. 10. Here, the OWSC device is simplified as a 1.04 m×0.48 m×0.12 m box-type flap hinged to a 0.16 m high base. The mass of the flap is 33 kg and the inertia of the flap is 1.84 kg·m^2. One wave probe termed as WP04 located at $x = 3.99$ m and four pressure sensors whose positions are given in Table 2 are used to measure the time

histories of the surface elevation and pressure loads on the flap. Note that the pressure sensors and wave probe are termed identical to those of the experiment in Ref. [38] for clarity.

In this case, both the body-fitted particle distribution and the lattice one are considered. Figure 11 presents the boundary-representation of the tank, wave
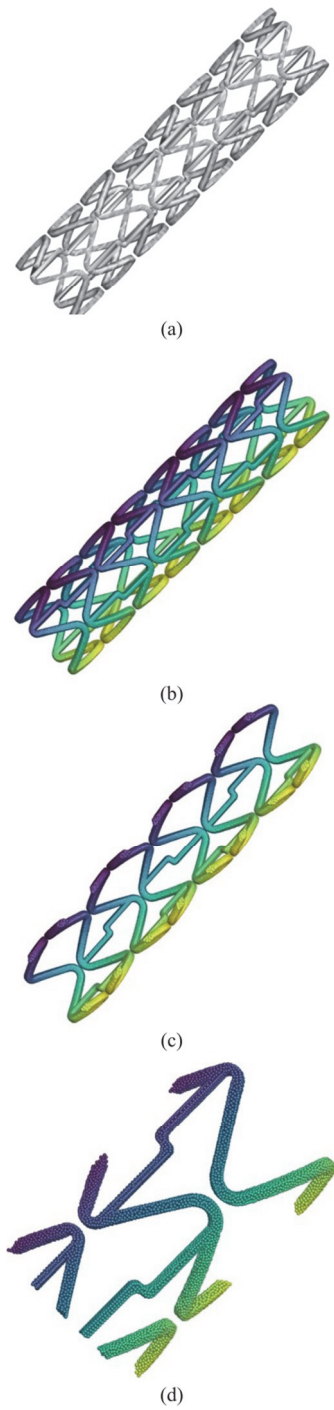
(a)

(b)

(c)

(d)

Fig. 8 (Color online) Cypher shaped stent: (a) Visualization of CAD geometry in STL format, (b) particle distribution by CAD-BPG, (c) sliced view of CAD-BPG, (d) a zoom of CAD-BPG

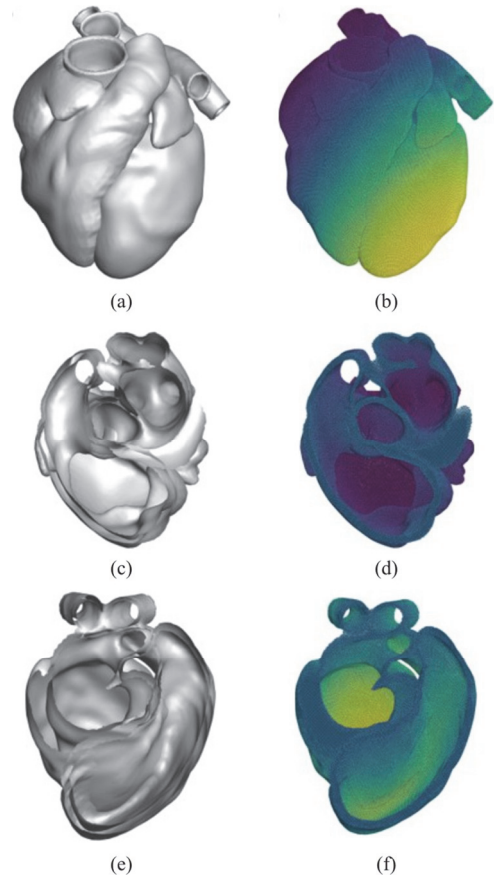

(a)   (b)

(c)   (d)

(e)   (f)

Fig. 9 (Color online) Lv-heart: (a) Visualization of CAD geometry in STL format, (b) particle distribution by CAD-BPG, (c) one sliced view of CAD geometry, (d) sliced view of CAD-BPG corresponding to (c), (e) another sliced view of CAD geometry, (f) sliced view of CAD-BPG corresponding to (e)

maker and flap as well as their corresponding particle distributions generated by the present CAD-BPG. For both tests, the initial particle space is set as $\Delta x = 0.03 \, \text{m}$ resulting in a number of 1.542×10^6 fluid particles and 0.628×10^6 solid particles (including tank, wave maker and flap).

The regular wave can be generated by imposing a piston–type wave maker whose displacement is determined by the linear wave making theory

$$\boldsymbol{r} = S \sin(ft + \phi) \tag{10}$$

where S is the wave stroke, f the wave frequency and ϕ the initial phase. Here, the wave stroke S is determined by

$$S = \frac{H \sinh(2kh_0) + 2kh_0}{\sinh(2kh_0) \tanh(kh_0)} \tag{11}$$

where H is the wave height, h_0 the water depth and k is the wave number. We consider the regular wave interaction with OWSC in condition of wave height $H = 5 \, \text{m}$ and wave period $T = 10 \, \text{s}$ in full scale.
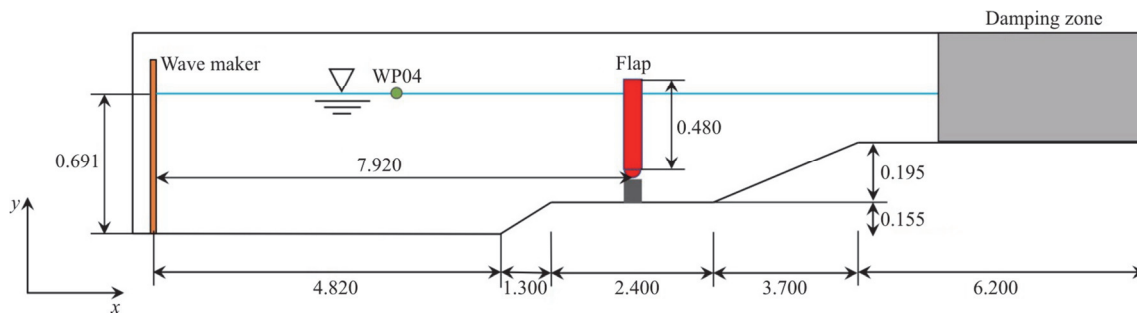
Fig. 10 (Color online) Schematic of the wave tank and the OWSC model. The scale is $1:25$ (m)

Table 2 Positions of the pressure sensors on the front flap face. The position along the z - axis is measured from the center of the device, and $y = 0$ denotes the mean water level

| No.	y - axis/m	z - axis/m
PS01	−0.046	−0.468
PS03	0.050	0.364
PS05	−0.300	0.364
PS13	0.025	0.052

For the wave interaction with the flap, the total force and torque acting about the center of mass of the solid body can be expressed as

$$\boldsymbol{F} = \sum_{a \in N} \boldsymbol{f}_a , \quad \boldsymbol{\tau} = \sum_{a \in N} (\boldsymbol{r}_a - \boldsymbol{r}_{com}) \times \boldsymbol{f}_a \tag{12}$$

where $\boldsymbol{r}_{com}$ is the center of mass, $\boldsymbol{f}_a$ denotes the fluid force action on a flap particle a located at $\boldsymbol{r}_a$. The total force and torque are obtained to solve the Newton-Euler equation

$$\begin{pmatrix} \boldsymbol{F} \\ \boldsymbol{\tau} \end{pmatrix} = \begin{pmatrix} m\mathbb{I} & 0 \\ 0 & \boldsymbol{I} \end{pmatrix} \begin{pmatrix} \dfrac{\mathrm{d}\boldsymbol{v}}{\mathrm{d}t} \\ \dfrac{\mathrm{d}\boldsymbol{\Omega}}{\mathrm{d}t} \end{pmatrix} \tag{13}$$

where m is the mass of flap, $\mathbb{I}$ the identity matrix, $\boldsymbol{I}$ the moment of inertia about the center of mass and $\boldsymbol{\Omega}$ is the angular velocity. Here, only the rotation is taken into consideration for the motion of the flap.
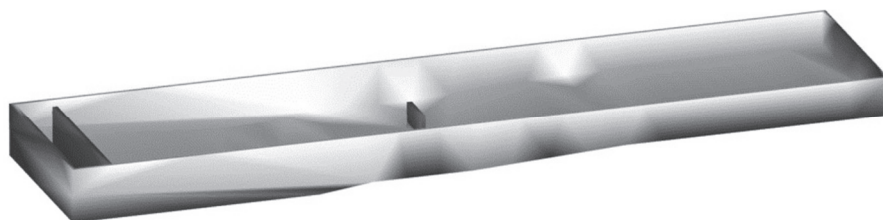
(a) Visualization of CAD geometry in STL format
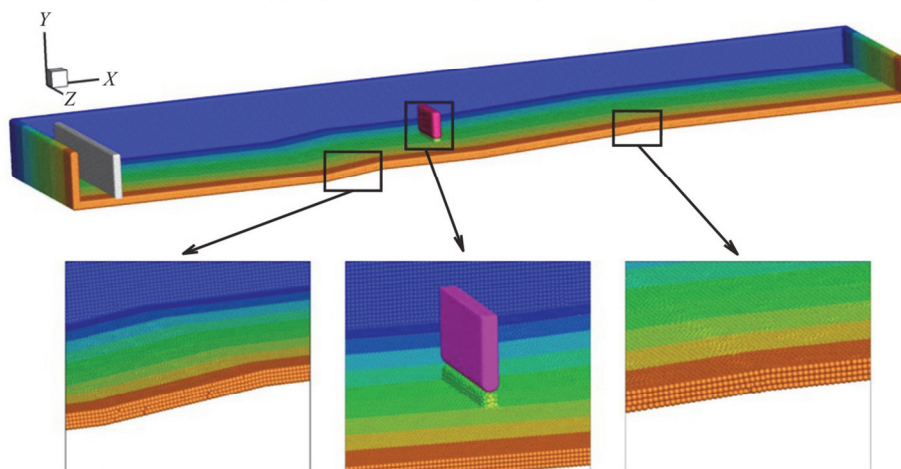
(b) Particles distributions by CAD-BPG

Fig. 11 (Color online) Modeling of wave interaction with OWSC: (a) Visualization of CAD geometry in STL format and (b) particles distributions by CAD-BPG

Figure 12 presents several snapshots showing the free surface colored by velocity magnitude and the flap's rotation predicted by using the body-fitted particle distribution as initial condition. It can be observed that smooth velocity fields are produced even complex interactions between wave and the flap are involved. Also, wave refection and breaking can be noted in the region near the flap during the interaction.

(a) t=23.5

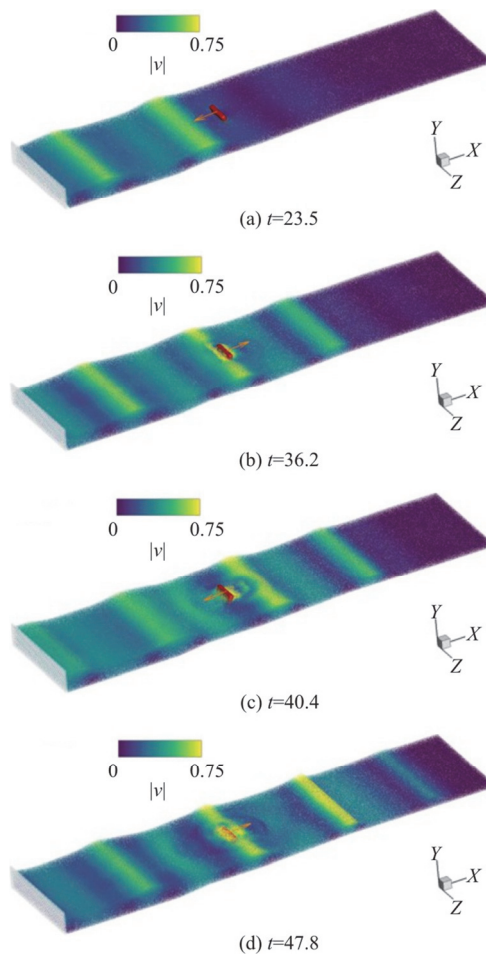(b) t=36.2

(c) t=40.4

(d) t=47.8

Fig. 12 (Color online) Modeling of wave interaction with OWSC: Free surfaces with particles colored by velocity magnitude and the flap motion predicted by body-fitted particle distribution for wave height $H = 5\,\mathrm{m}$ and wave period $T = 10\,\mathrm{s}$

Figure 13 shows the comparison of the time history of surface elevation at probe WP04 and the corresponding flap rotation between experimental data and numerical results obtained by the lattice and body-fitted particle distributions. For wave elevation as shown in Fig. 13(a), both results have good agreement with experimental data while the body-fitted particle initial condition shows improved accuracy in modeling of wave dynamics. This may due to the fact that body-fitted particle distribution of

the tank's slope parts significantly improve the accuracy of fluid-solid interaction. Again, the body-fitted particle distribution shows impressive improvement in predicting the large amplitude rotation of the flap as shown in Fig. 13(b).

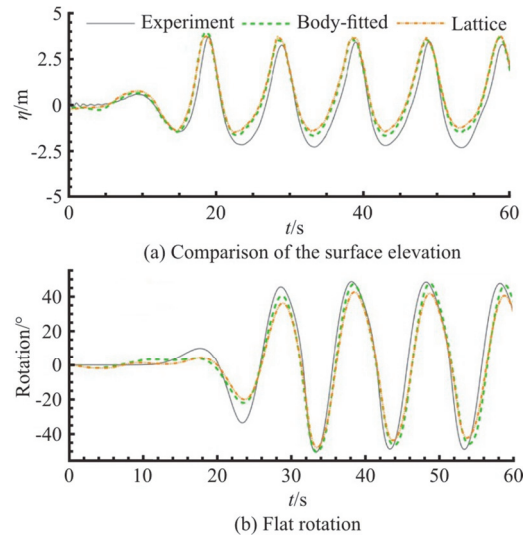(a) Comparison of the surface elevation

(b) Flat rotation

Fig. 13 (Color online) Modeling of wave interaction with OWSC: Comparison of the surface elevation (top panel) and flap rotation (bottom panel) for wave height $H = 5\,\mathrm{m}$ and wave period $T = 10\,\mathrm{s}$

Figure 14 shows the time histories of the pressure signals recorded by the pressure sensors given in Table 2. Note that the initial hydrostatic pressure is subtracted from the recorded pressure signals inducing negative drops in some profiles as Ref. [38]. Compared with the experimental data, the main plateaus of all the pressure profiles are reasonably well captured by both particle distributions. For sensors PS01 and PS03, large pressure peaks and drops are noted since the present SPH model is based on weakly-compressible assumption and air cushion effects are not captured in mono-fluid simulation. Similar to the results reported in Ref. [38], the pressure drops for sensors PS05 and PS13 are underestimated in present results and theses discrepancies are related to the wave breaking. Also, the pressure signals show identical profile for both particle distributions indicating that the initial particle distribution has small effects on the pressure field.

4. Conclusion

In this paper, we present a CAD-compatible body-fitted particle generator for arbitrarily complex 3-D geometry and apply it as a pre-processing tool for modeling of wave-structure interaction. This particle generator mainly includes the following procedures: (1) the geometry information is accessed by importing
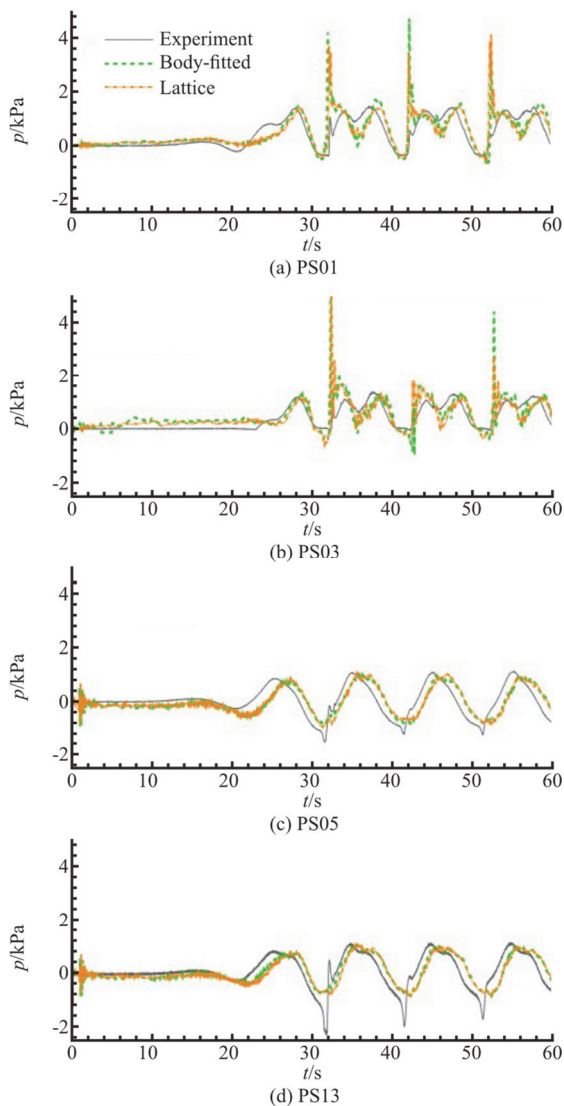
Fig. 14 (Color online) Modeling of wave interaction with OWSC: Comparison of the time histories of wave loads on the flap for wave height $H = 5\,\text{m}$ and wave period $T = 10\,\text{s}$

are uniformly distributed. Then, the improvements of computational accuracy by adopting the present CAD-BPG are proved by a physical implementation. In addition, the present approach is CAD-compatible and can read arbitrarily complex geometry from external CAD files implying a promising potential of particle-based methods in real-world applications.

References

[1] Gingold R. A., Monaghan J. J. Smoothed particle hydrodynamics: Theory and application to non-spherical stars [J]. *Monthly Notices of the Royal Astronomical Society*, 1977, 181(3): 375-389.

[2] Lucy L. B. A numerical approach to the testing of the fission hypothesis [J]. *The Astronomical Journal*, 1977, 82: 1013-1024.

[3] Koshizuka S., Oka Y. Moving-particle semi-implicit method for fragmentation of incompressible fluid [J]. *Nuclear Science and Engineering*, 1996, 123(3): 421-434.

[4] Mishra B. K., Rajamani R. K. The discrete element method for the simulation of ball mills [J]. *Applied Mathematical Modelling*, 1992, 16(11): 598-604.

[5] Monaghan J. J. Simulating free surface flows with SPH [J]. *Journal of Computational Physics*, 1994, 110(2): 399-406.

[6] Hu X. Y., Adams N. A. A multi-phase SPH method for macroscopic and mesoscopic flows [J]. *Journal of Computational Physics*, 2006, 213(2): 844-861.

[7] Monaghan J. J. SPH without a tensile instability [J]. *Journal of Computational Physics*, 2000, 159(2): 290-311.

[8] Zhang C., Hu X. Y., Adams N. A. A weakly compressible SPH method based on a low-dissipation Riemann solver [J]. *Journal of Computational Physics*, 2017, 335: 605-620.

[9] Zhang C., Xiang G. M., Wang B. et al. A weakly compressible SPH method with WENO reconstruction [J]. *Journal of Computational Physics,* 2019, 392: 1-18.

[10] Benz W., Asphaug E. Simulations of brittle solids using smooth particle hydrodynamics [J]. *Computer Physics Communications*, 1995, 87(1-2): 253-265.

[11] Libersky L. D., Petschek A. G. Smooth particle hydrodynamics with strength of materials (Larry D., Libersky A., Petschek G. Advances in the free-Lagrange method including contributions on adaptive gridding and the smooth particle hydrodynamics method) [M]. Berlin, Heidelberg, Germany: Springer, 1991, 248-257.

[12] Randles P. W., Libersky L. D. Smoothed particle hydrodynamics: Some recent improvements and applications [J]. *Computer Methods in Applied Mechanics and Engineering*, 1996, 139(1-4): 375-408.

[13] Zhang C., Hu X., Adams N. A. A generalized transport-velocity formulation for smoothed particle hydrodynamics [J]. *Journal of Computational Physics*, 2017, 337: 216-232.

[14] Ye T., Pan D., Huang C. et al. Smoothed particle hydro-

and parsing the polygon mesh storing in external CAD files, and the geometry surface is then described by an implicit zero level-set function, (2) starting from a preconditioned lattice or random particle distribution, particles evolution is driven by a constant background pressure under the framework of WCSPH methodology, (3) surface particles are constrained by introducing an efficient surface bounding method to achieve body-fitted feature. With the assumption that each particle possesses an invariant volume, a body-fitted well-regularized particle distribution can be achieved when system approaches to stable state. A number of benchmark cases with complex geometry demonstrate that the particle distribution generated by the present CAD-BPG represents the geometry well and particles

dynamics (SPH) for complex fluid flows: Recent developments in methodology and applications [J]. *Physics of Fluids*, 2019, 31(1): 011301.

[15] Zhang C., Rezavand M., Hu X. A multi-resolution SPH method for fluid-structure interactions [J]. *Journal of Computational Physics*, 2021, 429: 110028.

[16] Gotoh H., Khayyer A. On the state-of-the-art of particle methods for coastal and ocean engineering [J]. *Coastal Engineering Journal*, 2018, 60(1): 79-103.

[17] Siemann M. H., Ritt S. A. Novel particle distributions for SPH bird-strike simulations [J]. *Computer Methods in Applied Mechanics and Engineering*, 2019, 343: 746-766.

[18] Alimirzazadeh S., Kumashiro T., Leguizamón S. et al. GPU-accelerated numerical analysis of jet interference in a six-jet Pelton turbine using finite volume particle method [J]. *Renewable Energy*, 2020, 148: 234-246.

[19] Ji Z., Stanic M., Hartono E. A. et al. Numerical simulations of oil flow inside a gearbox by smoothed particle hydrodynamics (SPH) method [J]. *Tribology International*, 2018, 127: 47-58.

[20] Zhang C., Wei Y., Dias F. et al. An efficient fully Lagrangian solver for modeling wave interaction with oscillating wave energy converter [EB/OL]. arXiv preprint, 2020, arXiv:2012.05323.

[21] Crespo A. J. C., Hall M., Domínguez J. M. et al. Floating moored oscillating water column with meshless SPH method [C]. *ASME 2018 37th International Conference on Ocean, Offshore and Arctic Engineering*, Madird, Spain, 2018.

[22] Zhang C., Wang J., Rezavand M. et al. An integrative smoothed particle hydrodynamics framework for modeling cardiac function [J]. *Computer Methods in Applied Mechanics and Engineering*, 2021, 381: 113847.

[23] Zhang C., Zhu Y., Yu Y. et al. A simple artificial damping method for total Lagrangian smoothed particle hydrodynamics [EB/OL]. arXiv preprint, 2021, arXiv:2102.04898.

[24] Domínguez J. M., Crespo A. J. C., Barreiro A. et al. Development of a new pre-processing tool for SPH models with complex geometries [C]. *6th International SPHERIC workshop*, Hamburg, Germany, 2011, 117-124.

[25] Vignjevic R., Orłowski M., De Vuyst T. et al. A parametric study of bird strike on engine blades [J]. *International Journal of Impact Engineering*, 2013, 60: 44-57.

[26] Heimbs S. Computational methods for bird strike simulations: A review [J]. *Computers and Structures*, 2011, 89(23-24): 2093-2112.

[27] Diehl S., Rockefeller G., Fryer C. L. et al. Generating optimal initial conditions for smoothed particle hydrodynamics simulations [J]. *Publications of the Astronomical Society of Australia*, 2015, 32: e048.

[28] Vela L. V., Sanchez R., Geiger J. ALARIC: An algorithm for constructing arbitrarily complex initial density distributions with low particle noise for SPH/SPMHD applications [J]. *Computer Physics Communications*, 2018, 224: 186-197.

[29] Fu L., Ji Z. An optimal particle setup method with Centroidal Voronoi Particle dynamics [J]. *Computer Physics Communications*, 2019, 234: 72-92.

[30] Adami S., Hu X. Y., Adams N. A. A transport-velocity formulation for smoothed particle hydrodynamics [J]. *Journal of Computational Physics*, 2013, 241: 292-307.

[31] Zhang C., Rezavand M., Zhu Y. et al. SPHinXsys: An open-source meshless, multi-resolution and multi-physics library [J]. *Software Impacts*, 2020, 6: 100033.

[32] Sherman M. A., Seth A., Delp S. L. Simbody: Multibody dynamics for biomedical research [J]. *Procedia IUTAM*, 2011, 2: 241-261.

[33] Osher S., Sethian J. A. Fronts propagating with curvature-dependent speed: Algorithms based on Hamilton-Jacobi formulations [J]. *Journal of Computational Physics*, 1988, 79(1): 12-49.

[34] Fu L., Han L., Hu X. et al. An isotropic unstructured mesh generation method based on a fluid relaxation analogy [J]. *Computer Methods in Applied Mechanics and Engineering*, 2019, 350: 396-431.

[35] Litvinov S., Hu X. Y., Adams N. A. Towards consistence and convergence of conservative SPH approximations [J]. *Journal of Computational Physics*, 2015, 301: 394-401.

[36] Wendland H. Piecewise polynomial, positive definite and compactly supported radial functions of minimal degree [J]. *Advances in computational Mathematics*, 1995, 4(1): 389-396.

[37] Quarteroni A., Lassila T., Rossi S. et al. Integrated heart–Coupling multiscale and multiphysics models for the simulation of the cardiac function [J]. *Computer Methods in Applied Mechanics and Engineering*, 2017, 314: 345-407.

[38] Wei Y., Rafiee A., Henry A. et al. Wave interaction with an oscillating wave surge converter, part I: Viscous effects [J]. *Ocean Engineering*, 2015, 104: 185-203.